Observation of the antimatter helium-4 ($^4\overline{\mathrm{He}}$, $\overline{\alpha}$) nucleus and the study of its formation mechanism

by

Liang Xue

Dissertation Director: Prof. YuGang Ma

Off-campus Co-adviser: Dr. Aihong Tang

A Dissertation
Submitted to Graduate University
of
Chinese Academy of Sciences
In partial fulfillment of
the requirement For the degree of
Doctor of Philosophy

Shanghai Institute of Applied Physics
Chinese Academy of Sciences

April, 2012

Dedicated to my parents

Acknowledgments

First and foremost, I would like to express my heartfelt gratitude to my advisor Prof. Yugang Ma for the continuous support of my Ph.D study, for his patience, motivation, experience, and immense knowledge. His guidance helped me in all the time of my research and writing of this thesis. I could not have imagined having a better advisor for my Ph.D study. I hope that one day I would become as good as an advisor to my student as Prof. Ma has been to me.

I would like to address special thanks and appreciation to my co-advisor Dr. Aihong Tang. During my years at Brookhaven National Laboratory (BNL) as a visitor, he brought me into the world of experimental high energy nuclear physics, showed me how to research a problem and achieve goals, taught me how to question thoughts and express ideas. He has given me plenty of opportunities to present my work in front of experts in the field, spent endless time reviewing and proofreading my papers. The many skills I have learnt from him will constantly remind me of how great a teacher he is throughout my life.

My sincere thanks also goes to Prof. Nu Xu, Dr. Hank Crawford, Prof. Keane Declan, Dr. Zhangbu Xu, and Prof. Huan Zhong Huang, for helpful suggestions and fruitful discussions. Many thanks to Dr. Tonko Ljubicic, Dr. Jeff Landgraf, Dr. Yuri Fisyak, Dr. Gene Van Buren, and Dr. Jerome Lauret for their technical support. I extend my thanks to the members of STAR group at BNL, and the physics working group for providing abundant

healthy discussion in my research. Particularly, I would like to acknowledge Dr. Xin Dong, Dr. Lijuan Ruan, Dr. Yifei Zhang, Dr Zebo Tang, Dr. Xiaoping Zhang, Dr. Hao Qiu, Dr. Bingchu Huang, Hongwei Ke, and Jie Zhao, for many valuable discussion that helped me understand my research better.

I am also indebted to the members of heavy ion reaction group at SINAP, especially Prof. Xiangzhou Cai, Prof. Guoliang Ma, Prof. Chen Zhong, Prof. Jinhui Chen, Prof. Song Zhang, and Prof. Jun Xu, for their insightful comments and constructive criticisms at different stages of my Ph. D research. I am grateful to all my friends at SINAP for the support they provided.

Most importantly, none of this would have been possible without the love and patience of my parents, to whom this thesis is dedicated. I would like to express my heartfelt gratitude to them. Finally, my deepest appreciation to my wife Zhaoli Liu, whose love and support is always the first reason I am able to do anything of value.

Abstract

According to the CPT symmetry, a fundamental symmetry of physical laws under transformations that involve the simultaneous inversion of charge, parity and time, matter and antimatter are supposed to be created with comparable abundance at the beginning of the universe. However, overwhelming evidences[1–3] support that our world today consists almost entirely of matter rather than antimatter. The study of the so called matter-antimatter asymmetry is one of the most important frontiers in modern physics. One necessary step of this study is to create and identify antimatter fragments. In addition to space based experiments[4–6] which passively look for tiny antimatter fragments in cosmos, high-energy nuclear collisions, by creating an energy density similar to that of the universe microseconds after the Big Bang, can be used to actively produce antimatter and study their production mechanisms. The Relativistic Heavy Ion Collider (RHIC), located at Brookhaven National Laboratory (BNL), produces a high-temperature and high-density matter (Quark Gluon Plasma)[7, 8], containing roughly equal number of quarks and antiquarks, by colliding two gold beams at near light speed. The environment created is ideally suitable for the production of antimatter nucleus and hypernucleus. Antimatter helium-4 nucleus($^4\overline{\mathrm{He}}$, or $\overline{\alpha}$), which consists of two antiprotons ($\overline{\mathrm{p}}$) and antineutrons ($\overline{\mathrm{n}}$), has not been observed previously although the α-particle was identified a century ago by Rutherford and is present in cosmic radiation at the ten per cent level[9]. Here we report the observation of $^4\overline{\mathrm{He}}$[9, 10], the heaviest observed antinucleus to date. In total, 18 $^4\overline{\mathrm{He}}$ were detected by the STAR experiment in 10^9 recored Au+Au collisions. The invariant yields of ^{4}He and $^4\overline{\mathrm{He}}$ in central Au+Au collisions are consistent with the expectations of both the statistical model and the coalescence model. The reduction factor is of $1.1^{+0.3}_{-0.2}\times10^3$ ($1.6^{+1.0}_{-0.6}\times10^3$) for each additional

nucleon (antinucleon) added to nucleus (antinucleus). Unless there is a breakthrough in the accelerator technology, it is likely that the $^4\overline{\mathrm{He}}$ will remain the heaviest stable antimatter nucleus observed for the foreseeable future. Our finding provides a baseline for future searches of $^4\overline{\mathrm{He}}$ in cosmos.

We also present a phenomenological study[11, 12] on the formation mechanism of light (anti)nuclei (d, $\overline{\mathrm{d}}$, ^{3}He, $^3\overline{\mathrm{He}}$, $^3_\Lambda$H, $^3_{\overline{\Lambda}}\overline{\mathrm{H}}$, ^{4}He, $^4\overline{\mathrm{He}}$) in relativistic heavy ion collisions, based on a hydrodynamic BlastWave model[13–15] coupled with a coalescence model[16, 17]. Our calculations for the p_T spectra of p, $\overline{\mathrm{p}}$, Λ, $\bar{\Lambda}$, ^{3}He, $^3\overline{\mathrm{He}}$ are in good agreement with STAR results, and the reduction factor is of 1.3×10^3 (1.7×10^3) for each additional nucleon (antinucleon) added to nucleus (antinucleus), also roughly consistent with experimental measurements. We further calculated the production rate of other exotic particles, which provides a good reference for future observations.

Keywords: RHIC, High Level Trigger, antimatter helium-4 nucleus($\overline{\alpha}$), $\Lambda\Lambda$

Contents

Chapter 1 Introduction

1.1 Standard model

The search for the fundamental building blocks of matter is one of the primary goals of particle physics. The so-called Standard Model of particle physics (formulated in the 1970's) describes the universe in terms of three generations of quarks, leptons and their anti-particles. There are six flavors of quarks and leptons: for quarks, up (u), down (d), strange (s), charm (c), bottom (b), and top (t), and for leptons, electron (e), electron neutrino (ν_e), μ, μ neutrino (ν_μ), τ, and τ neutrino (ν_τ). The collection of quarks and leptons is shown in Figure 1-1. Hadrons are viewed as being composed of quarks, either as quark-antiquark pairs (mesons) or as three quarks (baryons). There are four kinds of fundamental forces along with their carrier particles, namely graviton for gravitation, photon for electromagnetic force, $W^{\pm}$ and Z for weak interaction, and gluon for strong interaction. Aside from the graviton for gravitation, all other carrier particles have been observed experimentally. The force range for gravitation and electromagnetic force are infinite, that for weak interaction and strong interaction are 10^{-18} m and 10^{-15} m, respectively. In the Standard Model of particle physics, hadrons are composites that are "glued" together by gluons, and can described by the strong nuclear force. The widely-accepted theory for strong interaction

is Quantum Chromodynamics (QCD).

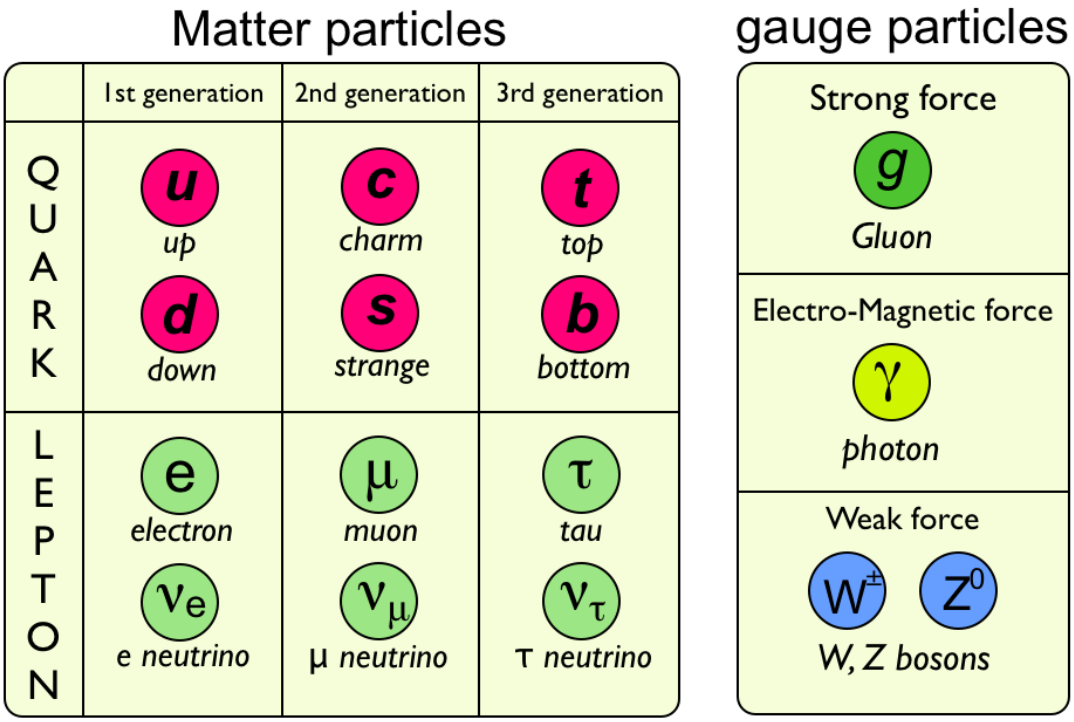

Figure 1-1: The building blocks of matter in standard model.

1.2 Quantum chromodynamics (QCD)

1.2.1 Asymptotic freedom and confinement

Quantum chromodynamics (QCD) is the SU(3) Yang-Mills theory (gauge field theory) that describes the strong interactions of colored quarks and gluons. Analogous to the two-valued electrical charge associated with electromagnetic force is a three-valued "color charge" associated with quarks and gluons. That is the reason why the strong nuclear force is also called the "color interaction". QCD enjoys two peculiar properties: asymptotic freedom and confinement. They can be qualitatively described by the strong coupling constant:

$$\alpha_s(Q^2) = \frac{12\pi}{\beta_0 \ln(Q^2/\Lambda_{QCD})} \tag{1-1}$$

Asymptotic freedom says that quarks interact weakly at high energies (larger Q^2), when the distance between quarks decreases. On the other hand, confinement means that the interactions between quarks does not diminish as they are separated (small Q^2), and, it would take infinite amount of energy to separate two quarks. A good agreement between measured α_s and QCD calculations can be seen in Figure 1-2.

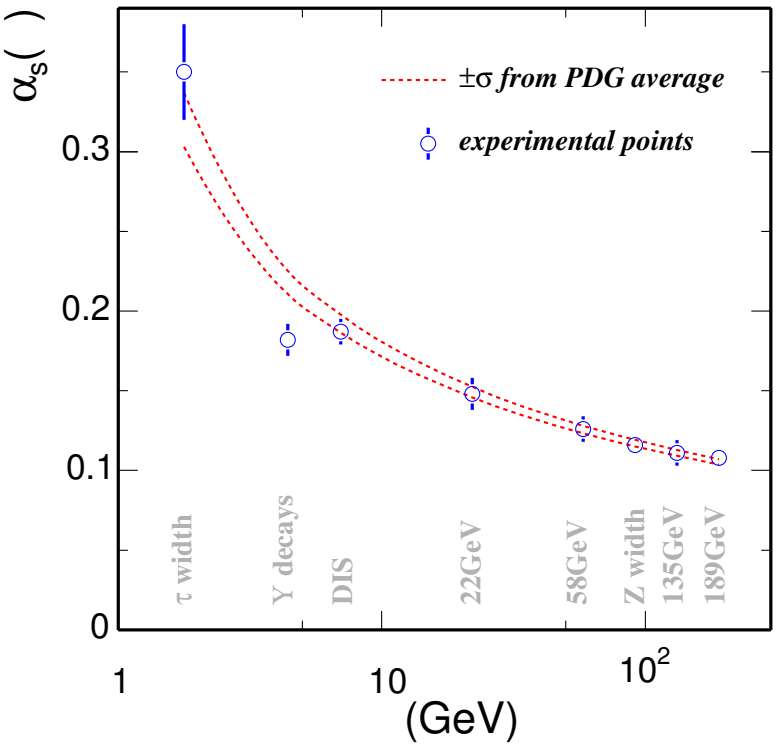

Figure 1-2: Running of the strong coupling constant established by various types of measurements at different scals, compared to the QCD calculation[18].

1.2.2 QCD phase transition

Free quarks and gluons can not be observed under normal conditions due to the color confinement. However, lattice QCD suggests that quarks will be deconfined and a new state of matter called Quark Gluon Plasma (QGP) will be created if the temperature is extremely high. The critical temperature (T_c) and the energy density (ϵ_c) for the QCD phase transition are 170 MeV and 1 GeV/fm^3, respectively[19, 20]. Figure 1-3 depicts the energy density

as a function of temperature (in units of T/T_c) with different number of flavors. ϵ/T^4 reflects the entropy or total number of degrees of freedoms of the system. The tremendous increase of ϵ/T^4 corresponds to the formation of QGP where new degrees of freedom are created with free quarks and gluons. Arrows in the figure indicate the continuum ideal gas limits for two and three flavor QCD. The lattice studies of the QCD energy density indicate that deviations from StefanBoltzmann limits for the ideal gas are about (15 - 20)% in the temperature interval $2T_c < T < 4T_c$.

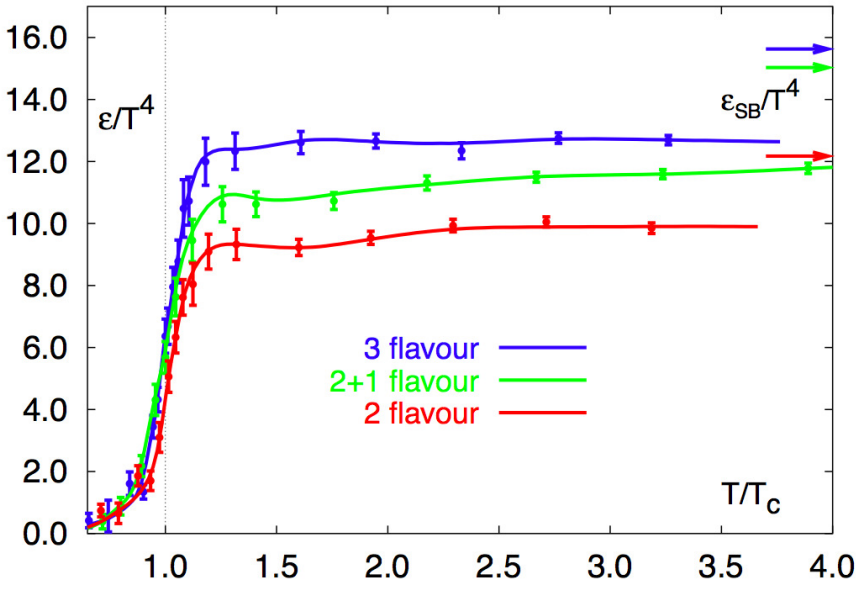

Figure 1-3: Energy density as a function of temperature (in units of T/T_c). Arrows in the figure present the continuum ideal gas values.[19]

1.3 Relativistic Heavy Ion Collisions

It is believed that QGP had existed microseconds after the Big Bang. To look for the QGP and understand its properties, Relativistic Heavy Ion Collider (RHIC) was built to create key conditions at the beginning of the universe. During its twelve years of successful operation, RHIC has made many important discoveries. Among them there are two particular ones, namely, the jet quenching and the surprisingly large elliptic flow.

1.3.1 Jet quenching

High-p_T suppression of charged hadrons has been observed in 200 GeV central Au+Au collisions by studying the nuclear modification factor R_{AB} and R_{CP}, defined as:

$$R_{AB}(p_T) = \frac{d^2N_{AB}/dp_Tdy}{T_{AB}d^2\sigma_{pp}/dp_Tdy} \tag{1-2}$$

and

$$R_{CP}(p_T) = \frac{< N_{bin}^{Peripheral} > d^2N_{Central}/dp_Tdy}{< N_{bin}^{Central} > d^2N_{Peripheral}/dp_Tdy} \tag{1-3}$$

where $T_{AB} = \langle N_{bin} \rangle / \sigma_{pp}^{inel}$ is the "thickness function" of nuclear nuclear interactions, and N_{bin} is the total number of nucleon-nucleon collisions. Figure 1-4 shows the R_{CP} of hadrons as a function of p_T[7]. R_{CP} increases monotonically at low p_T region, reaches its maximum, and

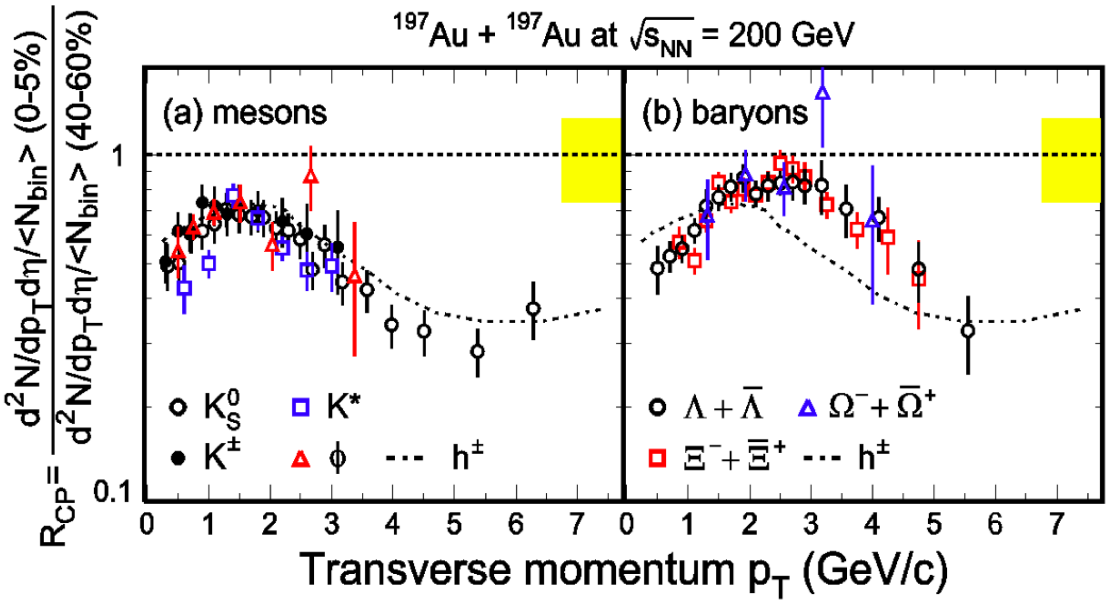

Figure 1-4: R_{CP} measured in 200 GeV Au+Au collisions as a function of transverse momentum for mesons (a) and hadrons (b).

then decreases at high p_T region, showing a suppression behavior for high-p_T particles. The left panel of Figure 1-5 depicts the R_{AB} versus p_T for 200 GeV central Au+Au collisions and d+Au collisions[21]. Suppression of high-p_T charged hadrons is observed in central Au+Au collisions, but not in d+Au collisions. Since high-p_T particles are produced by hard

scatterings at the initial stage of the collision, the suppression observed in central Au+Au events with respect to p+p and peripheral Au+Au events has been interpreted as the energy loss of the energetic partons penetrating the hot dense medium, a process that is called jet quenching. The jet quenching is not observed in d+Au collisions at RHIC energy, neither in Pb+Pb collisions at SPS energy[22].

High-p_T di-hadron azimuthal correlation measurement can be used as another tool to probe the parton energy loss in the hot dense medium. The right panel of Figure 1-5 compares the background-subtracted azimuthal distributions in 200 GeV p+p, d+Au, and central Au+Au collisions. Near-side peaks are similar in all three systems, while a strong suppression of away-side correlation relative to p+p, d+Au is seen in central Au+Au collisions. The dramatic suppression in away-side of back-to-back correlation indicates that a hot dense matter is created in central Au+Au system.

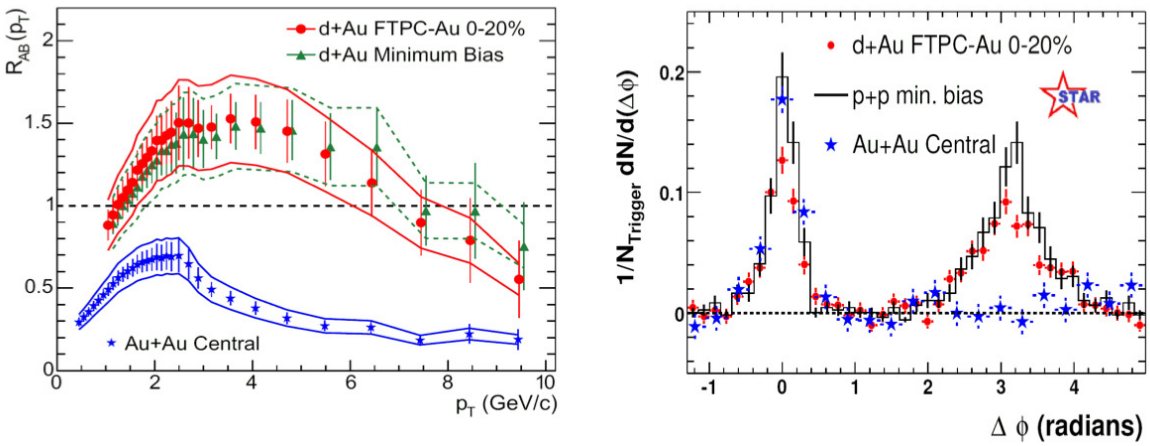

Figure 1-5: (Left panel) R_{AB} for minimum bias and central d+Au collisions, and central Au+Au collisions. (Right panel) Comparison of two-particle azimuthal distributions for central d+Au collisions to those seen in p+p and central Au+Au collisions.

1.3.2 Anisotropic flow

In non-central heavy ion collisions, two nuclei pass through each other at close to light speed, leaving behind an almond shape in the center of the mass region. This almond

shape reflects the overlapping geometry of the two nuclei. The matter at the center quickly expands because of the tremendous energy deposition. During the expansion, the multiple interaction converts the initial anisotropy in coordinate space into momentum space, forming an anisotropic flow. The anisotropic distribution of particles with respect to the reaction plane, defined by the beam and the line connecting the centroid of the two nuclei, can be written in a form of Fourier series:

$$E\frac{d^3N}{d^3p} = \frac{1}{2\pi}\frac{d^2N}{p_T dp_T dy}\left(1 + \sum_{n=1}^{\infty} 2v_n \cos[n(\phi - \Psi_r)]\right), \tag{1-4}$$

where Ψ_r is the azimuthal angle of the reaction plane, and ϕ is the azimuthal angle of emitted particles. Elliptic flow (v_2) is a sensitive probe of the local thermalization of the system. The top panel of Figure 1-6 shows the v_2 of K^0_S, $\Lambda + \bar{\Lambda}$, and charged hadrons ($h^{\pm}$)

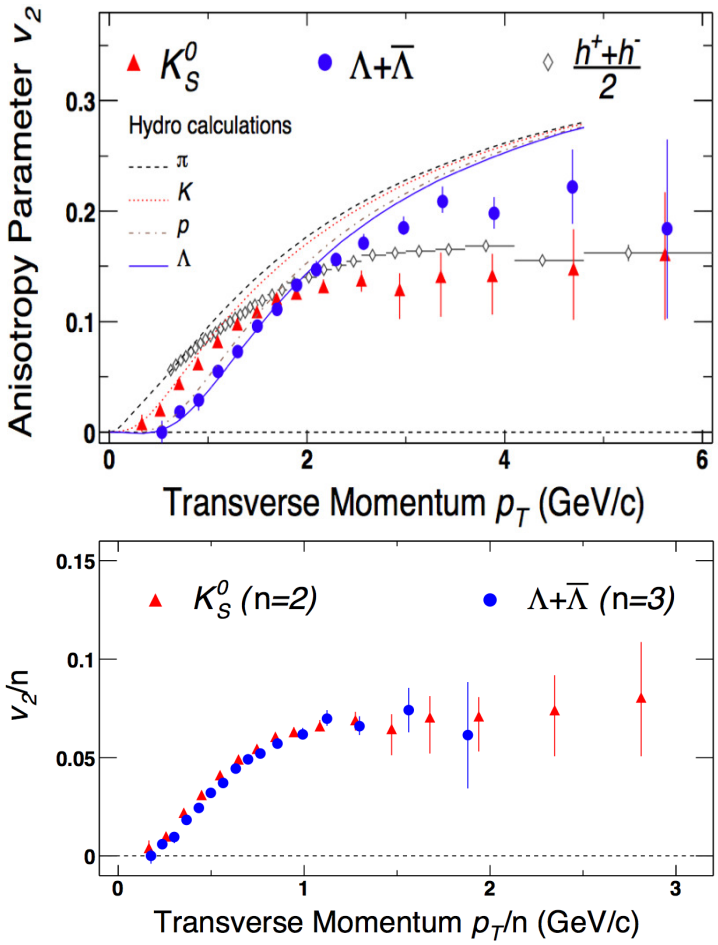

Figure 1-6: Elliptic flow, v_2 for K^0_S, $\Lambda + \bar{\Lambda}$ and charged ($h^{\pm}$) vs. p_T distribution (top panel), and v_2/n as a function of p_T/n for K^0_S and $\Lambda + \bar{\Lambda}$ (bottom panel).

as a function of p_T in 200 GeV Au+Au collisions[23]. The dashed lines indicate predictions from hydrodynamic model calculations. The plot shows a mass scaling with $p_T < 2$ GeV/c, and a classification of mesons and baryons in the intermediate p_T region. The mass scaling is interpreted as a result of the hydrodynamic mechanism of the system, while the meson-baryon classification can be characterized by the quark coalescence model (partonic flow) with finite partonic flow. The uniformity of v_2/n versus p_T/n for mesons and baryons (NCQ scaling), as shown in the bottom panel of Figure 1-6, with n being the constituent quark number, also supports the partonic flow mechanism [24].

1.4 Production of light (anti)nuclei in heavy ion collisions

1.4.1 Coalescence production

In heavy ion collisions, the coalescence process[16, 17, 25, 26] of light (anti)nuclei is historically described by the coalescence parameter B_A. Their differential invariant yield is related to the primordial yields of nucleons and is described by

$$E_A \frac{d^3N_A}{d^3P_A} = B_A (E_p \frac{d^3N_p}{d^3P_p})^Z (E_n \frac{d^3N_n}{d^3P_n})^{A-Z}, \tag{1-5}$$

where $E\frac{d^3N}{d^3P}$ stands for the invariant yields of nucleons or light (anti)nuclei, and A and Z are the atomic mass number and atomic number, respectively. P_A, P_p, and P_n denote their momentum, with $P_p = P_n = P_A/A$ assumed. The B_A can be written as:

$$B_A = A\frac{2s_A+1}{2^A} R_{np}^N (\frac{(2\pi\hbar)^3}{mV})^{A-1} \sim (1/V)^{A-1}, \tag{1-6}$$

where R_{np} is the neutron to proton ratio, s_A and m are the quantum number of spin and mass of a light (anti)nucleus, respectively. B_A is interpreted to be inversely related to the fireball volume in the coordinate space. Figure 1-7 shows the coalescence parameters of

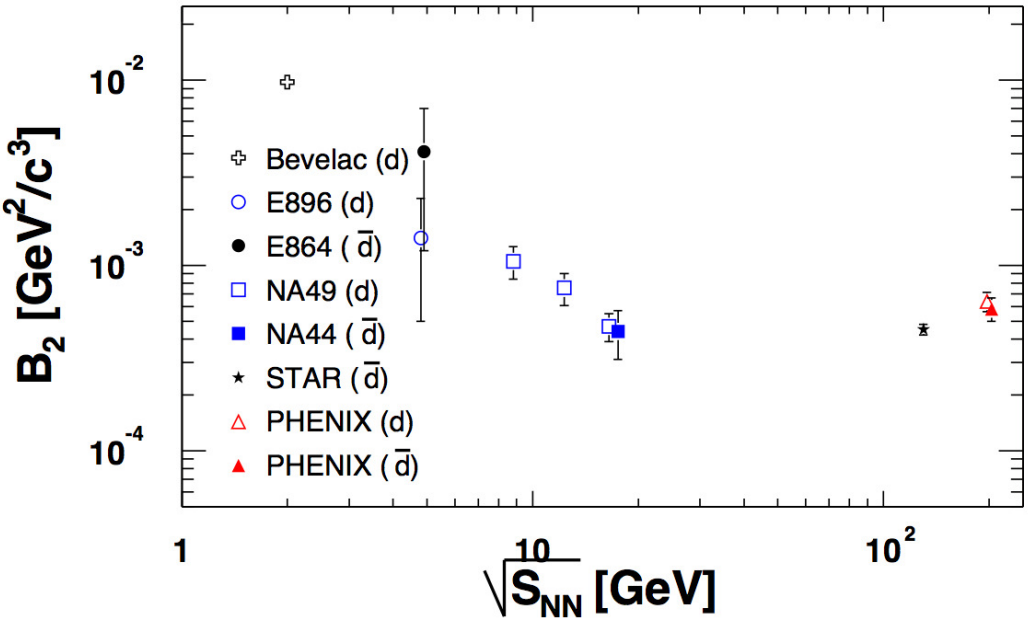

Figure 1-7: Coalescence parameter B_2 for d($\bar{\text{d}}$) extracted by various type of experiments at different energy scales.

d and $\bar{\text{d}}$ (B_2) extracted by various type of experiments at different energies. B_2 decreases dramatically with the increase of center-of-mass energies, indicating that a larger fireball volume is created at a higher energy.

1.4.2 Thermal production

In heavy ion collisions, the single particle spectra can be characterized by the Cooper-Frye formula[27]:

$$E\frac{d^3N_i}{d^3P} = \frac{2J+1}{(2\pi)^3}\int_{\Sigma_f} Pd^3\sigma(R)f_i(R,P), \tag{1-7}$$

where $2J+1$ is the spin degeneracy factor, and Σ_f is the kinetic freeze-out hypersurface. Based on the Boltzmann-Gibbs BlastWave model, which assumes that the local thermalization is achieved in the collision system, the phase space distribution function can be written as

$$f_i(R,P) = \exp(\frac{u^\nu p_\nu - \mu}{T}), \tag{1-8}$$

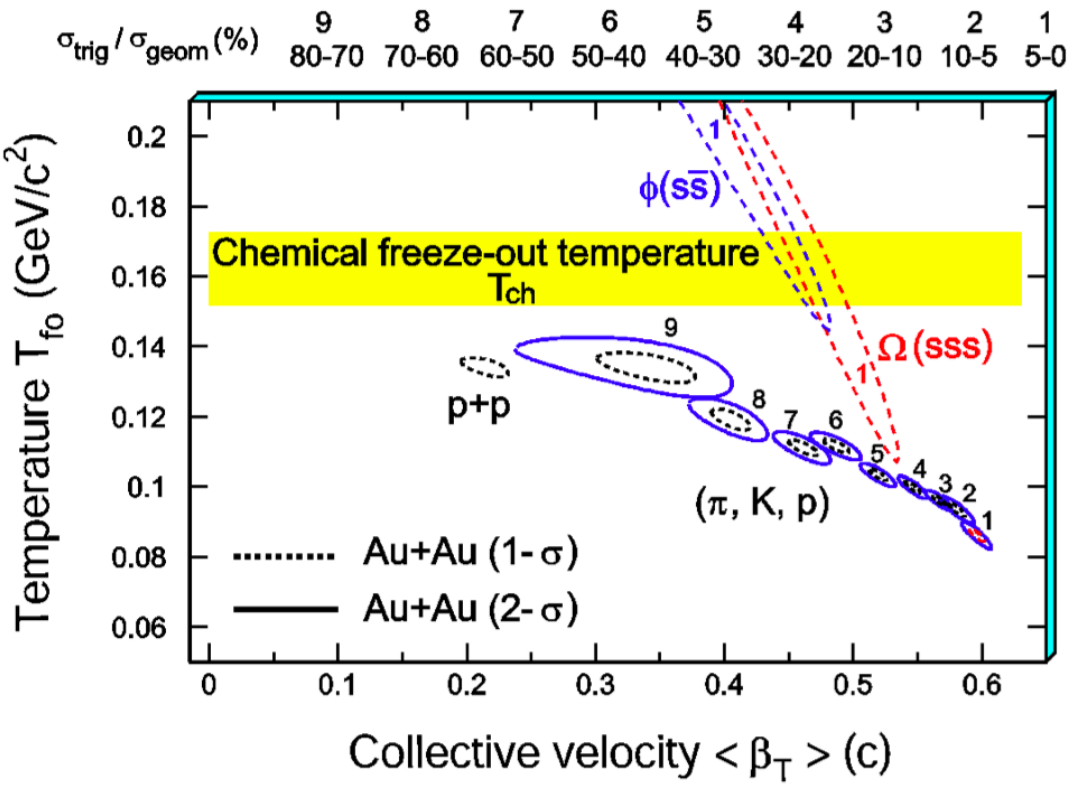

Figure 1-8: The χ^2 contours extracted by thermal + radial flow fits for π, K, and p and strange hadrons in 200 GeV p+p and Au+Au system[7].

with chemical potential $\mu = B\mu_B + S\mu_B$ (B and S are the baryon number and strangeness number respectively), local temperature T, and local four-velocity vector u^ν. Given equations 1-7 and 1-8, the m_T (p_T) spectra of a single particle can be written as:

$$\frac{dN}{m_T dm_T} \propto \int_0^R r dr m_T I_0(\frac{p_T \sinh\rho}{T}) K_1(\frac{m_T \cosh\rho}{T}), \tag{1-9}$$

where

$$\rho = tanh^{-1}\beta_r \ , \qquad \beta_r = \beta_s(\frac{r}{R})^n, \tag{1-10}$$

with flow velocities β_r and β_s at the position with a radius of r, and the hard-spherical edge (R) along the transverse radial direction, respectively. m_T is the transverse mass, T is the temperature at the kinetic freeze-out stage. I_0 and K_1 are modified bessel functions. Figure 1-8 shows the χ^2 contours extracted by fitting π, K, and p and strange hadrons in 200 GeV p+p and Au+Au system with formula 1-9. For ordinary particles (π, K, p), as the

collision become more and more central, the system develops a stronger collective flow, then it expands and cools at the kinetic freeze-out stage. On the other hand, strange hadrons (ϕ, Ω) reflect a higher kinetic freeze-out temperature, although with a large uncertainty. That means the substantial radial flow velocity for ϕ and Ω would be accumulated prior to chemical freeze-out, giving the multi-strange hadrons greater sensitivity to the dynamics in the early stages of the system evolution[7].

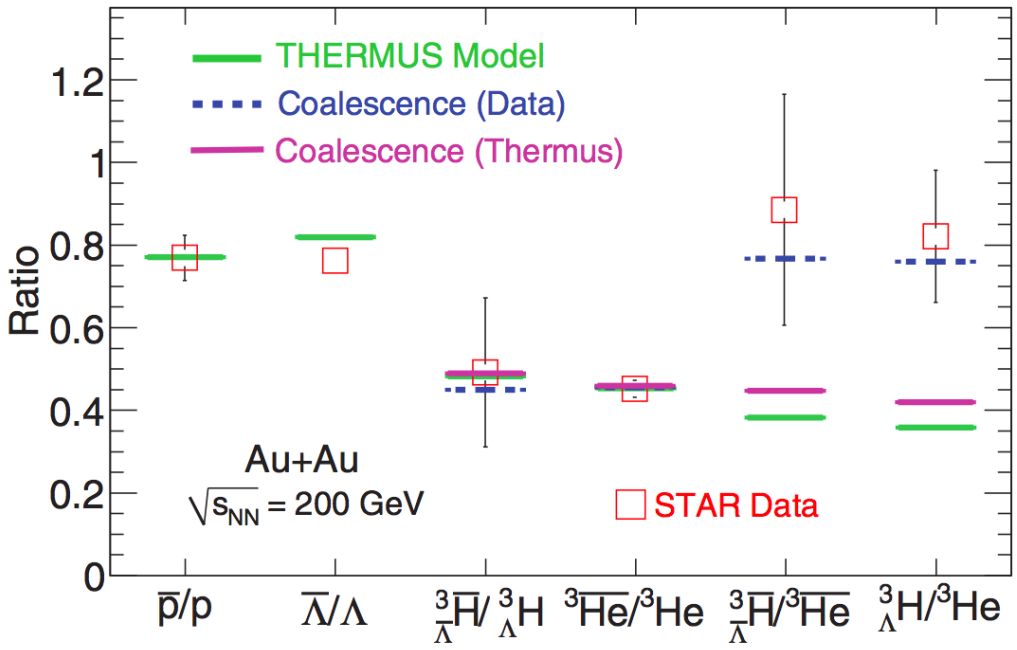

Figure 1-9: Comparison of results from STAR experiment and the thermal model and coalescence model predictions in Au+Au 200 GeV collisions.

In thermodynamic model, a light (anti)nucleus is regarded as an object with energy emitted by the fireball with $E = |B|m_p$, where B is the atomic mass number, and m_p is the mass of proton. The production probability is determined by the Boltzmann factor $e^{-E/T}$. Figure 1-9 shows the comparison between model predictions and data for particle-ratios in Au+Au collisions at RHIC energy[32, 33]. The thermal model describes the antiparticle to particle ratios quite well, but underestimates the ratios of ${}^{3}_{\Lambda}\overline{\mathrm{H}}/{}^{3}\overline{\mathrm{He}}$ and ${}^{3}_{\Lambda}\mathrm{H}/{}^{3}\mathrm{He}$[32]. Figure 1-10 depicts the energy dependence of ${}^{3}_{\Lambda}\mathrm{H}/{}^{3}\mathrm{He}/(\Lambda/\mathrm{p})$ and ${}^{3}\mathrm{He}/{}^{3}H$ ratios. The ${}^{3}\mathrm{He}/{}^{3}\mathrm{H}$

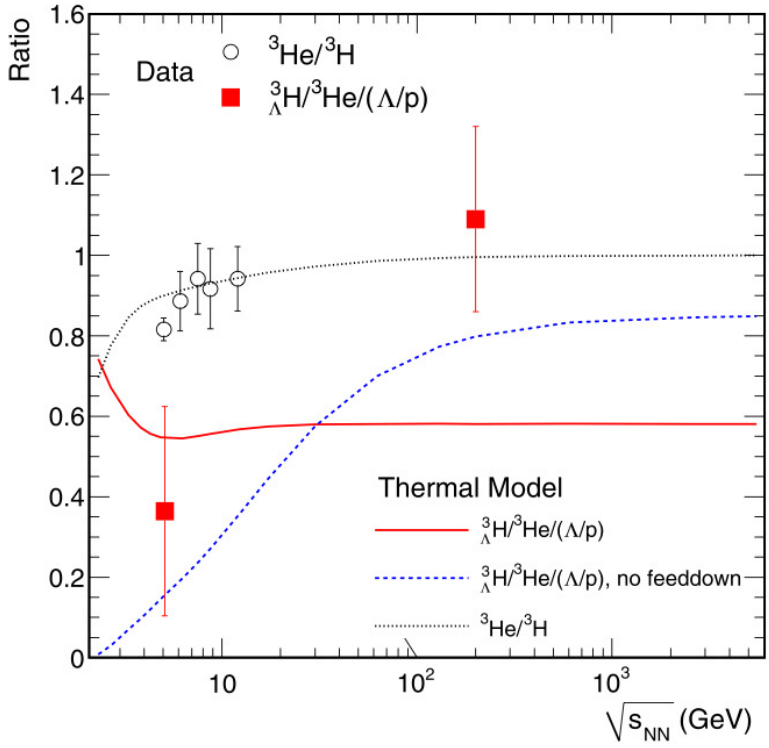

Figure 1-10: Energy dependence of nuclei and hypernuclei production ratios, data points are taken from[28–31], solid and dashed lines stands for the thermal calculations.

ratios are well reproduced by the thermal model at AGS energy, and the correction of the feed-down contribution to Λ and p[33], which is denoted by the blue dashed line, is essential for the $^3_\Lambda$H/^{3}He/(Λ/p) calculation.

1.4.3 STAR's previous measurement on light (anti)hypernuclei : $^3_\Lambda$H and $^3_{\overline{\Lambda}}\overline{\mathrm{H}}$

The first observation of a hypernucleus was reported in 1952 using a nuclear emulsion cosmic detector [34]. However, the detection of the first antihypernucleus, $^3_{\overline{\Lambda}}\overline{\mathrm{H}}$, consisting of one $\overline{\mathrm{n}}$, one $\overline{\mathrm{p}}$ and one $\overline{\Lambda}$, was not made until 2010 [31]. The study of (anti)hypernuclei in heavy ion collisions is essential for the understanding of the interaction between nucleon and hyperon (Y-N interaction), which plays an important role in the explanation of the structure of neutron stars. Furthermore, the lifetime of a (anti)hypernucleus depends on

the strength of the Y-N interaction. Therefore, the precise measurement of the lifetime of (anti)hypernuclei provides the information of Y-N interaction. On the other hand, the measurement of the lifetime of antihypernuclei leads to a precise test of the CPT symmetry law between antimatter and matter in the future. Figure 1-11 shows the invariant mass distribution of ${}^{3}_{\Lambda}\mathrm{H}$ and ${}^{3}_{\Lambda}\overline{\mathrm{H}}$ reconstructed via decay channel ${}^{3}_{\Lambda}\mathrm{H}\rightarrow{}^{3}\mathrm{He}+\pi^{-}$ and ${}^{3}_{\Lambda}\overline{\mathrm{H}}\rightarrow{}^{3}\overline{\mathrm{He}}+\pi^{+}$ based on the conservation of momentum and energy[31, 35]. The best fit to the spectrum indicates that the mass peak is located at 2.991 GeV/c^2 with a significance of 4.1 σ for ${}^{3}_{\Lambda}\overline{\mathrm{H}}$, and corresponding significance for ${}^{3}_{\Lambda}\mathrm{H}$ signal is 5.2 σ.

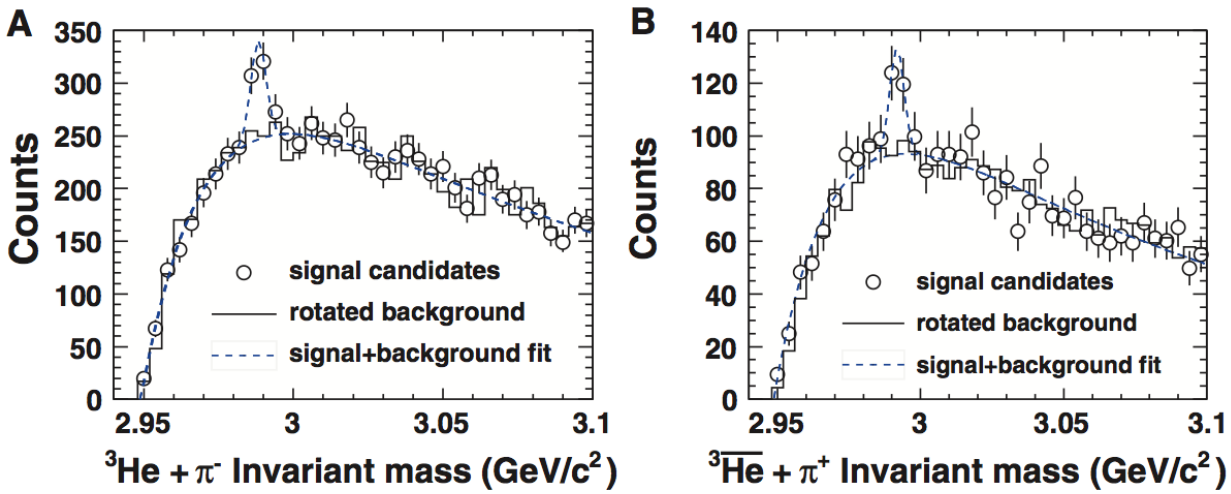

Figure 1-11: Reconstructed invariant mass distribution of the daughter ${}^{3}\mathrm{He}({}^{3}\overline{\mathrm{He}})$ and π^- (π^+). Open circles represent for the signal distribution. Solid lines are the combinatorial background distributions. Blue dashed lines are the Gaussian (signal) plus double exponential (background) function fit.

Strangeness enhancement in nucleus-nucleus collisions is regarded as a sensitive probe of the formation of QGP[36]. This effect leads to a high production rate of ${}^{3}_{\Lambda}\mathrm{H}$ (${}^{3}_{\Lambda}\overline{\mathrm{H}}$) due to the equilibration among strange quarks and light quarks. The strangeness population factor

$$S_3 = {}^{3}_{\Lambda}H/({}^{3}He \times \Lambda/p), \tag{1-11}$$

is defined to distinguish the QGP phase and the pure hadronic phase in heavy ion collisions. Figure 1-12 depicts the excitation function of particle ratios for the STAR data and other previous measurements[28–30]. The S_3 value is close to unity at RHIC energy, while only

about 1/3 at AGS energy, indicating that the phase space population of strange quarks are comparable with light quarks at RHIC.

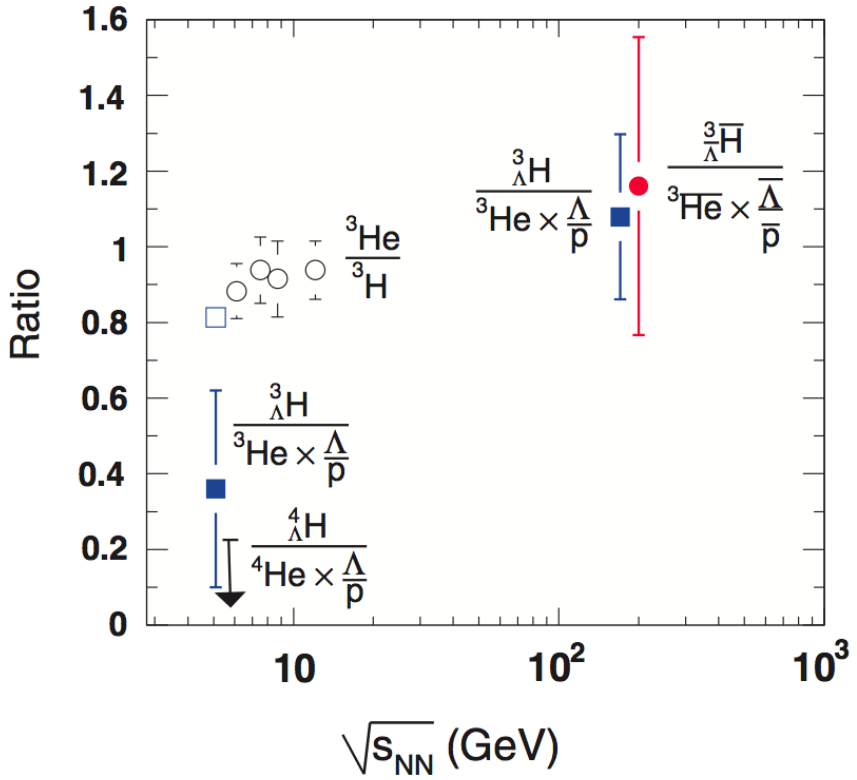

Figure 1-12: Particle ratios versus center-of-mass energy per nucleon-nucleon collision. The data points besides this measurement are taken from Refs[28–30].

1.5 Thesis structure and organization

We implemented an online High Level Trigger (HLT) at the STAR experiment, and with data taken by the HLT we observed 16 $^{4}\overline{\mathrm{He}}$ nucleus in Au+Au collisions at 200 GeV and 62 GeV. This thesis will present the development and performance of the HLT, the $^{4}\overline{\mathrm{He}}$ identification base on the Time Projection Chamber (TPC) and Time Of Flight (TOF) detector, $^{4}\overline{\mathrm{He}}$ background estimation, as well as the phenomenological study of the formation mechanism of light (anit)nuclei. This thesis is arranged as follows:

Chapter 1: Introduction

Chapter 2: The STAR Experiment

Chapter 3: The STAR High Level Trigger

Chapter 4: Observation of the $^4\overline{\mathrm{He}}$ ($\overline{\alpha}$) nucleus

Chapter 5: Coalescence production of light (anti)nuclei

Chapter 6: Conclusion and Outlook

Chapter 2 The STAR Experiment

2.1 The Relativistic Heavy Ion Collider

The construction of the Relativistic Heavy Ion Collider (RHIC) at Brookhaven National Laboratory started in 1991, and the first collision was made in the summer of 2000. During the course of thirteen years of successful operation, RHIC had collided ions including Au+Au, p+p, d+Au, Cu+Au, and U+U at various energies. Thanks to the continuous upgrades in the past decade, RHIC has far overpassed its designed luminosity. As of today it can deliver a luminosity of 5.0×10^{27} cm^{-2}s^{-2} in Au+Au 200 GeV collisions, 5.2×10^{31} cm^{-2}s^{-2} in p+p 200 GeV collisions, and 2.0×10^{32} cm^{-2}s^{-2} in p+p 500 GeV collisions.

The RHIC complex was designed to produce, accelerate and store the heavy ion beams. It consists of two superconducting storage rings installed side-by-side, which intersect at six interaction points. The Tandem Van de Graaff accelerators, the Booster Synchrotron and the Alternating Gradient Synchrotron (AGS), are combined to serve as an injector. For the case of preparing Au beams, the Pulsed Sputter Ion Source generates Au atoms with a charge of -1 e in the Tandem Van de Graaff accelerators, leaving a beam with net charge of

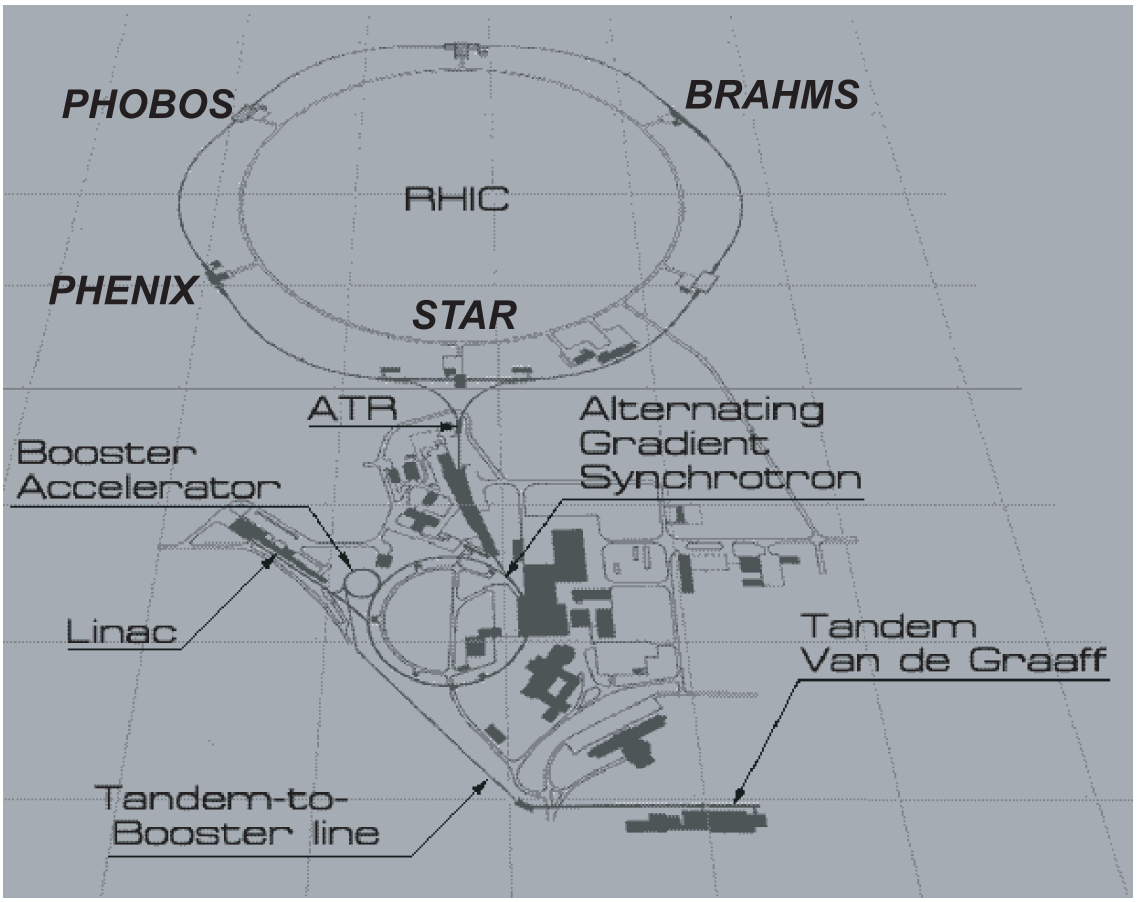

Figure 2-1: Relativistic Heavy Ion Collider at Brookhaven National Lab.

+32 e, and beam energy at 1 MeV/nucleon. Then, the beam is transferred to booster, where the Au atoms is accelerated to 95 MeV/nucleon, and stripped to a net charge of +77 e. In AGS, the Au beam is further accelerated to 8.86 GeV/nucleon, and with a net charge of +79 e. Finally, the beam is injected into RHIC, and further accelerated to collision energy.

Out of the six collision points, four of them are occupied by different experimental facilities. They are STAR at 6:00 o'clock, PHENIX at 8:00 o'clock, and PHOBOS and BRAHMS at 10:00 and 2:00 o'clock, respectively. Data analyzed in this thesis are Au+Au collisions at 200 GeV and 62 GeV taken by the STAR experiment in year 2010.

2.2 The STAR Detector

The STAR (Solenoidal Tracker At RHIC) detector complex consists of a set of sub-

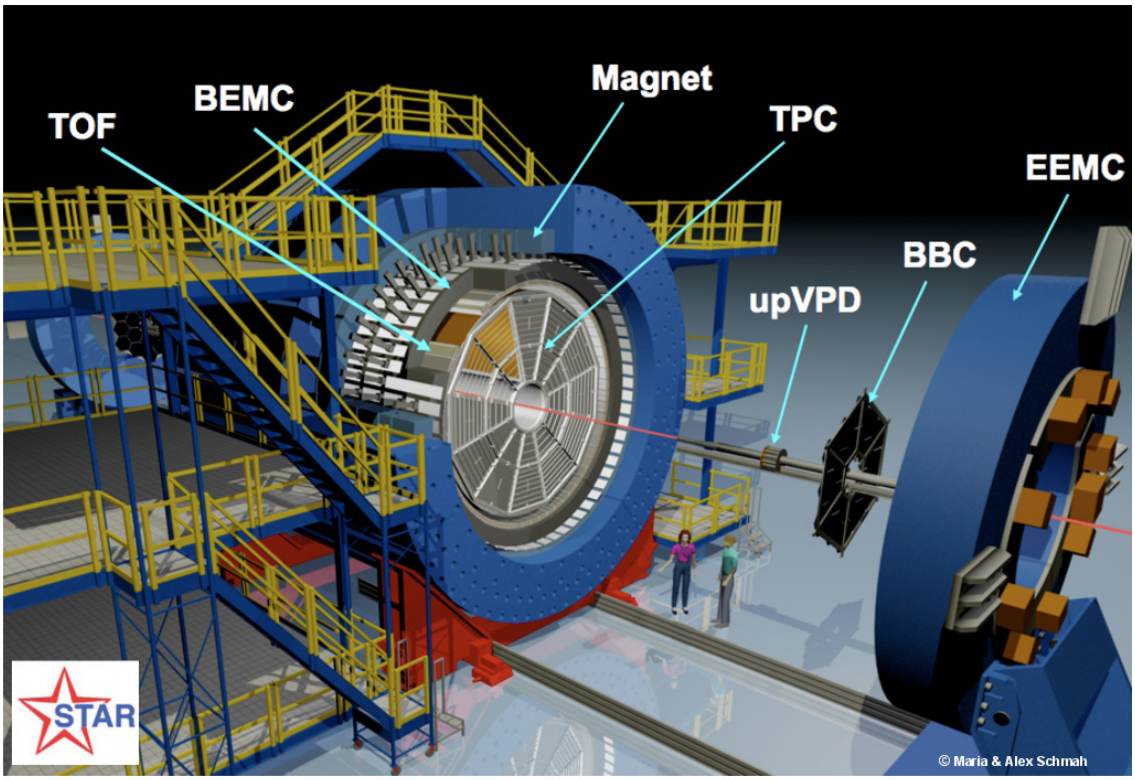

Figure 2-2: A three-dimensional rendering of STAR detector.

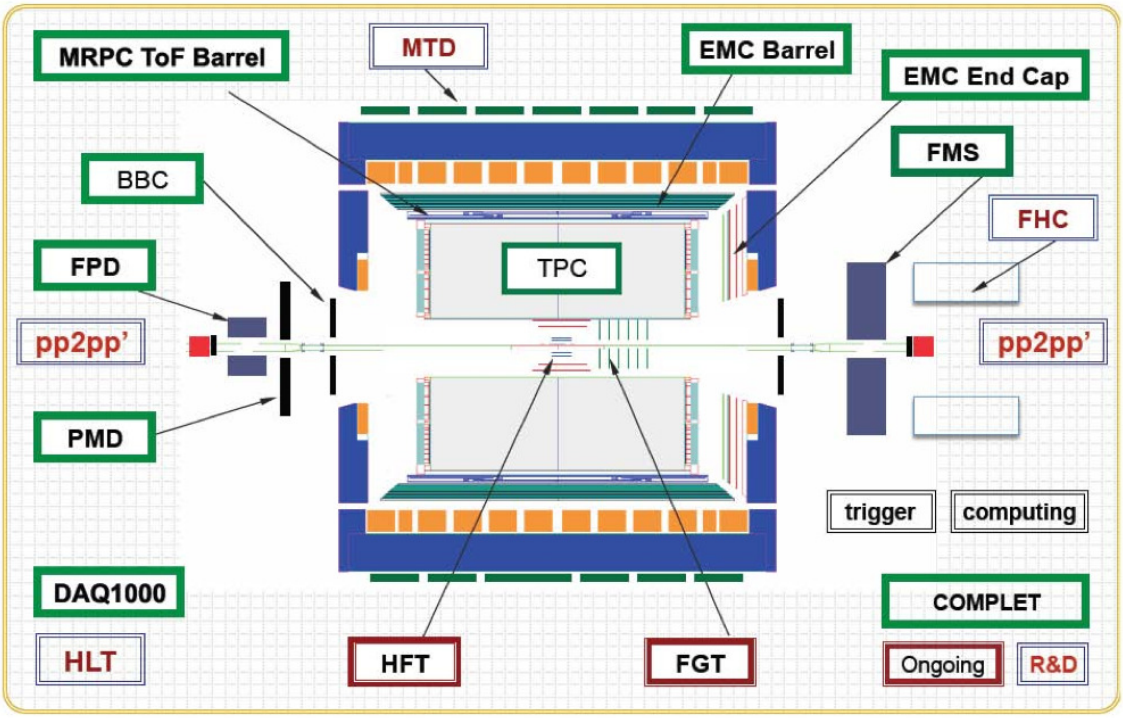

Figure 2-3: A side-view of STAR detector.

systems, including the Time Projection Chamber (TPC) for reconstructing tracks at mid-rapidity region($|\eta| < 1.2$), and a pair of radial-drift Forward TPC (FTPC) (only in for early runs) for reconstructing tracks at forward rapidity $2.5 < |\eta| < 4.0$, Time-Of-Flight detector (TOF) for the measurement of particle's traveling time, Barrel ElectroMagnetic Calorimeter (BEMC) and Endcap ElectroMagnetic Calorimeter (EEMC) to calculate the deposited energy. Other sub-detectors that are not crucial for our analysis include, the Muon Telescope Detector (MTD), Beam Beam Counters (BBC), Zero Degree Calorimeters (ZDC), pseudo-Vertex Position Detectors (pVPDs), Ring-Imaging Cerenkov Retector (RICH), and Forward Hadron Calorimeter (FHC). With all subsystems combined, the STAR detector complex has a large and uniform acceptance with excellent tracking and particle identification capabilities.

2.2.1 Magnet

STAR detector complex sits in a strong magnetic field produced by STAR magnet[37]. The magnet is a cylindrical-like device, with 6.85 m along the longitudinal direction, 5.27 m for inner diameter and 6.28 m for outer diameter along the radial direction. It provides a nearly uniform magnet field ranging from 0.25 T to 0.5 T, along the beam direction. The maximum excursion of the radial component for full (half) field is approximately $\pm$50 Gauss ($\pm$25 Gauss), and the ϕ component of the field is less than $\pm$3 Gauss ($\pm$1.5 Gauss). The maximum radial and angular variations of the field integrals are $|\Im_r| < 0.30$ cm and $|\Im_\phi| < 0.035$ cm over the entire TPC volume. Where $|\Im_r|$ and $|\Im_\phi|$ are defined as

$$|\Im_r| \equiv |\int_{z'=210cm}^{z} (B_r/B_{z'})dz'| \tag{2-1}$$

$$|\Im_\phi| \equiv |\int_{z'=210cm}^{z} (B_\phi/B_{z'})dz'| \tag{2-2}$$

2.2.2 Time Projection Chamber

The Time Projection Chamber (TPC) is the primary tracking device of STAR[38]. It records the tracks of particles, and identifies them by correlating their ionization energy loss ($\langle dE/dx \rangle$) and momentum. Its acceptance covers ± 1.8 units of pseudo-rapidity with full azimuthal angle. The TPC is shown schematically in Figure 2-4. It is 4.2 m long 4 m in diameter, filled with P10 gas and divided into two drift chambers by central membrane, and with a uniform electric field of 135 V/m. The uniformity of electric field is critical since the track reconstruction precision is of sub-millimeter and electron drift paths are up to 2.1 meters. The paths of primary ionizing particles passing through the gas volume are reconstructed with high precision from the released secondary electrons which drift to the readout end-caps at the ends of the chamber.

Number of Anode Sectors	24
Number of Pads	136608
Cathode Potential	28 kV
Drift Gas	P10
Pressure	Atmospheric + 2 mbar
Signal to Noise Ratio	20:1
Drift Velocity	5.45 cm/μs
Transverse Diffusion (σ)	230 μm/$\sqrt{cm}$
Longitudinal Diffusion (σ)	360 μm/$\sqrt{cm}$

Table 2-1: Basic parameters for STAR TPC.

The end-cap readout planes of STAR closely match the designs used in other TPCs such as PEP4, ALEPH, EOS and NA49, but with some refinements to accommodate the high track density at RHIC and some other minor modifications to improve the reliability and simplify the construction. The TPC has 12 sectors arranged as on a clock around the circle. The sectors are installed inside the support wheel so that there are only 3 mm spaces between the sectors, which reduce the undetectable area as much as possible.

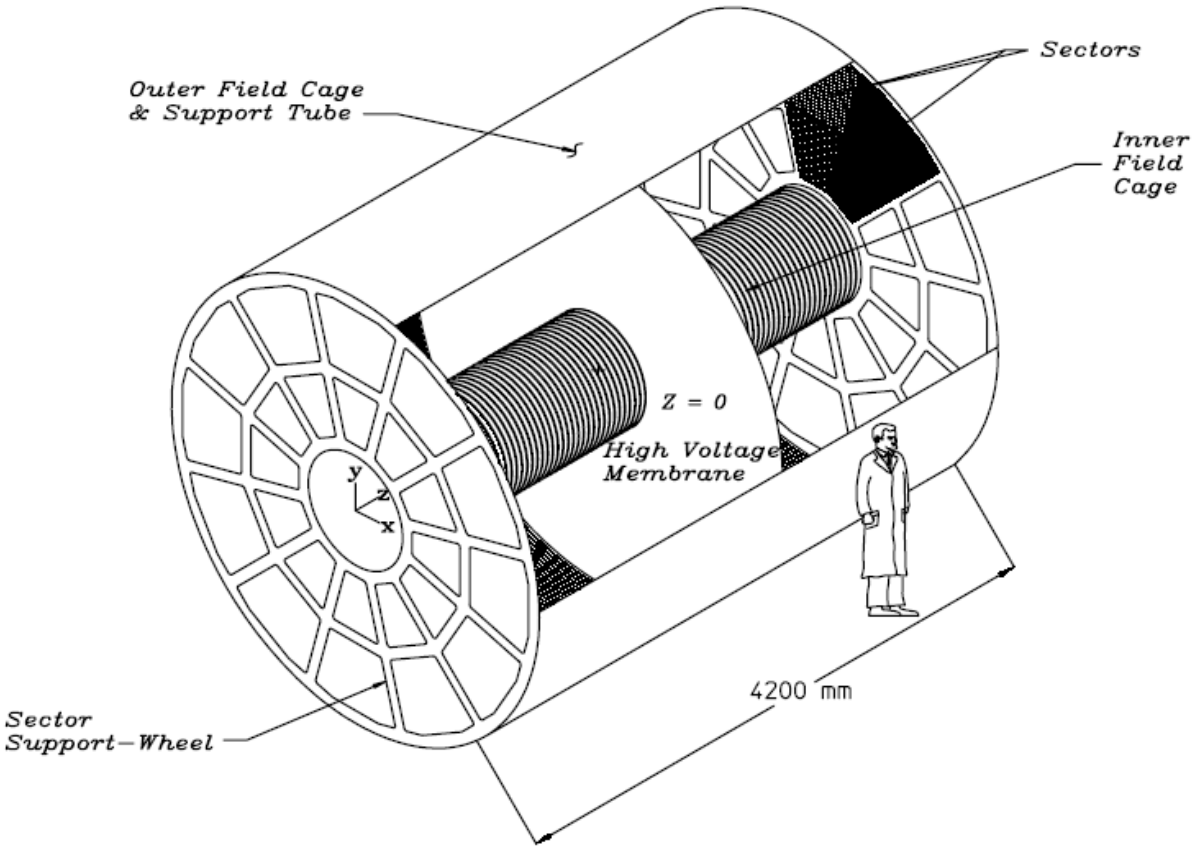

Figure 2-4: STAR Time Projection Chamber.

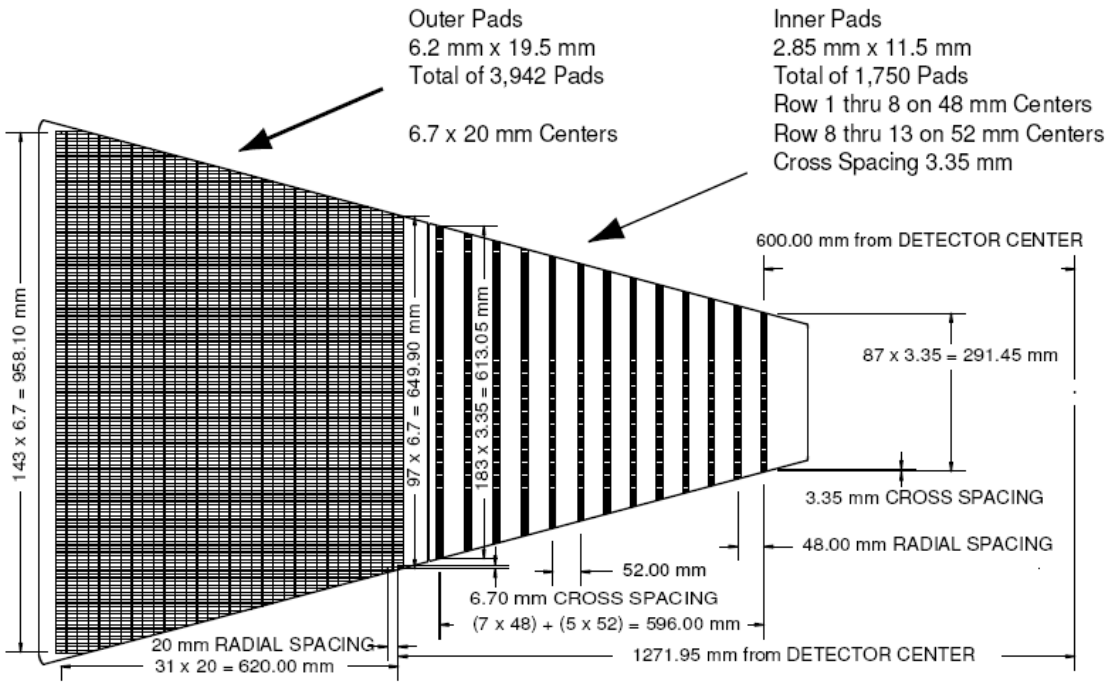

Figure 2-5: The anode pad plane of one full sector of STAR TPC.

The readout system is based on the Multi Wire Proportional Chambers (MWPC) with readout pads. The chambers consist of four components: a pad plane and three wire planes as seen in Figure 2-6. The amplification layer is composed of the anode wire plane of wires with the pad plane on one side and the ground wire plane on the other. The third wire plane is a gating grid. The drifting electrons avalanche in the high fields at the 20 μm anode wires providing an amplification of 1000 to 3000.

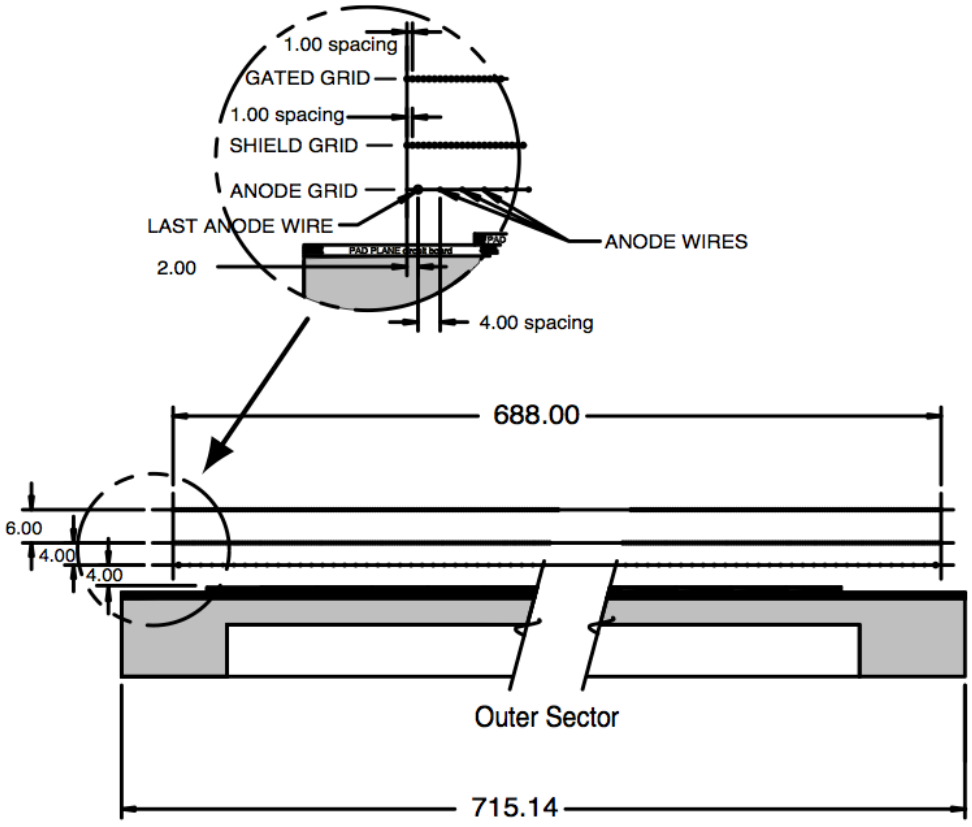

Figure 2-6: A cutaway view of an outer sub-sector pad plane.

2.2.3 dE/dx calibration and particle idendification

The TPC dE/dx measurement relies on the gas gain, which has a strong dependence on the pressure and high voltage applied. Extra variations come from difference in gain between sectors and pad rows. The goal of dE/dx calibration is to reduce or eliminate correlations on those variables, and improve dE/dx resolution. The ionization energy loss

of high-energy particles follows the Landau distribution. Experimentally, mean energy loss $\langle dE/dx \rangle$[39] is calculated using the "truncated mean method" and the "likelihood method" for particle identification. Figure 2-7 shows the preliminary result of $\langle dE/dx \rangle$ resolution as a function of particle track length. The truncated mean method gives a resolution of 7.49% with a track length of 76 cm.

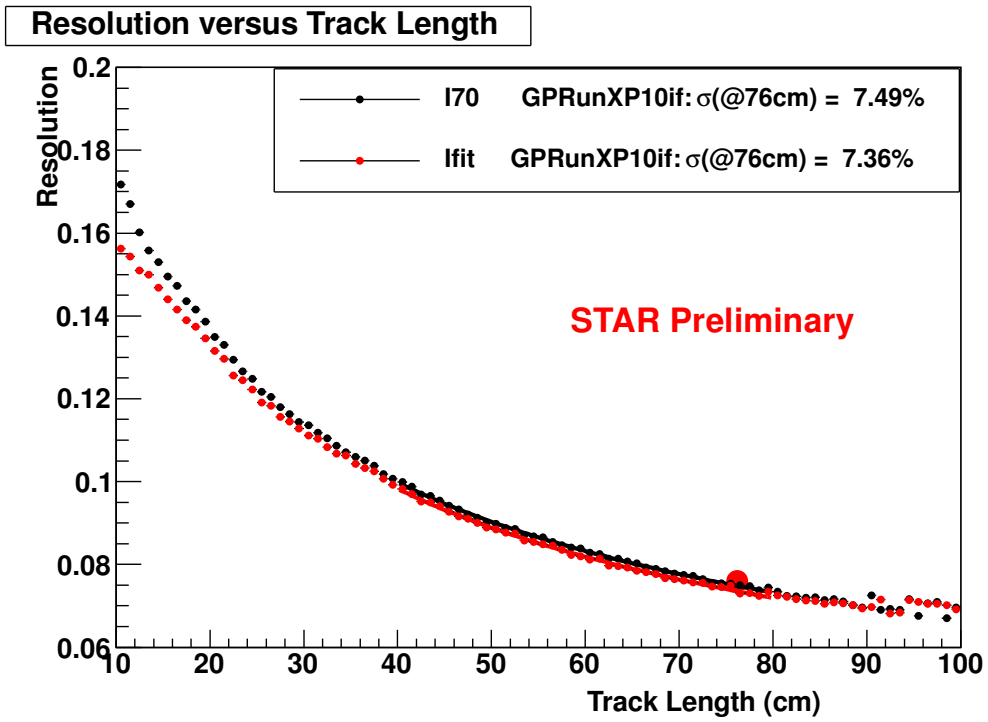

Figure 2-7: dE/dx resolution in Au+Au 200 GeV as a function of track length after calibration.

The mean energy loss $\langle dE/dx \rangle$ of a charged particle with charge z (in units of e), speed $\beta = v/c$ can be described by Bethe-Bloch formula[40]:

$$\langle \frac{dE}{dx} \rangle = 2\pi N_0 r_e^2 m_e c^2 \rho \frac{Z z^2}{A\beta^2} [\ln \frac{2m_e \gamma^2 v^2 E_M}{I^2} - 2\beta^2], \tag{2-3}$$

where ρ is the density of the medium, N_0 is the Avogadro number, m_e is the electron mass, $r_e = e^2/m_e$ is the classical electron radius, c is the speed of light, Z is the atomic number of the absorber, A is the mass number of the absorber, $\gamma = 1/\sqrt{1-\beta^2}$, and I is the mean excitation energy. $E_M = 2m_e c^2 \beta^2/(1-\beta^2)$ is the maximum transferable energy in a single collision. The mean energy loss as a function of track momentum from STAR

TPC is shown in Figure 2-8. It shows that different charged particle species with same momentum have different energy loss when passing through the TPC. Charged pions and kaons can be identified up to ~ 0.7 GeV/c and protons and anti-protons can be identified up to ~ 1.1 GeV/c. Furthermore, using the secondary vertex reconstruction technique, STAR TPC can identify many resonances, such as K^0_S, and Λ up to ~ 7.0 GeV/c, and K^*, ϕ, and Δ to ~ 5.0 GeV/c.

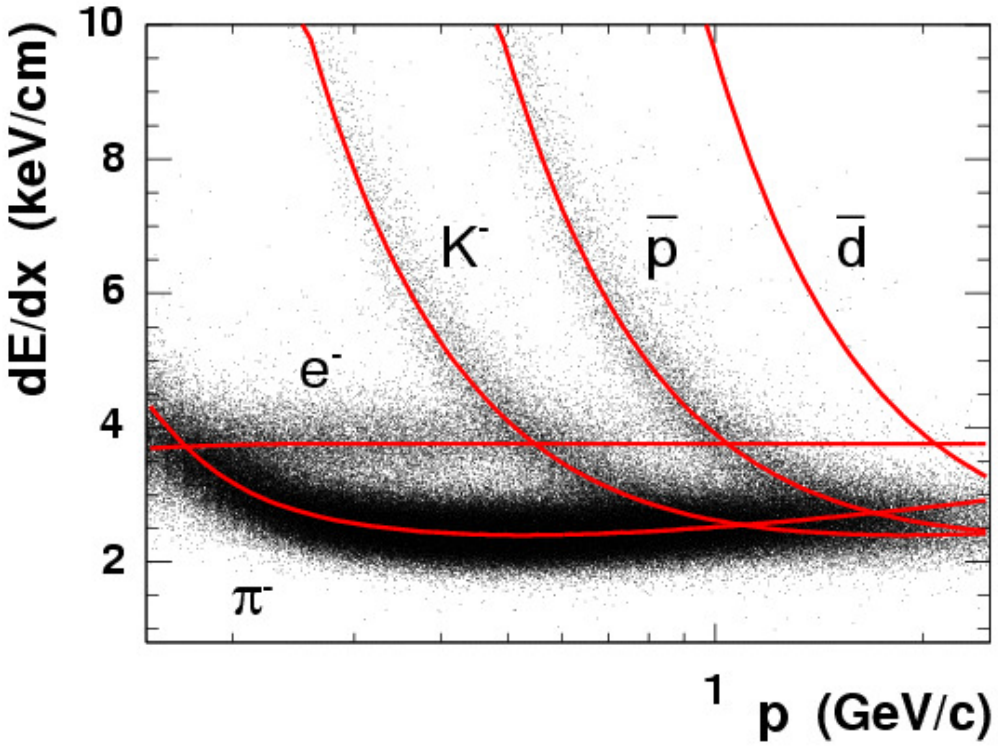

Figure 2-8: Energy loss $\langle dE/dx \rangle$ for charged particles in TPC

2.2.4 Time Of Flight

The STAR Time Of Flight (TOF) consists of 120 trays, with 60 of them on the east side and the others on the west side. For each tray, it is 240 cm long, 21.3 cm wide, and 8.5 cm thick. It has 32 modules, and each module has 6 pads. In total the TOF has 23040 pads, with an overall coverage of ~ 60 m^2[41–43]. The TOF detector relies on the Multi-gap Resistive Plate Chamber technique, which is capable of sub one hundred picoseconds time

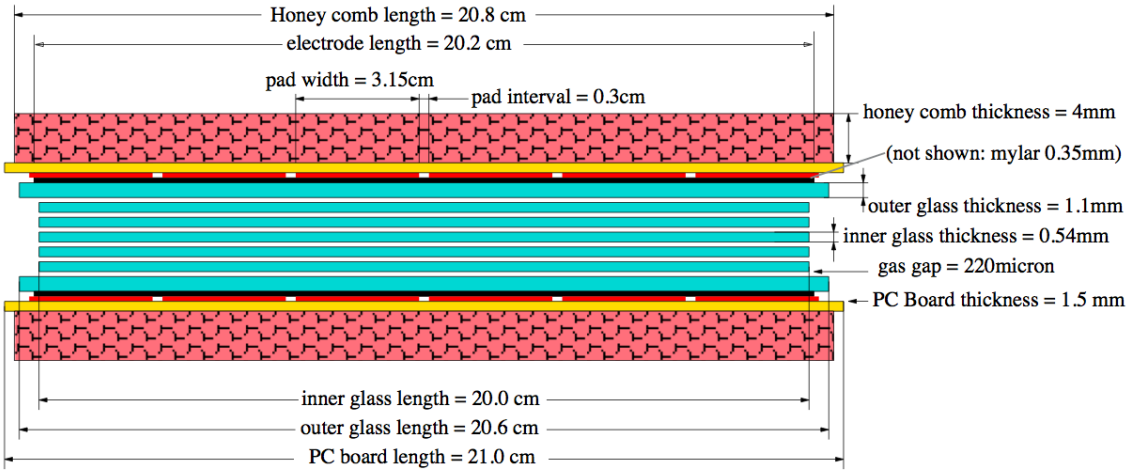

Figure 2-9: A side view of the long edge of a MRPC module

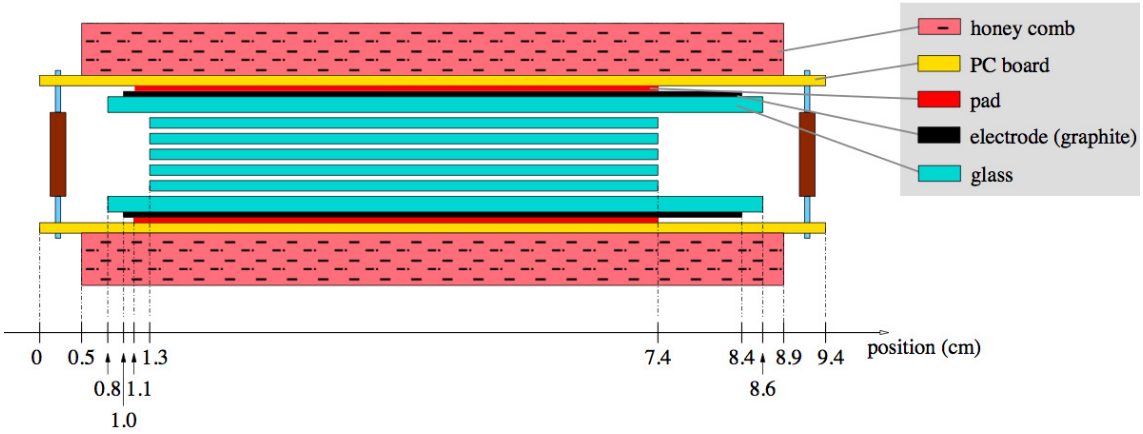

Figure 2-10: A side view of the short edge of a MRPC module.

resolution and high detection efficiency ($> 95\%$) for minimum ionizing particles[44]. Figure 2-9 and 2-10 show two side-views of the long and short edge of a MRPC module. A MRPC module is a stack of resistive glass plates with a series of uniform gas gaps. The outer and inner glass plates are 20.6 cm and 20 cm long, 7.6 cm and 6.1 cm wide, 1.1 mm and 0.54 mm thick, respectively. They are parallel to each other with nylon fishing lines as a partition. By applying a high voltage at the external electrodes, a high electric field is created in each sub gap, and all the internal plates are electrically floating. Charged particles generate avalanches in the sub gaps, when passing through the chamber. The read-out system records the induced signal on the pad, and calculates the arriving time of tracks. Figure 2-11 shows

the inverse velocity ($1/\beta$) calculated from TOF as a function of momentum calculated from TPC tracking in 200 GeV d+Au collisions. The separation between pions and kaons up to p_T = 1.6 GeV/c, and kaons and protons up to p_T = 3.0 GeV/c are achieved, respectively [45, 46].

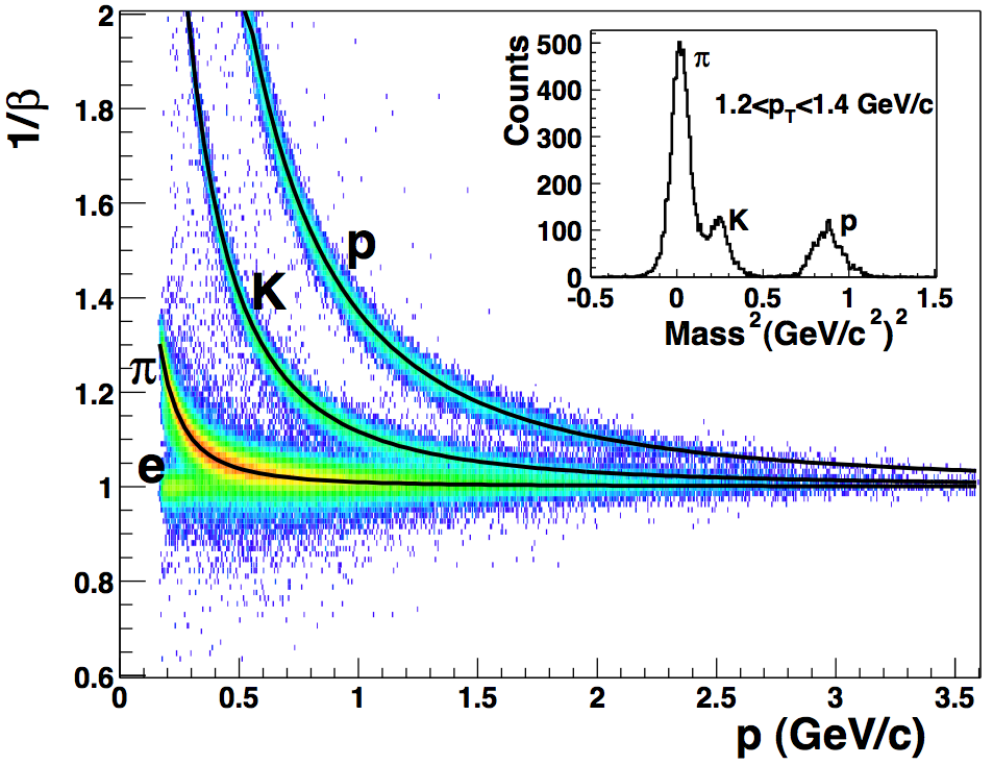

Figure 2-11: $1/\beta$ vs. momentum for pion, kaon, and proton from 200 GeV d+Au collisions. The inserted plot shows $m^2(m^2 = p^2(1/\beta^2 - 1))$ for 1.2 GeV/c < p_T < 1.4 GeV/c.

2.2.5 Trigger System

The STAR trigger system is based on a set of fast detectors, which includes ZDC, pVPD, TOF/CTB, BEMC, and BBC. The event selection relies on the measurement of the event multiplicity and energy distribution in pseudo-rapidity (η) and azimuth angle (ϕ). The multiple level structure of the trigger system is based on TPC timing considerations, and consists of a Level 0 selection followed by Level 1, Level 2, and High Level Trigger for analysis and rejection. Each detector channel is digitized for every RHIC crossing and fed into a Data

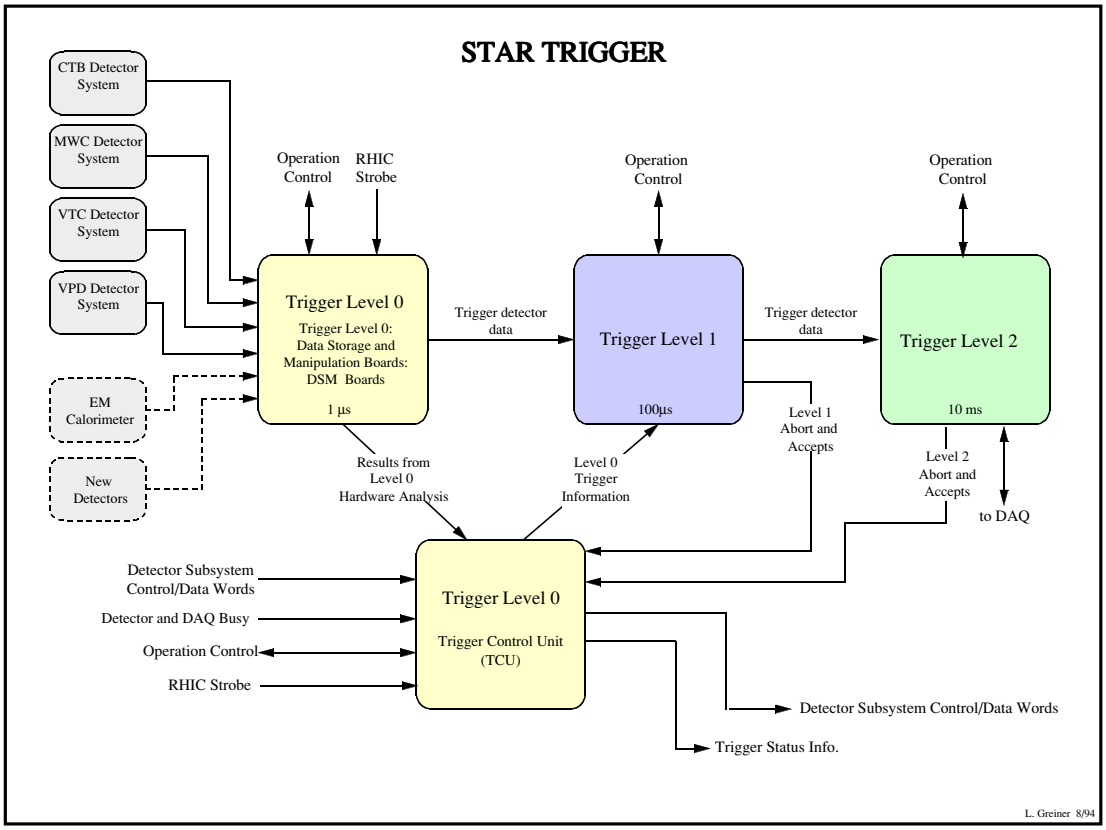

Figure 2-12: The STAR trigger system.

Storage and Manipulation (DSM) board where it is analyzed and combined with the other signals in a multi-layer pipeline that forms a fast decision tree. The DSM based decision tree constitutes Level 0 of the trigger and is constrained to issue a decision within 1.5 μs from the time of the interaction, as shown in Figure 2-12. While the amplification/digitization cycle is proceeding in the slow detectors, the data from fast detectors can be further analyzed during this storage period to decide whether a selected event should be rejected or passed to the next level of analysis at Level 1. This time allocation is set somewhat arbitrarily at 100 μs for Level 1 analysis. If this event is rejected, it takes a few μs for the TPC electronics to reset itself to be ready to accept another event. During Level 2 stage, network bandwidth allows all data from the trigger detectors to be moved to a central location for

further analysis. Simultaneously, additional summary data from other fast detectors (EMC, TOF) can be added to this trigger data to determine whether the event should be kept or rejected [47]. All of the raw trigger detector data and the results from Level 1 and Level 2 analyses are packaged and sent to the Data Acquisition System (DAQ) system. When TPC data is digitized and ready to read into the event builder, STAR High Level Trigger[9] collects information from subsystems and reconstruct an event. The event will be analyzed online and a trigger decision will be made.

Chapter 3 The STAR High Level Trigger

In year 2010, RHIC delivered a luminosity of 5.0×10^{27} cm^{-2}s^{-2} for Au+Au 200 GeV collisions, 5.2×10^{31} cm^{-2}s^{-2} for p+p 200 GeV collisions, and 2.0×10^{32} cm^{-2}s^{-2} for p+p 500 GeV collisions. To cope with the enormous beam intensities, STAR has upgraded the Data Acquisition System (DAQ1000). The enhanced capability of data taking imposes a great challenge for STAR computing in terms of CPU time and tape storage. However, a small portion of the data is of great physics interest, e.g., heavy flavor, high-p_T, di-electrons, exotics, and ultra peripheral collisions. In order to assure timely physics output of these physics topics, it is much desired to design and implement a High Level online Trigger (HLT) that can reduce the amount of data written to tape while maintaining a high sampling rate thus fully utilizes the delivered luminosity.

3.1 Architecture

STAR HLT collects data from tracking device (TPC) and other fast detectors (BEMC, TOF), as well as reconstructs events and makes decisions. The HLT consists of two parts, one is called Sector Level 3 (SL3), and the other, Global Level 3 (GL3). The schematic configuration of HLT is presented in Figure 3-1. The SL3 does the sector tracking on DAQ's CPU. The advantage of tracking with DAQ machines is that data is already in the memory,

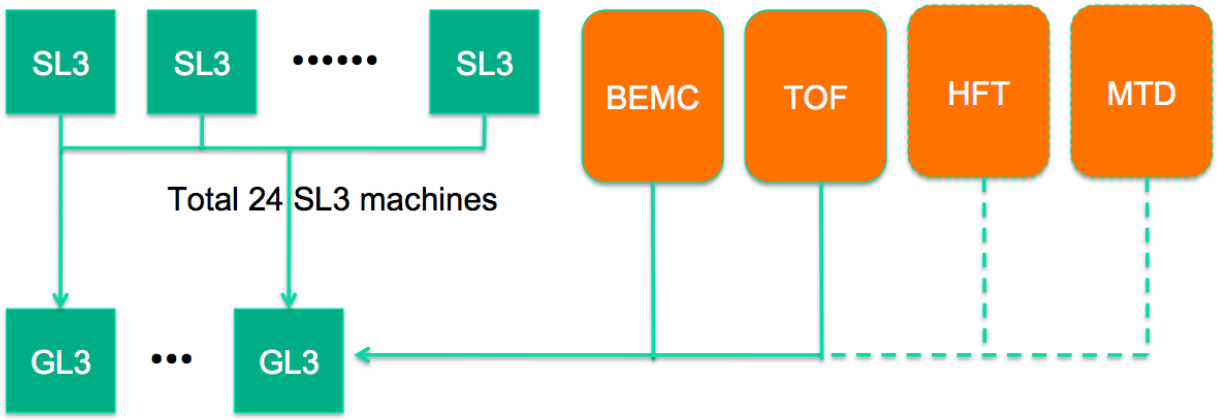

Figure 3-1: The HLT architecture in 2010 and 2011.

and no additional time is needed for I/O. The disadvantage is that there are 24 DAQ machines, each of them takes care of only one TPC sector, and there is no communication between DAQ machines. This means that there is an efficiency loss for tracks crossing sector boundaries. However, the magnitude of such efficiency loss is only at 2% level and is manageable. After SL3, the tracking information is sent to GL3 machines in which they are assembled together with information from other subsystems (EMC, TOF, etc.) to make real-time decision on event selection and express streaming and/or data compression. In the future, STAR HLT will include the information from the Heavy Flavor Tracker (HFT) and the Muon Telescope Detector (MDT) to trigger heavy flavor events and μ rich events.

3.2 Online Tracking

HLT online tracker is implemented at the point when all the data from the detectors are collected by the DAQ. The core algorithm of the tracker is the fast track finder based on conformal mapping, which transforms a given space point into conformal space point according to the equations: $x_i^{'} = x_i/R_i^2$, $y_i^{'} = -y_i/R_i^2$, where $R_i^2 = (x - x_0)^2 + (y - y_0)^2$. This transformation requires the knowledge of a point (x_0, y_0) on the track trajectory, which is either the beam interaction point for primary tracks or the first point associated with the

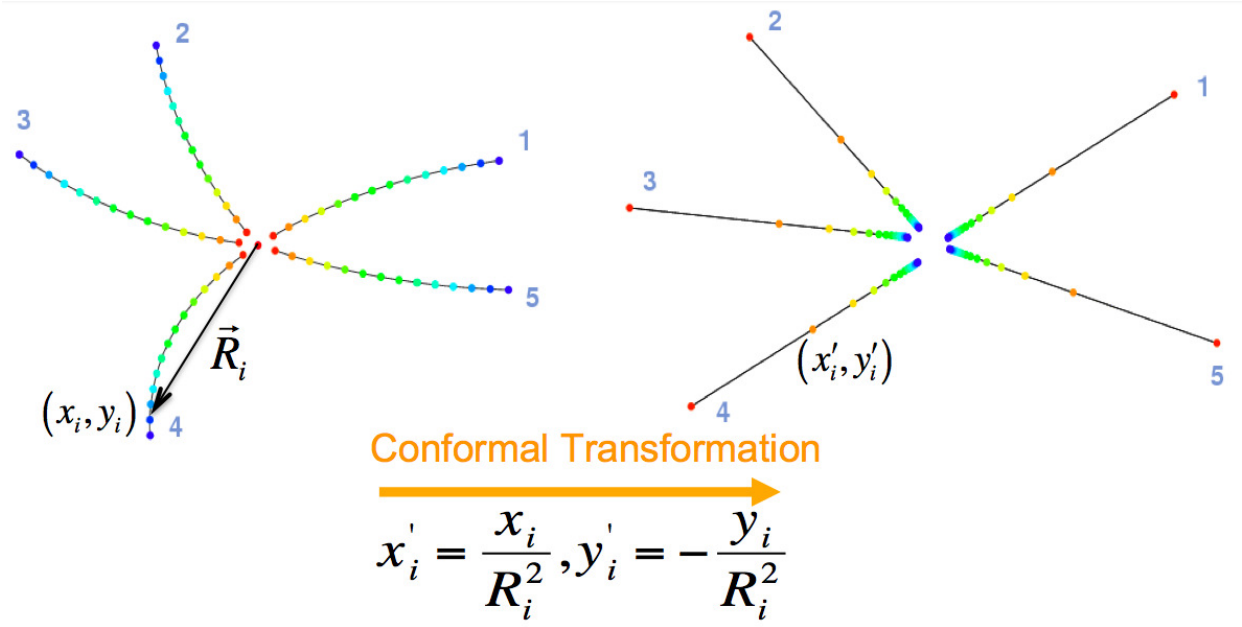

Figure 3-2: HLT online tracking algorithm.

track for secondary tracks. Once a track is found, it can be refitted with a helix model in real space. Figure 3-3 shows the HLT online tracking efficiency (left panel) and p_T resolution (right panel) with respect to the offline tracking algorithm, by assuming that the offline reconstruction efficiency is 100%. The relative HLT online tracking efficiency is larger than 90% with $p_T > 1$ GeV/c, while the relative p_T resolution is lower than 2% at $p_T < 3$ GeV/c.

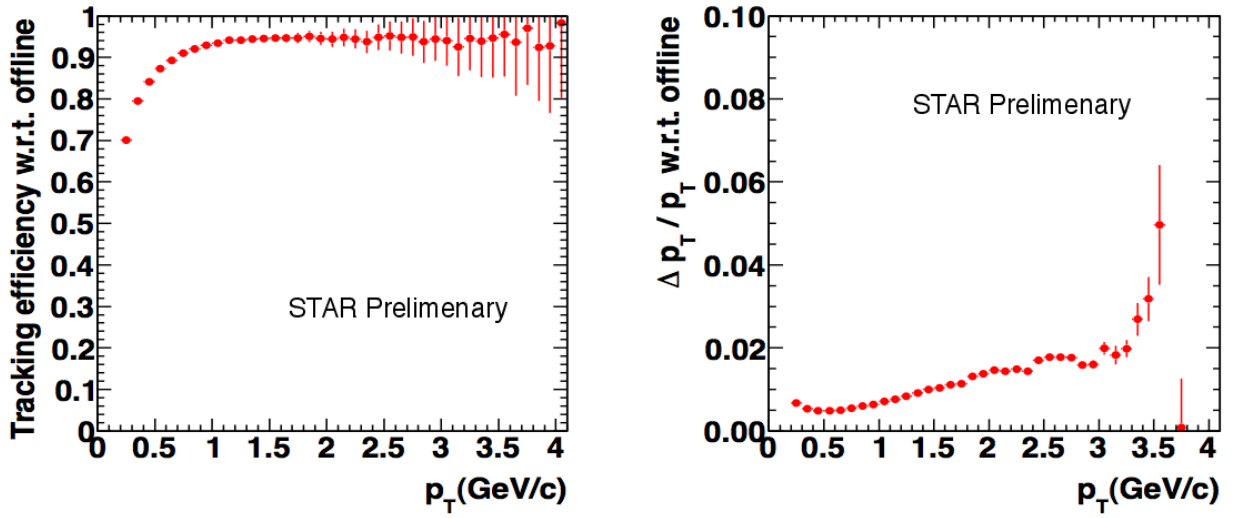

Figure 3-3: HLT online tracking efficiency (left) and p_T resolution (right) as a function of p_T in 200 GeV Au+Au collisions.

3.3 Online Monitoring

HLT online monitoring provides real-time feedback on the quality of the events triggered. In particular, monitoring the TPC tracking quality and the matching between TPC tracks and TOF or BEMC hits is essential for ensuring a properly working HLT. Figure 3-4 shows some selected online quality assurance plots in Au+Au 200 GeV events taken in 2010. Panel (a) presents the number of TPC clusters (nHits) in a track reconstructed online. Panel (b) shows the mean energy loss ($\langle dE/dx \rangle$) as a function of momentum. With it we monitor

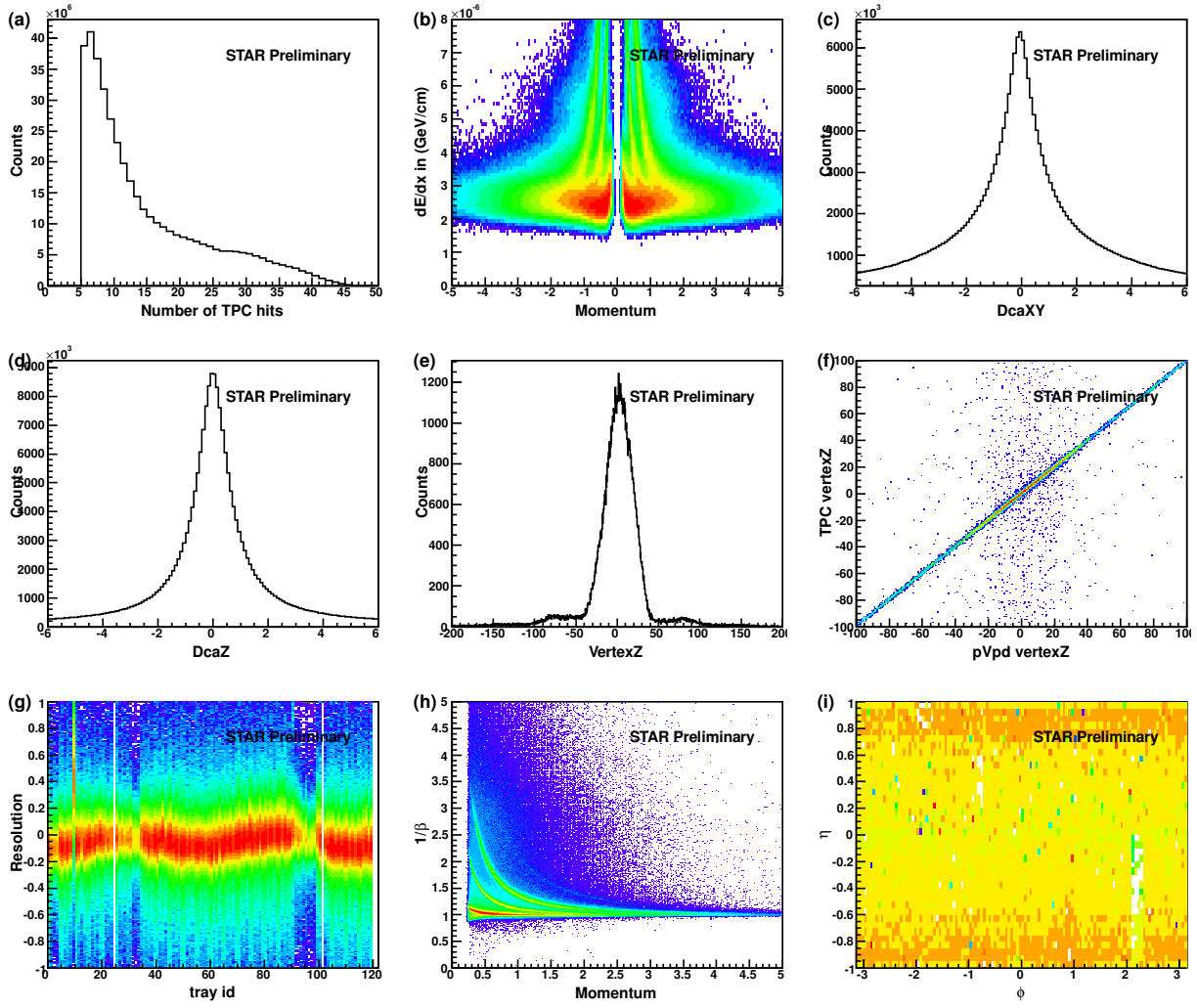

Figure 3-4: Selected HLT online quality assurance (QA) plots in 200 GeV Au+Au collisions.

the change of dE/dx online calibrations. Panel (c) and (d) are for the distance of closest

approach (DCA) between tracks and primary vertex, in the transverse plane (Dca_{XY}) and in the beam line direction (Dca_Z), respectively. The distortions of tracks in TPC due to the residual space charge effect and the non-perfect electric field will cause the shift of mean value on the dca distribution, and can be monitored by these two plots. Panel (e) is the reconstructed vertex Z distribution to monitor the vertex reconstruction at GL3 level. Panel (f) shows the correlation between vertex Z reconstructed by TPC and that calculated with the pseudo Vertex Position Detector (pVpd). Panel (g) and (h) present the tray by tray timing resolution of TOF and inverse velocity of tracks as a function of their momentum, respectively. Both are used for monitoring TOF calibrations. Panel (i) shows the η vs. ϕ distribution for BEMC signals. It can be used to identify running-away "hot towers".

3.4 Offline software development

Three software packages have been developed in order to propagate the HLT online information to offline. They are, StHltEvent, StMuHltEvent, and StHltMaker. StHltEvent is for transferring both TPC hits and tracks information to "event.root" format files which can be integrated with other offline softwares. StMuHltEvent is for further propagating TPC track information to "MuDst.root" format files for analysis. StHltMaker is the function which fill both StHltEvent and StMuHltEvent.

StHltEvent consists of modules of StHltEvent, StHltTrack, StHltBEmcTowerHit, StHltBTofHit, StHltVpdHit, StHltTrackNode, StHltTriggerReasonCapable, StHltTrigger-Reason, StHltHeavyFragment, StHltDiElectron, and StHltHighPt. StHltEvent also contains event level variables, such as trigger type, event vertex, and collision start-time. StHltTrack contains track level variables like charge, $\langle dE/dx \rangle$, momentum, etc. StHltBEmcTowerHit is for the energy deposition, and η and ϕ angle of BEMC hits. StHltBTofHit and StHltVpdHit

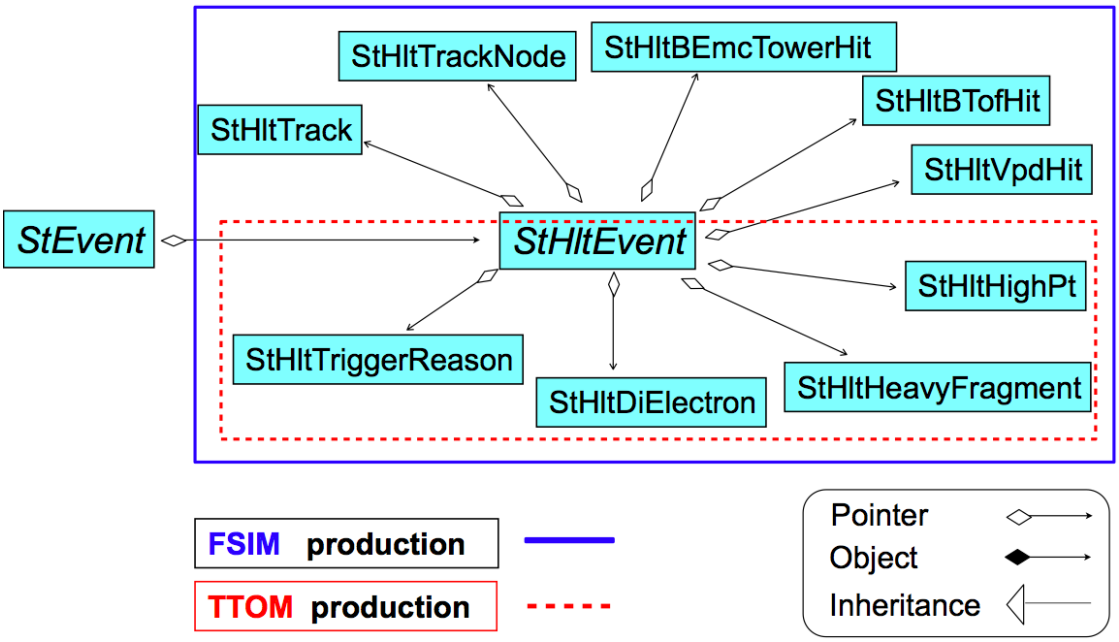

Figure 3-5: StHltEvent modules to propagate HLT online information to "event.root" format files.

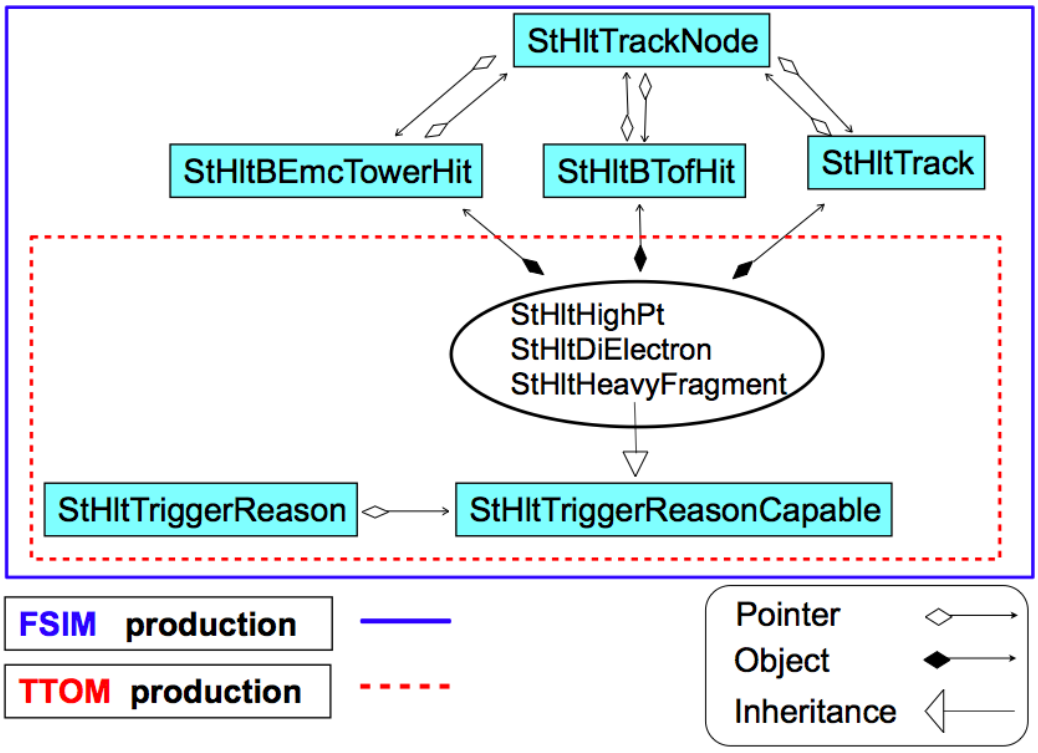

Figure 3-6: StHltEvent modules to propagate HLT online information to "event.root" format files.

are for storing the TOF and pVpd information, respectively. StHltTrackNode keeps the matching information between TPC tracks and TOF and BEMC hits. StHltHeavyFragment, StHltDiElectron, and StHltHighPt are for storing information of triggered light (anti)nuclei, di-electrons, and high-p_T tracks, respectively. Figures 3-5 and 3-6 present the connections between these modules.

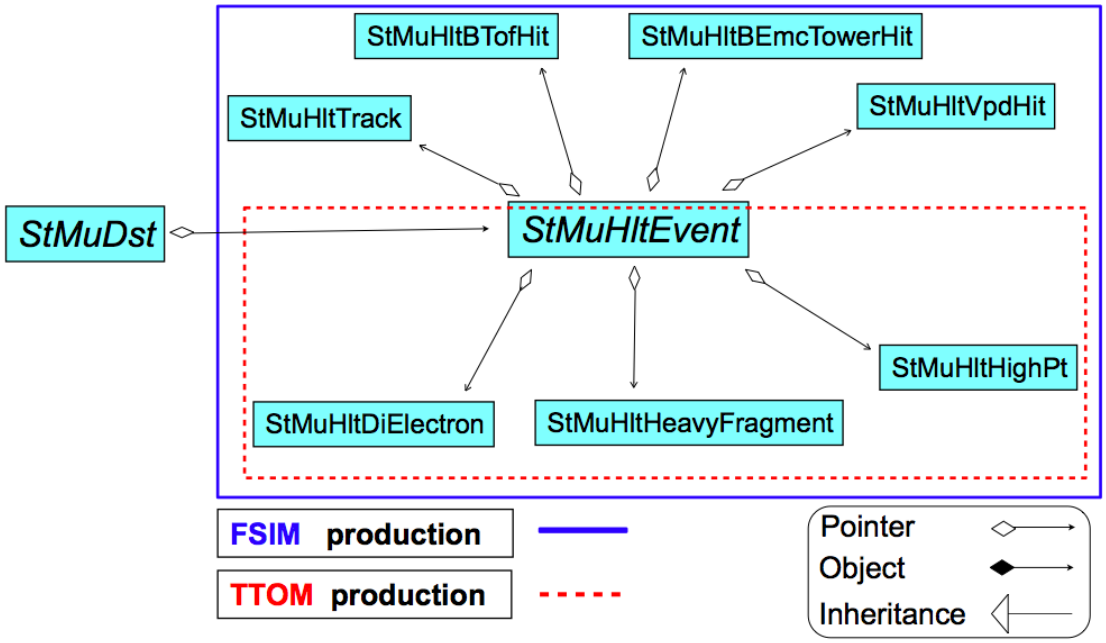

Figure 3-7: StMuHltEvent modules to propagate HLT online information to "Mudst.root" format files.

Like the StHltEvent, StMuHltEvent consists of modules of StMuHltEvent, StMuHltTrack, StMuHltBTofHit, StMuHltVpdHit, StMuHltBEmcTowerHit, StMuHltDiElectron, StMuHltHeavyFragment, and StMuHltHighPt. They are shown in Figures 3-7 and 3-8. Those classes are used in propagating HLT online information to "MuDst.root" files for physics analyses.

Figure 3-9 depicts the STAR offline data production flow with StHltMaker. STAR offline packages have a chain of "Makers", and each of them has a unique chain option to be enabled in the so called "big full chain" production. The corresponding chain option for StHltMaker

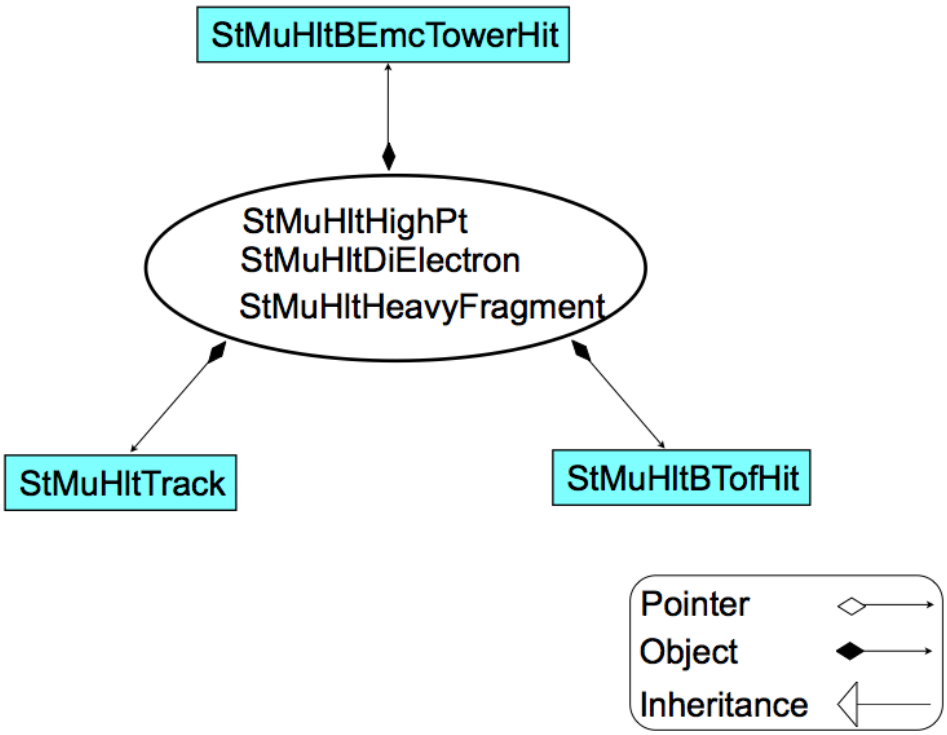

Figure 3-8: StMuHltEvent modules to propagate HLT online information to "Mudst.root" format files.

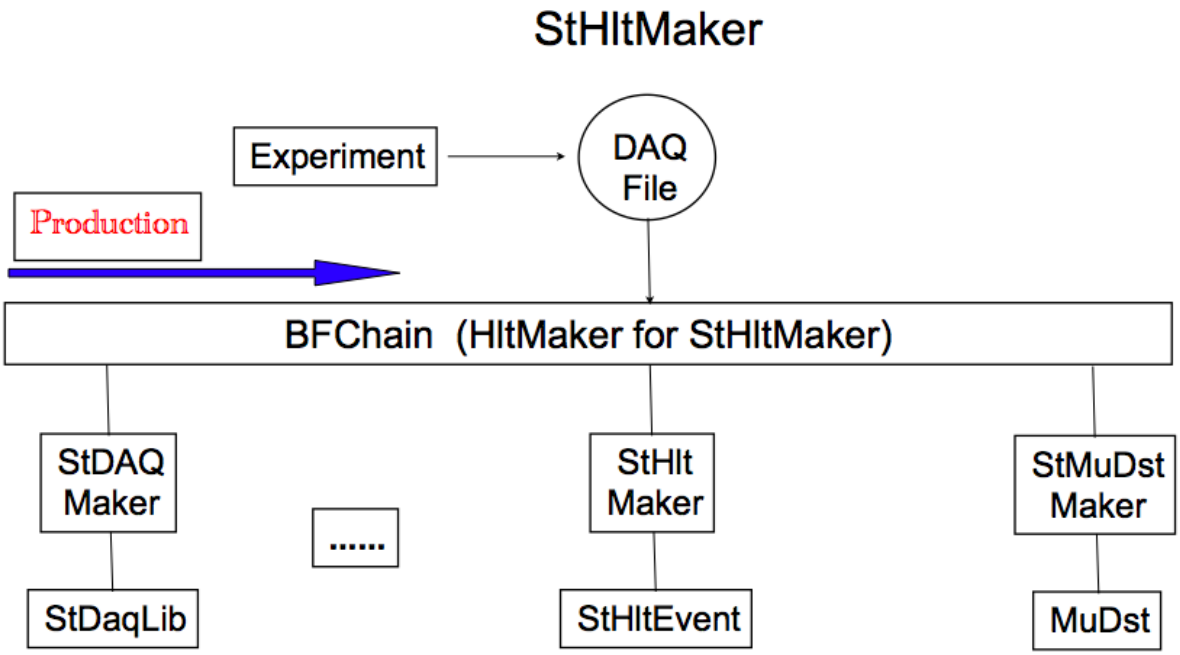

Figure 3-9: STAR offline data production flow.

is"HltMaker".

3.5 Online triggers for J/ψ and light (anti)nuclei

STAR HLT has successfully selected Au+Au collisions with J/ψ and light (anti)nuclei during 2010 and 2011 runs. To trigger J/ψ events, the HLT identified electrons and positrons based on their energy loss in TPC ($\langle dE/dx\rangle$, $n\sigma_e \in [-0.3, 3.0]$), velocity measured by TOF ($|1/\beta - 1| < 0.03$), and energy deposited in BEMC ($p/E \in [0.3, 1.5]$). J/ψ can be reconstructed and triggered online via its decay channel: $J/\psi \rightarrow e^+ + e^-$. To select events with light (anti)nuclei, a TPC $\langle dE/dx\rangle$ cut of $n\sigma_{He3} > -3$ was made online. Panels (a) and (b) of Figure 3-10 show the J/ψ invariant mass spectra and $\langle dE/dx\rangle$ as a function of momentum for light (anti)nuclei reconstructed by HLT online, respectively.

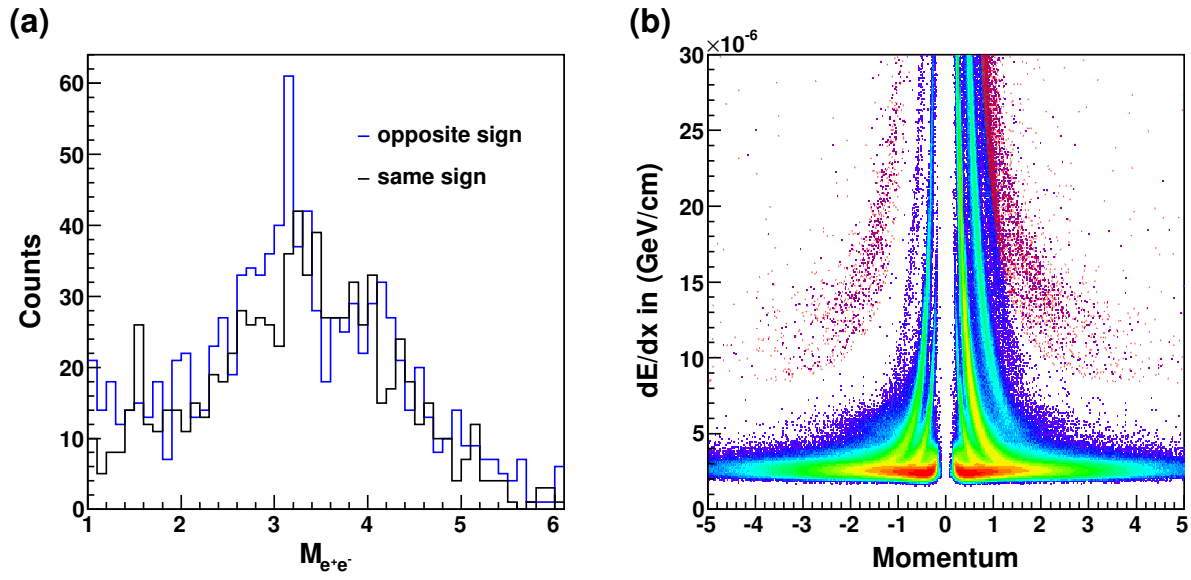

Figure 3-10: (a) J/ψ invariant mass spectra reconstructed via $J/\psi \rightarrow e^+ + e^-$ by HLT online. The blue line and the black line indicate the J/ψ signal and the background, respectively. (b) $\langle dE/dx\rangle$ as a function of momentum. The red triangles stand for the light (anti)nuclei triggered by HLT online based on a cut of $n\sigma_{He3} > -3$.

The light (anti)nuclei enhanced dataset, selected by the HLT in 2010, has been analyzed and 16 $^4\overline{\mathrm{He}}$ candidates have been observed, together with 2 additional $^4\overline{\mathrm{He}}$ candidates ob-

served in the year 2007[48], STAR has identified 18 $^{4}\overline{\mathrm{He}}$ nuclei in total. The result was published in Nature in April 2011, and will be discussed in the next chapter.

Chapter 4 Observation of the $^{4}\overline{\mathrm{He}}$ ($\overline{\alpha}$) nucleus

The idea of antimatter can be traced back to the end of 1890s, when Schuster hypothesized the existence of antiatoms as well as antimatter solar system in his letter to Nature magazine[49]. The modern concept of antimatter is originated from the negative energy state solution of a quantum mechanical equation, proposed by Dirac in 1928[50]. The first antimatter particle, the positron, was observed four years later in the cosmic radiation[51]. The possibility of the anti-gravity behavior between matter and antimatter has been discussed in 1961[52]. Since the observation of antiproton ($\overline{\mathrm{p}}$)[53] in 1955, antimatter nucleus such as $\overline{\mathrm{d}}$, $^{3}\overline{\mathrm{H}}$, $^{3}\overline{\mathrm{He}}$ has been discovered and widely studied in both cosmic rays[1–3, 54, 55] and high energy heavy ion collisions[48, 56]. More recently, the ALPHA experiment at CERN has successfully trapped hydrogen atoms for 1000 seconds[57, 58]. In 2011, the STAR experiment at RHIC observed the $^{4}\overline{\mathrm{He}}$ nucleus, also known as the $\overline{\alpha}$ particle[9, 10]. The production of light antinuclei in heavy ion collisions can be modeled successfully by macroscopic thermodynamics, which assumes energy equipartition, or by a microscopic coalescence process, which assumes uncorrelated probabilities for antinucleons close in position and momentum to become bound. Based on this study, the production rate for $^{4}\overline{\mathrm{He}}$ to

be produced by coalescence of products from collisions between energy cosmic rays and interstellar materials is too low to be observed. Thus even a single $^4\overline{\mathrm{He}}$ nucleus observed in the cosmic radiation should be a great hint of the existence of massive antimatter in the Universe.

In this chapter, we present the measurement of $^4\overline{\mathrm{He}}$ nucleus made by the STAR experiment. Unless annihilation, $^4\overline{\mathrm{He}}$ nuclei can travel through the STAR TPC and reach the TOF without decay, therefore, they can be identified by correlating their energy loss ($\langle dE/dx \rangle$) and measured magnetic rigidity (p/Z), as well as the measurement of their mass value. This chapter is arranged as follows: the dataset and cuts used in the analysis are presented in section 1. Section 2 focuses on the identification of of $^4\overline{\mathrm{He}}$ nucleus. In section 3, the event displays for $^4\overline{\mathrm{He}}$ candidates are presented. In section 4, the ^{4}He and $^4\overline{\mathrm{He}}$ invariant yield measurements are presented. In section 5, the background estimation, absorption correction, knock-out from beam pipe interaction are discussed. Section 6 summarizes the systematic errors.

4.1 Data sample and cuts

With upgraded readout electronics for TPC and fully installed TOF, STAR had already recorded enormous Au+Au collisions at 200 GeV, 62 GeV, 39 GeV, 11.5 GeV, and 7.7 GeV during the 2010 RHIC runs. Preferential selection of events containing tracks with charge $Ze = \pm 2e$ in 200 GeV and 62 GeV was implemented using HLT, and the selected dataset was analyzed for the measurements of the $^4\overline{\mathrm{He}}$ nucleus.

Collisions used for this analysis are required to have primary vertex position within 30 cm from the center of the TPC along the beam line direction, and have a less than 3 cm difference between the z vertex reconstructed by a vertex position detector (VPD) and the

TPC. Extra selection criteria for tracks, as shown in table 4-1, are used to obtain a clean separation between ^{3}He ($^3\overline{\text{He}}$) and ^{4}He ($^4\overline{\text{He}}$), and a significant signal to background ratio (S/B) for $^4\overline{\text{He}}$. In the table, nHits and nHitsdEdx are the total number of hits reconstructed by TPC and number of hits used for $\langle dE/dx\rangle$ calculation, respectively. nHitsPoss and nHitsFit are the total number of possible hits reconstructed and number of hits used for fitting, respectively. Cuts of nHits > 25, nHitsdEdx > 15 and nHitsFit/nHitsPoss > 0.52 are used to reject "short tracks" and "splitting tracks". Pseudo-rapidity $|\eta| < 1.0$ is required to assure that the track is fully in TPC acceptance. Secondary particles and background from the beam-pipe interactions are removed by applying the *Dca* (distance of closest approach) cuts. The track quality cut, $\chi^2 < 2.0$, is used to assure that the selected tracks have the best fitting. A new variable, $n\sigma^{^4He}_{dE/dx}$, defined as $\frac{1}{R}\ln(\langle dE/dx\rangle_{^4He}/\langle dE/dx\rangle^B_{^4He})$, is used for the identification of the $^4\overline{\text{He}}$ nucleus. Here, $\langle dE/dx\rangle^B_{^4He}$ is the expected $\langle dE/dx\rangle$[39] for ^{4}He and $^4\overline{\text{He}}$ nucleus, R is the $\langle dE/dx\rangle$ resolution. Y_{Local} and Z_{Local} specify the TOF pad position where a TOF electronic signal fired by a TPC track. $|\text{Y}_{\text{Local}}| < 1.5$ cm and $|\text{Z}_{\text{Local}}| < 2.9$ cm are required to exclude those hits located at the edge of the TOF pads.

	dE/dx PID method	TOF PID method	Invariant Yield measurement
primary track	Yes	Yes	Yes
nHits	> 25	> 25	> 25
nHitsdEdx	> 15	> 15	> 15
nHitsFit/nHitsPoss	$\in (0.52, 1.05)$	$\in (0.52, 1.05)$	$\in (0.52, 1.05)$
η	$\in (-1.0, 1.0)$	$\in (-1.0, 1.0)$	$\in (-1.0, 1.0)$
$q * Dca$	< 0.5 cm	< 0.5 cm	< 0.5 cm
$p/\lvert Z\rvert$	> 0.2 GeV/c	$\in (1.0, 5.0)$ GeV/c	> 0.2 GeV/c
$p_T/\lvert Z\rvert$	> 0.2 GeV/c	> 0.2 GeV/c	> 0.2 GeV/c
χ^2	< 2.0	< 2.0	< 2.0
$n\sigma^{^4He}_{dE/dx}$	-	-	$\in (-2.0, 3.0)$
Y_{Local}	-	$\in (-1.5, 1.5)$ cm	$\in (-1.5, 1.5)$ cm
Z_{Local}	-	$\in (-2.9, 2.9)$ cm	$\in (-2.9, 2.9)$ cm

Table 4-1: Cuts used for the $^4\overline{\text{He}}$ nucleus measurements.

4.2 $^4\overline{\mathrm{He}}$ identification

The identification of the $^4\overline{\mathrm{He}}$ nucleus relies on two key measurements: the mean energy loss $\langle dE/dx \rangle$ inside TPC, and the time of flight of particles arriving at the TOF detector. In general, TOF provides particle identification in a higher momentum range than $\langle dE/dx \rangle$, with a timing resolution of 95 ps within a window of 7 to 75 ns.

4.2.1 $n\sigma_{dE/dx}$ correction for light (anti)nuclei

The $n\sigma_{dE/dx}$ defined above denotes the deviation of the measured $\langle dE/dx \rangle$ from the theoretical expectation[39]. Figure 4-1 shows the $n\sigma^{^3He}_{dE/dx}$ distribution in 200 GeV Au+Au collisions selected by the HLT. It has a shape of multiple-gaussian, and from it the ^{3}He ($^3\overline{\mathrm{He}}$) can be well separated from the other particles. Therefore, by applying a $n\sigma^{^3He}_{dE/dx}$ cut,

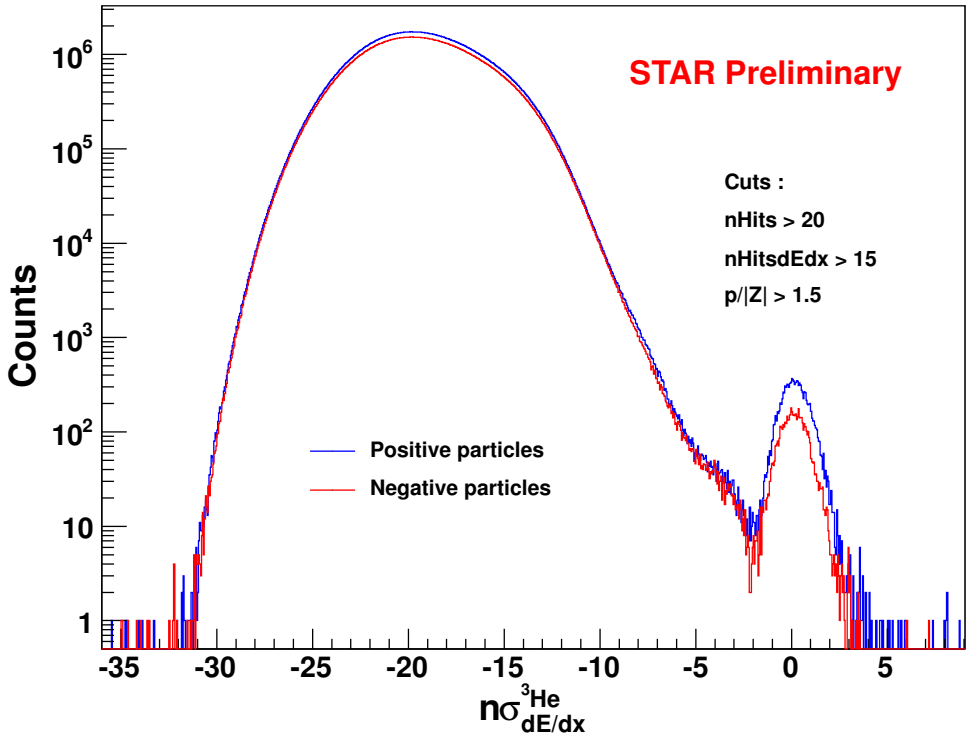

Figure 4-1: $n\sigma^{^3He}_{dE/dx}$ distribution in 200 GeV Au+Au collisions. The blue (red) lines denote the positive (negative) particles, respectively.

^{3}He and $^3\overline{\text{He}}$ can be sampled successfully with a high purity. By definition, the distribution of $n\sigma_{dE/dx}$ has a variance with a value fixed at unity. Unfortunately, the dE/dx calibration parameters based on a pure π (Ze=$\pm$1e) sample, which have small $\langle dE/dx \rangle$, is not applicable for light (anti)nuclei (Ze=$\pm$2e) with large $\langle dE/dx \rangle$ value. This makes the variance of $n\sigma_{dE/dx}$ deviating from the unity. When this happens, extra corrections of the $n\sigma_{dE/dx}$ for light (anti)nuclei needs to be made.

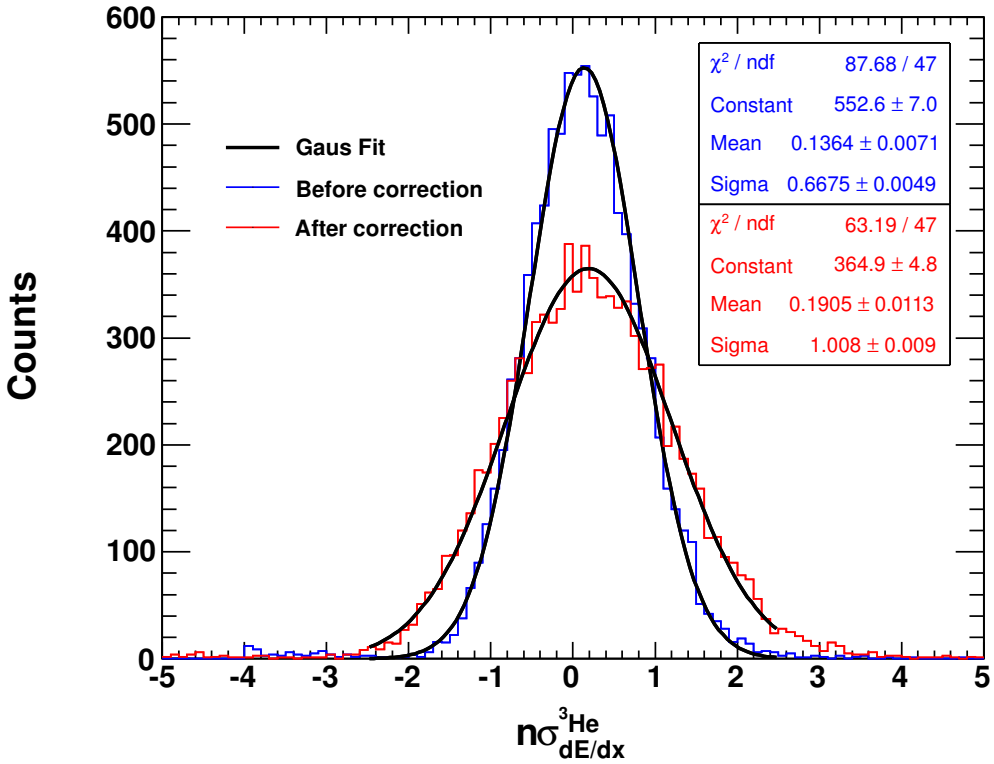

Figure 4-2: $n\sigma^{^3He}_{dE/dx}$ distribution for a pure ^{3}He and $^3\overline{\text{He}}$ sample selected based on TOF cuts in 200 GeV Au+Au collisions. Blue (red) line indicate the $n\sigma^{^3He}_{dE/dx}$ before (after) correction.

The $n\sigma_{dE/dx}$ for light (anti)nuclei can be corrected by dividing the σ from fitting the original $n\sigma^{^3He}_{dE/dx}$ distribution with a pure ^{3}He ($^3\overline{\text{He}}$) sample based on the TOF mass cut. Figure 4-2 presents the $n\sigma^{^3He}_{dE/dx}$ distribution in 200 GeV Au+Au collisions. It shows that, the σ value for ^{3}He and $^3\overline{\text{He}}$ moves to 1.0 after the $n\sigma_{dE/dx}$ correction.

4.2.2 $^4\overline{\text{He}}$ identification with $\langle dE/dx \rangle$

Figure 4-3 shows $\langle dE/dx \rangle$ versus the measured magnetic rigidity ($p/|Z|$) distribution, based on a combined dataset of 200 GeV and 62 GeV Au+Au collisions. The colored dots are the light (anti)nuclei selected by the HLT, while the grey bands are π, K, proton, and their antimatter partners from 200 GeV MiniBias data, plotted as a reference. A distinct band centered around the expected value[39] for ^{4}He particles is shown in the right panel, which indicates that the detector is well-calibrated. In the left panel, where $p/|Z|$ is less than 1.4 GeV/c, 4 $^4\overline{\text{He}}$ particles are located within the expected band for $^4\overline{\text{He}}$ and well separated from the $^3\overline{\text{He}}$ band. Two of them at the lower momentum region are from collisions recorded by TPC during 2007[48]. Above 1.75 GeV/c, $\langle dE/dx \rangle$ values of $^3\overline{\text{He}}$ and $^4\overline{\text{He}}$ merge together and the TOF system is needed to separate these two species.

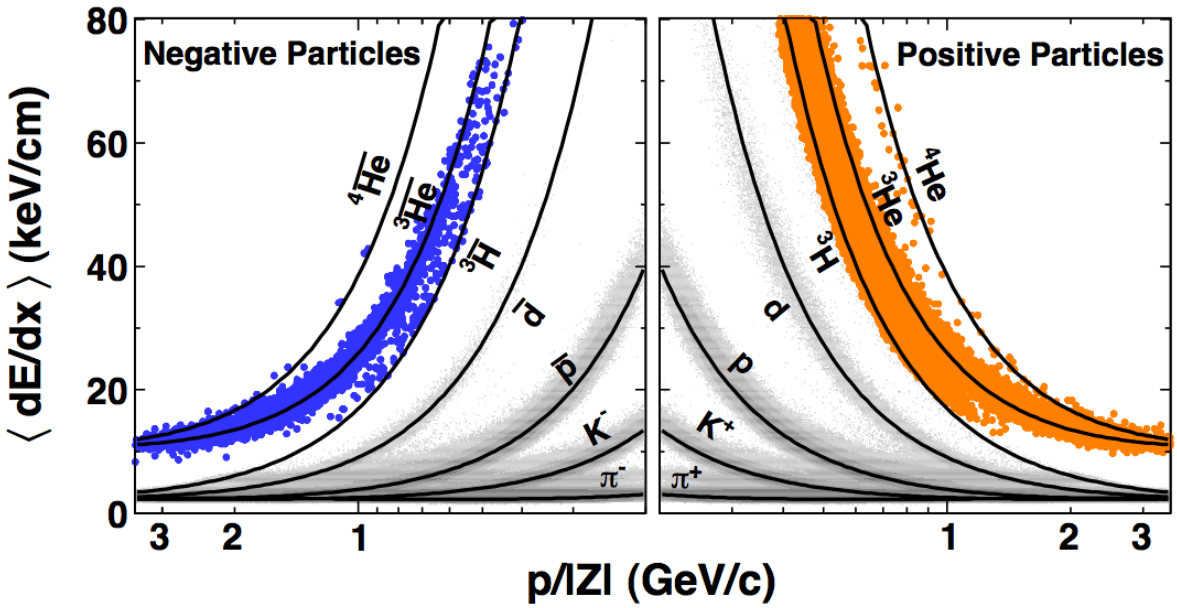

Figure 4-3: $\langle dE/dx \rangle$ versus $p/|Z|$ for negatively charged particles (left) and positively charged particles (right). The black curves show the expected values for each species. The lower edges of the colored bands correspond to the HLT's online calculation of 3σ below the $\langle dE/dx \rangle$ band center for ^{3}He. For reference, the grey bands indicate the d, $\overline{\text{d}}$, p, $\overline{\text{p}}$, K and π from Au+Au Minimum bias events at 200 GeV.

4.2.3 TOT slewing recalibration for (anti)nuclei

The pVpd and TOF are used to measure the collision starting time (T_{start}) and particle arriving time at TOF (T_{stop}), and therefore, calculate the time of flight (t) for particles. With the momentum (p) and the particle track length (L) derived from the track curvature in the TPC, the mass square of a particle can be calculated as, $m^2 = p^2 \times (t^2/L^2 - 1)$. Figure 4-4 shows the $1/\beta$ and the mass square (inserted) as a function of rigidity for π, K, and proton in Au+Au 200 GeV. A separation of π and K up to1.6 GeV/c, K and proton up to 3.0 GeV/c can be achieved.

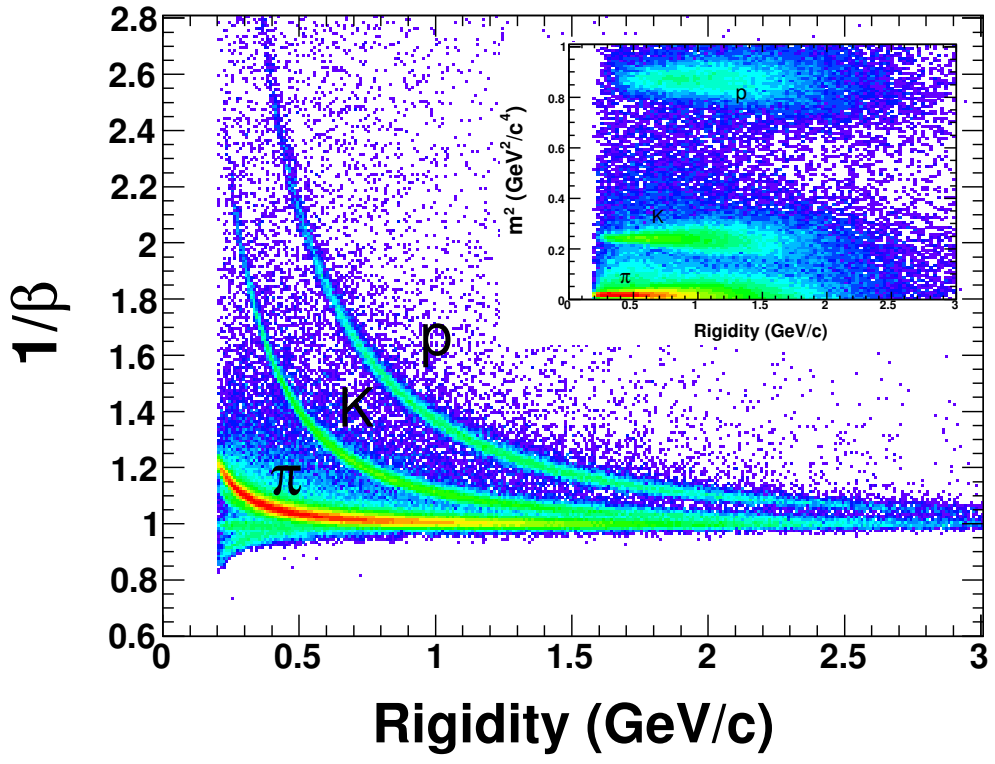

Figure 4-4: $1/\beta$ and mass square (inserted) as a function of magnetic rigidity ($p/|Z|$) for π, K and proton in 200 GeV Au+Au collisions.

To identify the $^4\overline{\mathrm{He}}$ nucleus based on the TOF detector, a series of calibrations are needed.

That includes the T_0 correction, the TOT (time over threshold) slewing correction, and the hit position correction for pVpd and TOF[59]. Calibrations are for reducing/eliminating the dependences of the difference between measured flight time and the expected value

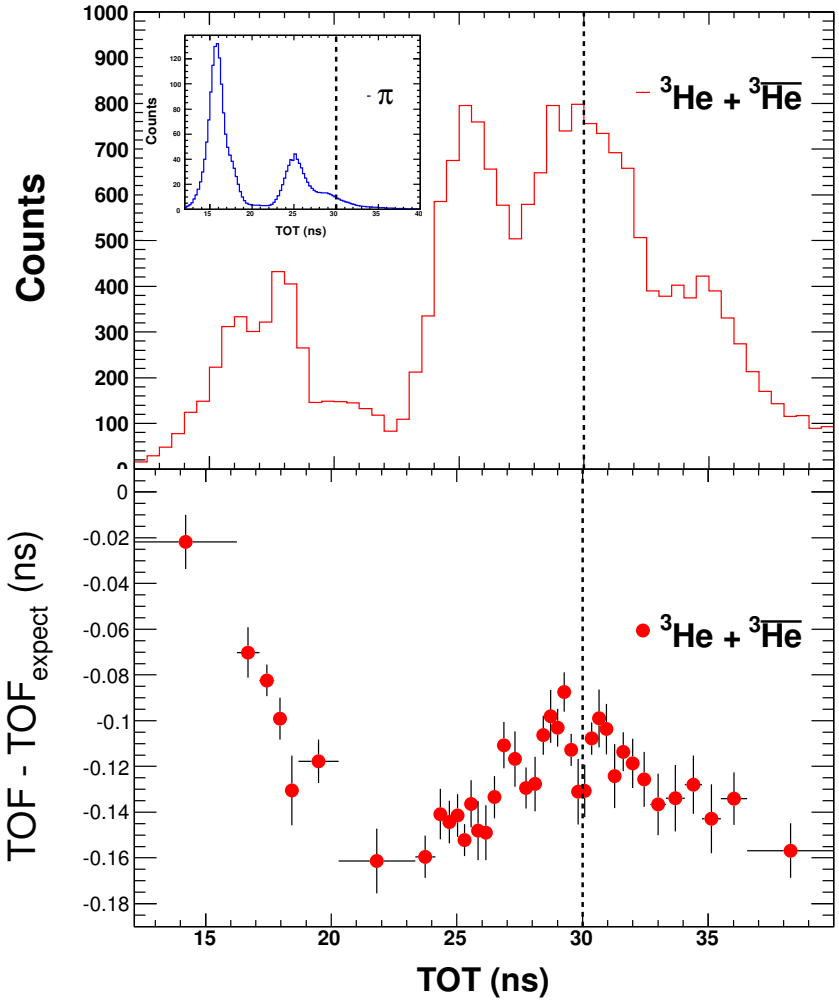

Figure 4-5: Top panel, the TOT distribution for ^{3}He and $^3\overline{\text{He}}$, and π (inserted). Bottom panel, the correlation between $tof - tof_{expect}$ and TOT for ^{3}He ($^3\overline{\text{He}}$).

($tof - tof_{expect}$), for T_0, TOT, and hit positions on TOF pads. Light (anti)nucleus tend to create a relative larger electronic signal, therefore, a larger TOT value than that of π. The pVpd and TOF calibration parameters based on a pure π sample, is not applicable for $^4\overline{\text{He}}$ identification. In Figure 4-5, the top panel presents the TOT distribution for

^{3}He and $^3\overline{\text{He}}$ and π (inserted), respectively. The bottom panel shows the correlation between $tof - tof_{expect}$ and TOT for ^{3}He and $^3\overline{\text{He}}$. The measured time of flight of ^{3}He and $^3\overline{\text{He}}$ nucleus shifted $\sim$ 140 ns with respect to their expected values. The STAR standard TOT slewing

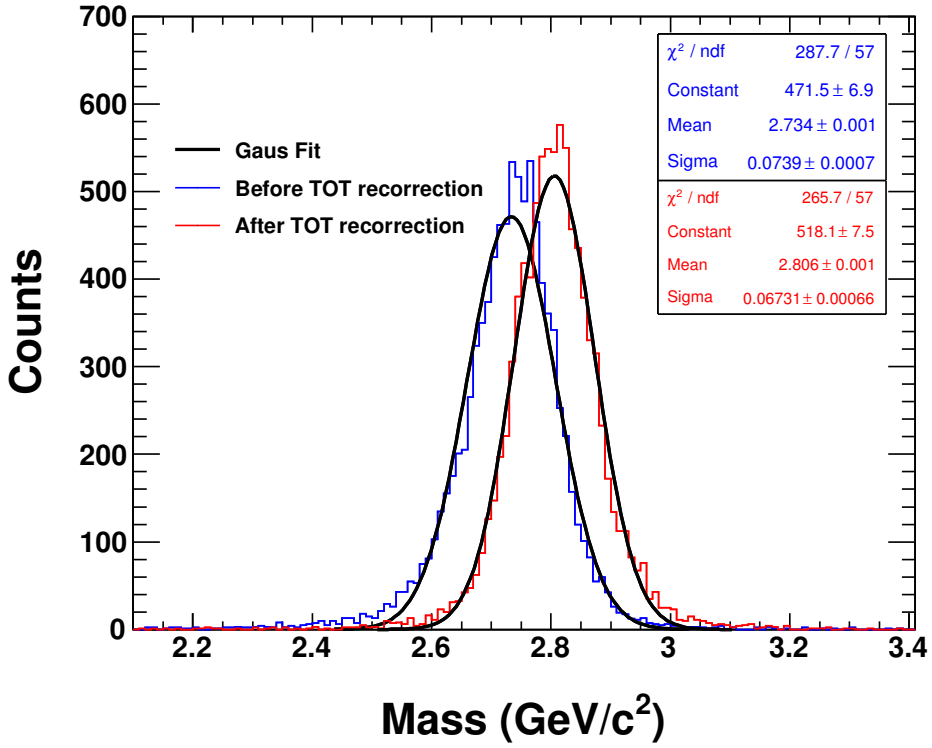

Figure 4-6: The measured mass for ^{3}He and $^3\overline{\text{He}}$ before (blue line) and after (red) the TOT slewing recorrection.

calibration procedure was followed for the correction, based on the sample of ^{3}He and $^3\overline{\text{He}}$. Figure 4-6 shows the calculated mass distribution for ^{3}He and $^3\overline{\text{He}}$ before and after applying the TOT correction. The measured mass value shifts from 2.734 GeV/c^2 to 2.806 GeV/c^2, after the TOT slewing correction.

4.2.4 $^4\overline{\text{He}}$ identification with dE/dx and TOF

A combination of $\langle dE/dx \rangle$ and mass measurement from TOF is used for the identification of $^4\overline{\text{He}}$ nucleus in high momentum range. Figure 4-7 shows the $n\sigma^{^4He}_{dE/dx}$ versus mass

distribution in Au+Au collisions at 200 GeV and 62 GeV. In both panels, the majority species are $^3\overline{\text{He}}$ and ^{3}He. A handful of $^4\overline{\text{He}}$ and ^{4}He nucleus around $n\sigma^{^4He}_{dE/dx} = 0$ and m^2/Z^2 = 3.47 GeV$^2/c^4$ are observed. The other particles in these two panels are ^{3}H and $^3\overline{\text{H}}$, respectively. The vertical lines indicate the theoretical mass value of $^3\overline{\text{He}}$ and $^4\overline{\text{He}}$, while the

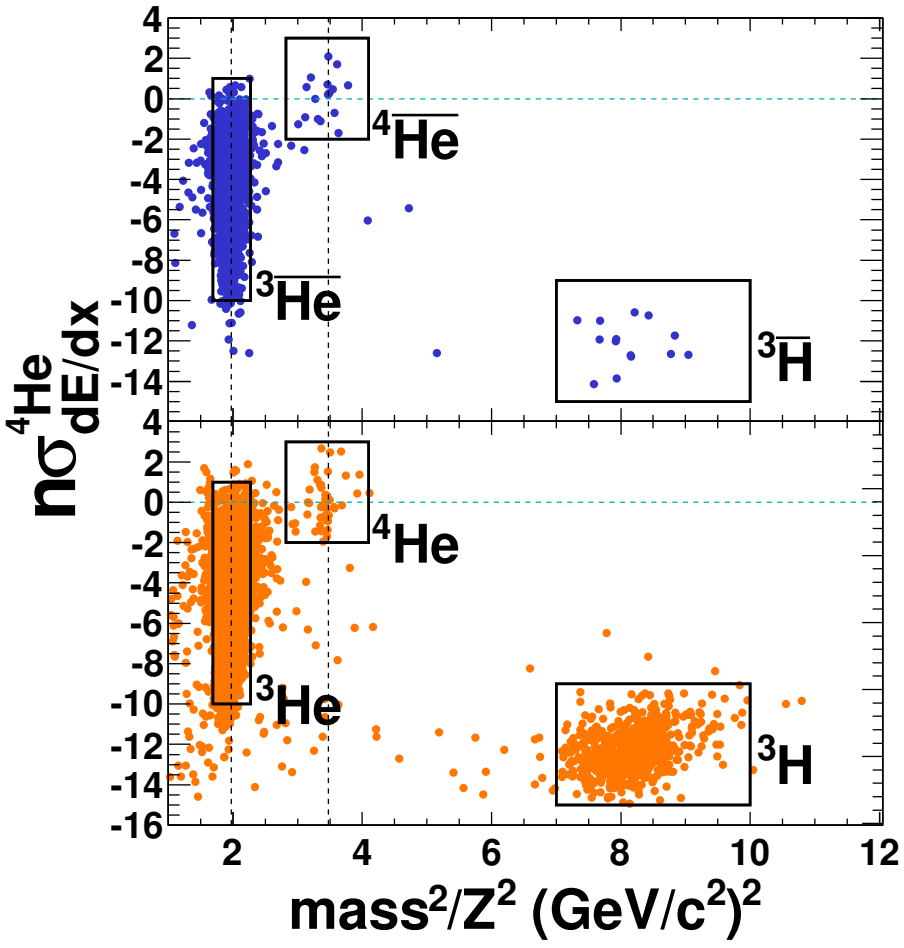

Figure 4-7: $n_{\sigma_{dE/dx}}$ vs m^2/Z^2 distribution of negatively charged particles (top panel) and positively charged particles (bottom panel). The theoretical values of m^2/Z^2 for ^{3}He ($^3\overline{\text{He}}$) and ^{4}He ($^4\overline{\text{He}}$) are indicated by the vertical lines at 1.97 GeV$^2/c^4$ and 3.47 GeV$^2/c^4$, respectively. The horizontal lines marks the position of $n_{\sigma_{dE/dx}} = 0$ for ^{4}He ($^4\overline{\text{He}}$).

horizontal line marks the position of $n\sigma^{^4He}_{dE/dx} = 0$ for ^{4}He and $^4\overline{\text{He}}$. The rectangles stand for the cuts used for the particle identification, for ^{4}He and $^4\overline{\text{He}}$, they are $-2.0 < n\sigma^{^4He}_{dE/dx} < 3.0$ and 3.35 GeV/c^2 < mass < 4.04 GeV/c^2, the second one corresponds a cut of 3σ. Figure

4-8 shows the projection onto the mass axis for particles within a cut: $-2.0 < n\sigma^{^4He}_{dE/dx} < 3.0$ in Figure 4-7. There is clear separation between $^3\overline{\mathrm{He}}$ and $^4\overline{\mathrm{He}}$ mass peaks. During 2010 runs, the STAR experiment has observed 16 $^4\overline{\mathrm{He}}$ nucleus in total based on the HLT-selected data sample.

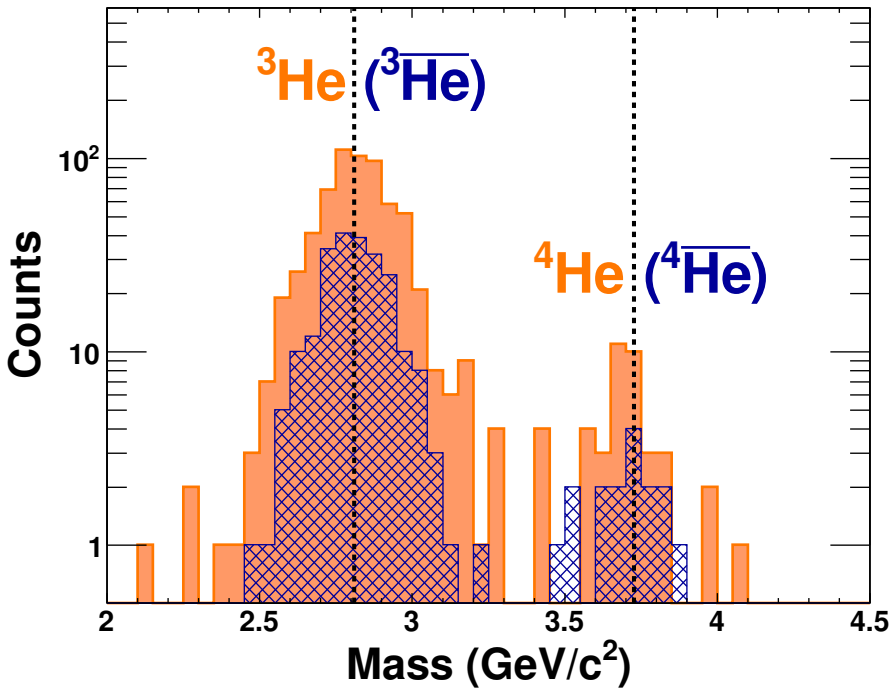

Figure 4-8: Mass distribution for ^{3}He ($^3\overline{\mathrm{He}}$) and ^{4}He ($^4\overline{\mathrm{He}}$) in 200 GeV and 62 GeV Au+Au collisions.

4.3 $^4\overline{\mathrm{He}}$ event display

STAR standard event display has been used to visually check all $^4\overline{\mathrm{He}}$ candidates. Figure 4-9 is the three-dimensional rendering of the STAR TPC surrounded by the TOF shown as the outermost cylinder. $^4\overline{\mathrm{He}}$ candidate is highlighted in red, and other tracks in the event are shown in golden. In addition, hit level event display is used to check the track quality, such as "short tracks" and "splitting tracks", of $^4\overline{\mathrm{He}}$ candidates. Figures 4-10 and 4-11 present the hit level event displays for $^4\overline{\mathrm{He}}$ candidates with run numbers of 11042004 and 11051001, respectively. The blue lines are the drawing of a thin conductive central

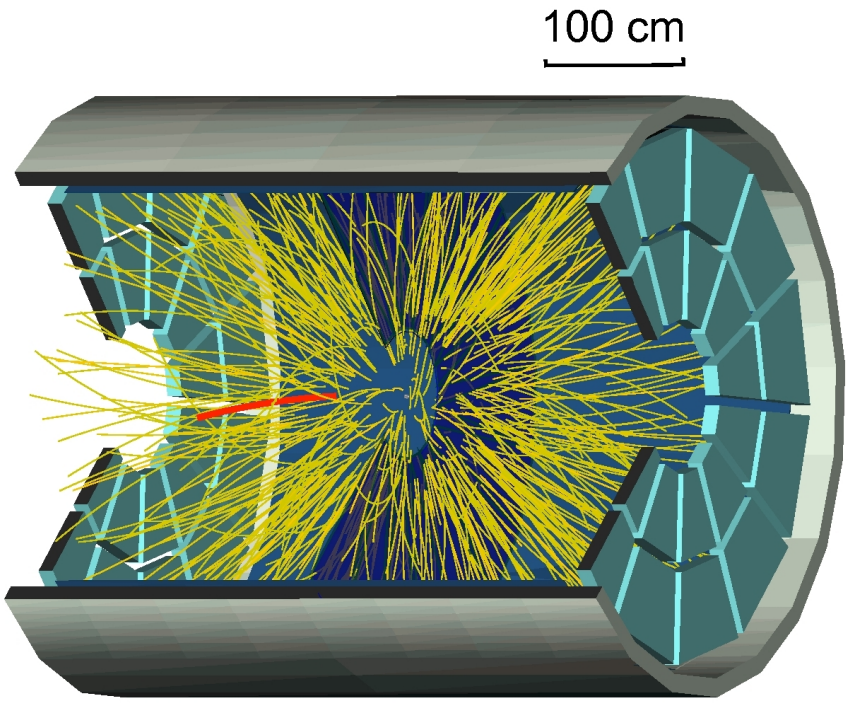

Figure 4-9: A three-dimensional rendering of the STAR TPC surrounded by the TOF shown as the outermost cylinder. Tracks from an event which contains a $^4\overline{\text{He}}$ are shown, with the $^4\overline{\text{He}}$ track highlighted in bold red.

membrane (CM) at the center of the TPC. The cylinder along the beam direction consists of the TPC inner field cage, and the end-caps at the bottom contain 24 TPC sectors, with 12 sectors on each side. The red solid rectangles highlight the $^4\overline{\text{He}}$ candidate in the event, and the blue circles are the hits that are never used for tracking by TPC. To avoid the "splitting tracks" of $^4\overline{\text{He}}$ candidates, any other tracks which have at least one hit within 5 cm of the $^4\overline{\text{He}}$ candidate are shown in different colors. The event display and properties for the other $^4\overline{\text{He}}$ candidates can be found in Appendix A and B.

RunID	**EvtID**	**Vz**	**RefMult**	**nHit**	**ndEdx**	$p/\|Z\|$	η	ϕ	**dca**
11042004	32163	-3.15	204	44	22	1.89	-0.16	2.33	0.35
length	χ^2	**n**$\sigma_{^4He}$	**E**	**tofZ**	**tofY**	**tot**	**tof**	β	**m**
193.83	0.69	-1.03	6.63	0.39	-0.15	20.30	9.95	0.72	3.66

Table 4-2: Properties for a $^4\overline{\text{He}}$ candidate with run number 11042004.

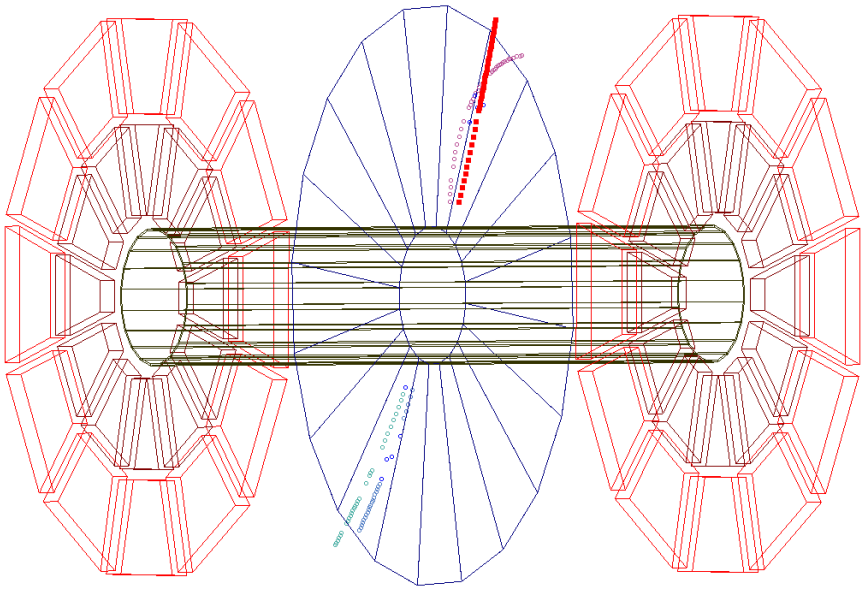

Figure 4-10: TPC event display for $^{4}\overline{\mathrm{He}}$ with run number 11042004. The red solid rectangles highlight the $^{4}\overline{\mathrm{He}}$ candidate. Tracks in other colors have at least one hit within 5 cm of the $^{4}\overline{\mathrm{He}}$ candidate.

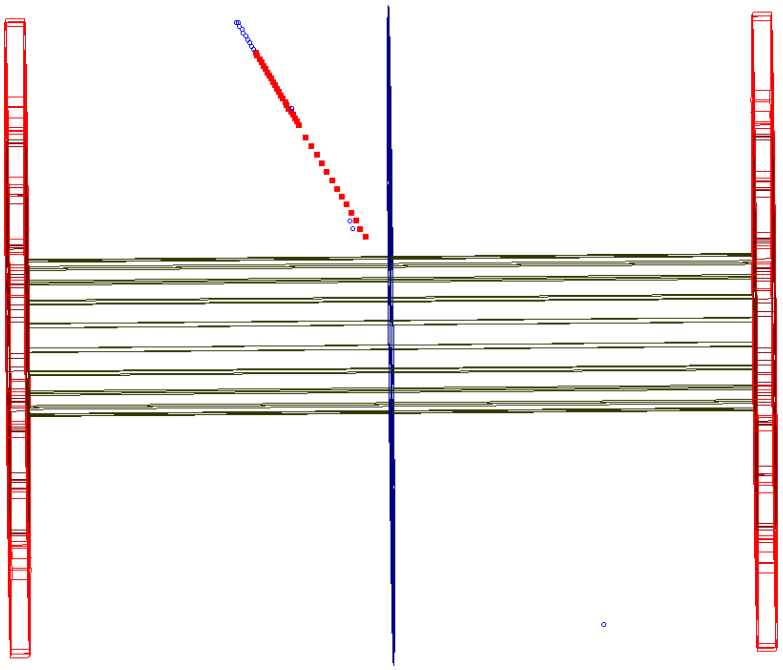

Figure 4-11: TPC event display for $^{4}\overline{\mathrm{He}}$ with run number11051001. The red solid rectangles highlight the $^{4}\overline{\mathrm{He}}$ candidate.

4.4 $^{4}\overline{\mathrm{He}}$ invariant yields

The differential invariant yield is calculated in Au+Au 200 GeV central collisions, using the observed $^{4}\overline{\mathrm{He}}$ counts. Various uncertainties related to TPC tracking, TOF matching,

RunID	**EvtID**	**Vz**	**RefMult**	**nHit**	**ndEdx**	$p/\|Z\|$	η	ϕ	**dca**
11051001	331536	-19.09	204	36	22	1.10	0.55	1.14	0.10
length	χ^2	$\mathbf{n\sigma_{^4He}}$	**E**	**tofZ**	**tofY**	**tot**	**tof**	β	**m**
197.30	0.81	0.23	1.90	-2.82	1.22	30.06	16.16	0.51	3.73

Table 4-3: Properties for a $^4\overline{\text{He}}$ candidate with run number 11051001.

and HLT trigger efficiency can be cancelled when calculating ^{4}He/^{3}He and $^4\overline{\text{He}}/^3\overline{\text{He}}$ ratios in a pseudo-rapidity window of $[-1.0, 1.0]$, and p_T window of $[0.75|\text{B}|, |\text{B}|]$ GeV/c (B is the baryon number). The ratios are $^4\text{He}/^3\text{He} = (3.0 \pm 1.3(\text{stat})^{+0.5}_{-0.3}(\text{sys})) \times 10^{-3}$ and $^4\overline{\text{He}}/^3\overline{\text{He}} = (3.2 \pm 2.3(\text{stat})^{+0.7}_{-0.2}(\text{sys})) \times 10^{-3}$, which are consistent with the statistical model[33] and the coalescence model calculations[11]. The differential invariant yields for ^{4}He and

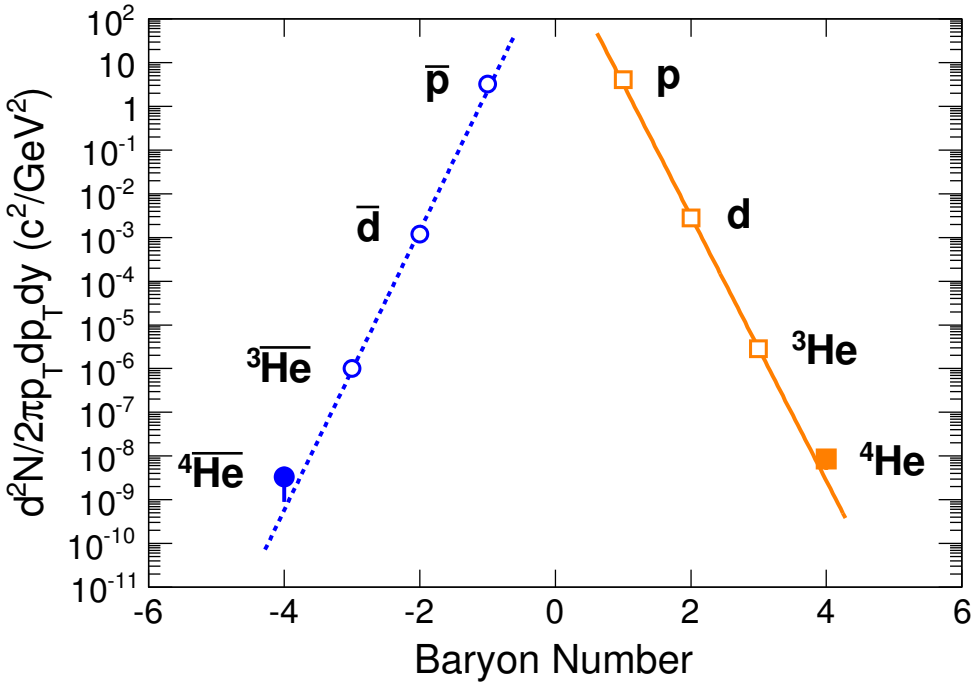

Figure 4-12: Differential invariant yields as a function of the baryon number B. The differential invariant yields were evaluated with a p_T window of $[0.75|\text{B}|, |\text{B}|]$ GeV/c, and a pseudo-rapidity window of $[-1.0, 1.0]$. The other data points besides ^{4}He and $^4\overline{\text{He}}$ are taken from [60, 61]. The lines represent the fits with the exponential formula $e^{-r|B|}$ for positive and negative particles separately.

$^4\overline{\text{He}}$ can be obtained by multiplying the ratios of ^{4}He/^{3}He and $^4\overline{\text{He}}/^3\overline{\text{He}}$ with previously measured ^{3}He and $^3\overline{\text{He}}$ differential invariant yields[61]. They are $(8.6 \pm 3.8(\text{stat})^{+0.9}_{-2.8}(\text{sys})) \times 10^{-9}$ and $(3.3 \pm 2.4(\text{stat})^{+0.5}_{-0.9}(\text{sys})) \times 10^{-9}$ for ^{4}He and $^4\overline{\text{He}}$, respectively. The systematic uncertain-

ties consist of background contaminations, feed-downs from hypertriton and antihypertriton, knock-out from beam pipe interactions, and the absorption in the material of detectors. They will be discussed in sections that follows. Figure 4-12 shows the differential invariant yields centered at $p_T = 0.875|\mathrm{B}|$ GeV/c for light (anti)nuclei as a function of their baryon numbers. Measurements other than ^{4}He and $^4\overline{\mathrm{He}}$ are taken from [60, 61]. Empirically, the production rate reduces by a factor of $1.6^{+1.0}_{-0.6} \times 10^3$ and $1.1^{+0.3}_{-0.2} \times 10^3$ by adding each additional antinucleon and nucleon to antinucleus and nucleus, respectively.

In a microscopic picture, light (anti)nucleus can be formed by coalescence during the last stage of the relativistic heavy-ion collisions. The production rate for light (anti)nucleus is proportional to the nucleon density in the phase space, therefore, presents an exponential behavior with respect to the baryon number. On the other hand, the statistic model, which regards the collision system as a fireball at a extremely high temperature, light (anti)nucleus, regarded as an object with energy $E = |\mathrm{B}|m_p$, can be emitted by the system with a probability determined by the Boltzmann factor $e^{-E/T}$. This model also produces the yield as an exponential of the baryon number. The considerations outlined above offer a good estimation for the production rate of heavier antinuclei. The yield of the stable antimatter nucleus next in line ($^6\overline{\mathrm{Li}}$) is predicted to be down by a factor of 2.6×10^6 compared to $^4\overline{\mathrm{He}}$ and is beyond the reach of current accelerator technology.

4.5 Backgrounds and corrections

4.5.1 Background estimation

Due to the finite TOF timing resolution and the mis-matching between TPC tracks and TOF hits, the $^3\overline{\mathrm{He}}$ mass distribution may be extended to the $^4\overline{\mathrm{He}}$ selection window, and

contributes to the background of $^4\overline{\text{He}}$. To determine the background contribution due to the

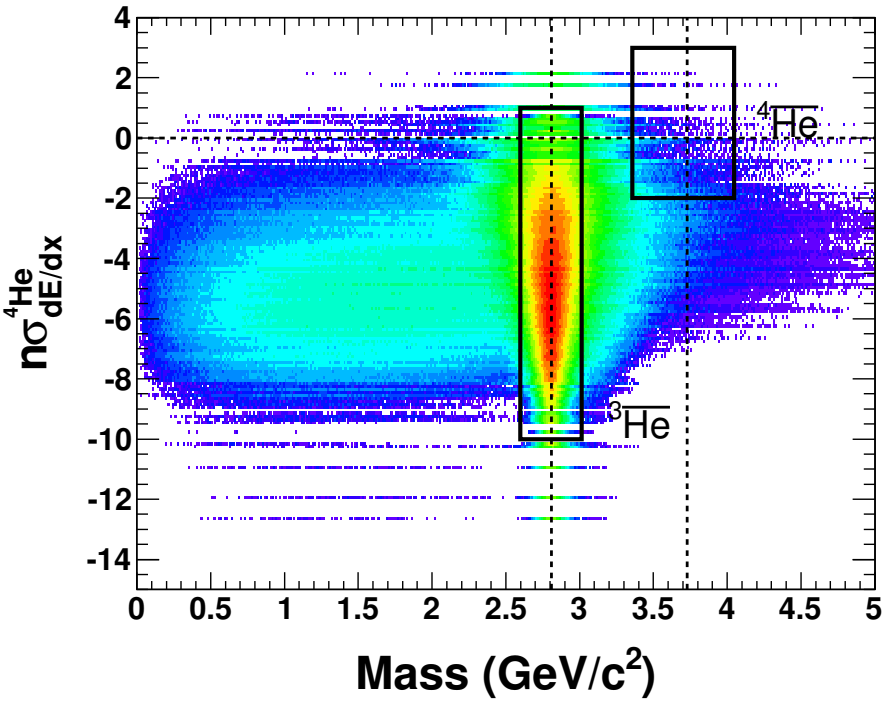

Figure 4-13: Reproduced $n\sigma^{^4He}_{dE/dx}$ vs. mass distribution based on a pure $^3\overline{\text{He}}$ sample and a random data sample. The vertical dashed lines indicate the theoretical mass values of $^3\overline{\text{He}}$ and $^4\overline{\text{He}}$, the horizontal line marks the position of $n\sigma^{^4He}_{dE/dx} = 0$. The rectangles shows the selection windows for $^3\overline{\text{He}}$ and $^4\overline{\text{He}}$.

finite TOF timing resolution, the $^3\overline{\text{He}}$ mass distribution is reproduced with each $^3\overline{\text{He}}$ track's expected time of flight, but smeared by time deviation $(t - t^{expected})$ of $^3\overline{\text{He}}$ from the same data sample. Similarly, to estimate the background contribution from the mis-matching between TPC tracks and corresponding TOF hits, the $^3\overline{\text{He}}$ mass value is calculated using each $^3\overline{\text{He}}$ track's expected time of flight and time deviation from a random data sample. Figure 4-13 presents the reproduced $n\sigma^{^4He}_{dE/dx}$ versus mass distribution. By projecting to the mass axis with a $n\sigma^{^4He}_{dE/dx}$ cut from -2.0 to 3.0. (Figure 4-14), the contamination of $^3\overline{\text{He}}$ to $^4\overline{\text{He}}$ can be estimated by integrating the reproduced $^3\overline{\text{He}}$ mass distribution over the mass selection window of 3.35 GeV/c^2 < mass < 4.04 GeV/c^2. The background contributes 1.4 and 0.05 counts of the 15 and 1 counts from the Au+Au collisions at 200 and 62

GeV, respectively. The probability of misidentification, calculated in the way of Poisson distribution, is 10^{-11}, corresponding to a signal significance larger than 6σ. The background of $^4\overline{\text{He}}$ and ^{4}He with different $n\sigma$ cuts are also calculated and presented in table 4-4.

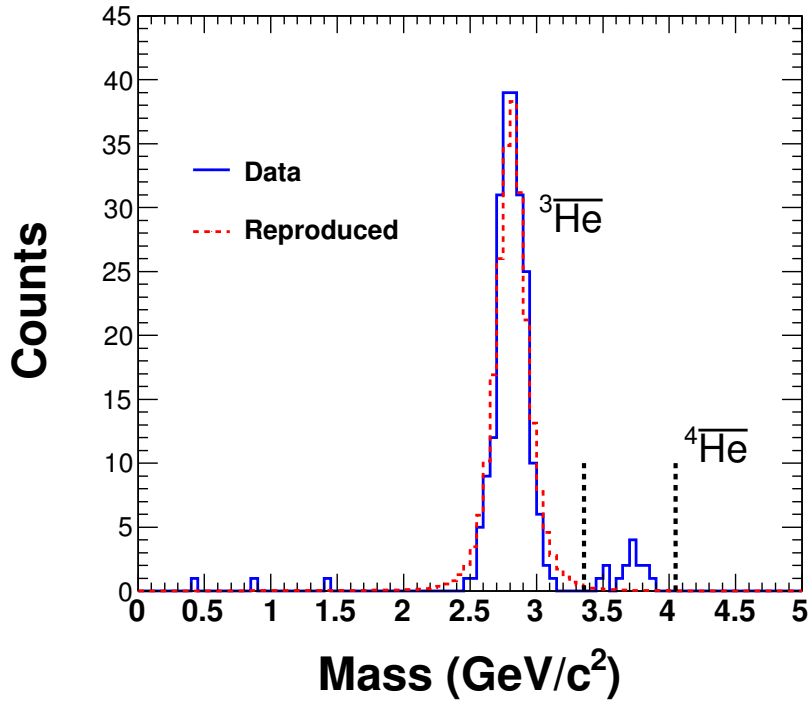

Figure 4-14: Mass distribution for $^3\overline{\text{He}}$, $^4\overline{\text{He}}$ (blue line), and reproduced $^3\overline{\text{He}}$ (dashed red line) from 200 GeV Au+Au collisions. Dashed black lines represent the $^4\overline{\text{He}}$ selection window used for $^4\overline{\text{He}}$ identification.

nσ	N($\overline{\alpha}$) - B	N(α) - B	Poisson(n,b) for $\overline{\alpha}$	Poisson(n,b) for α	N($^3\overline{\text{He}}$)	N(^{3}He)
[-3, 3]	17 - 2.5	26 - 5.5	1.6×10^{-9}	1.7×10^{-10}	2956	5904
[-2, 3]	15 - 1.4	26 - 3.5	2.6×10^{-11}	1.1×10^{-14}	2917	5854
[-1, 3]	11 - 0.57	21 - 1.6	2.7×10^{-11}	1.2×10^{-16}	2562	5242

Table 4-4: $^4\overline{\text{He}}$ and ^{4}He background with different nσ cuts.

4.5.2 Absorption

The absorption of $^3\overline{\text{He}}$ and $^4\overline{\text{He}}$, because of their annihilation with the material in STAR detectors, were estimated based on the annihilation correction of $\overline{\text{p}}$ analysis of STAR in

2001[62]. The $\overline{\text{p}}$ absorption loss correction factor, which is defined as the ratio between the total amount of protons created and that survived when passing through the material[62, 63], was parameterized as:

$$\text{Abs}^{\overline{\text{p}}}_{\text{corr}}(p) = \exp(\frac{0.089}{\sqrt{1+\gamma}} p^{-0.65} \frac{p}{p_T}), \tag{4-1}$$

where $\gamma = 1/\sqrt{1-\beta^2}$, and p and p_T are the momentum and transverse momentum, respectively. The parameter "0.089" is determined by the thickness of the material in STAR detector complex. The depth of the material can be calculated in the unit of radiation length (X_0), by summing over the beam pipe, SVT, TPC and TOF. They are $5.36\%X_0$ and $6.29\%X_0$ for run 2001 and 2010 respectively, therefore, the parameterization coefficient in equation 4-2 is estimated to be "0.104" for run 2010. On the other hand, a scaling of the inelastic cross section from pA to AA collisions:

$$\sigma_{\text{inel}}(^3\text{He},^4\text{He}) \approx (2, 2.56)\sigma_{\text{inel}}(\text{p}) \tag{4-2}$$

was applied to evaluate the annihilation cross section of $^3\overline{\text{He}}$ and $^4\overline{\text{He}}$ nucleus[64], by assuming that the scaling holds for $^3\overline{\text{He}}$ and $^4\overline{\text{He}}$. Therefore, the absorption correction factors for $^3\overline{\text{He}}$ and $^4\overline{\text{He}}$ in run 2010, can be parameterized as a function of the momentum and baryon number:

$$\text{Abs}_{\text{corr}}(p) = \exp(\frac{0.104a}{\sqrt{1+\gamma}} (\frac{p}{B})^{-0.65} \times \frac{p}{p_T}), \tag{4-3}$$

where, B is the baryon number, and a is the scaling factor of 2.0 (2.56) for $^3\overline{\text{He}}$($^4\overline{\text{He}}$). Figure 4-15 presents the absorption correction factor as a function of momentum for light antinucleus passing across the STAR detector in 2010. The absorption correction factors for $^3\overline{\text{He}}$ and $^4\overline{\text{He}}$ at $p_T = 0.875|\text{B}|$, where the $^4\overline{\text{He}}/^3\overline{\text{He}}$ ratio was evaluated, are 1.16 and 1.21, respectively.

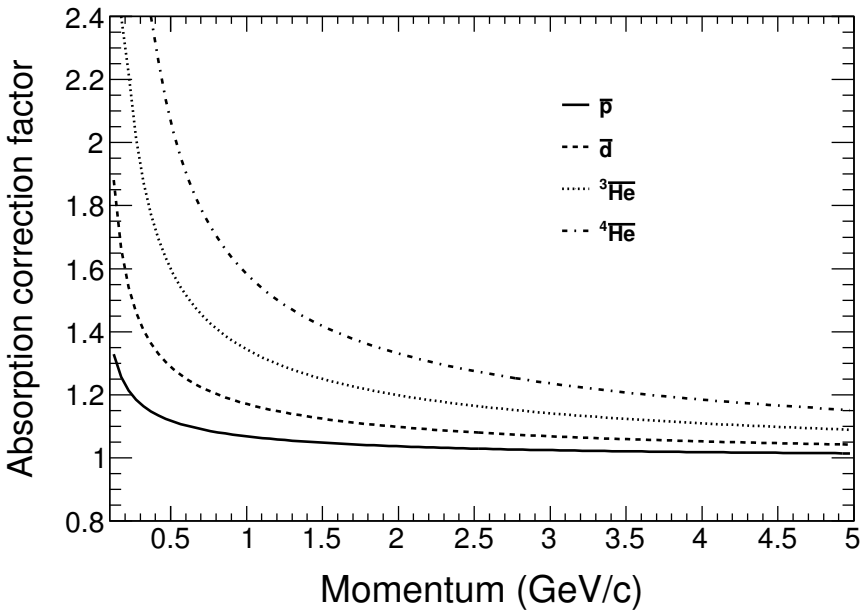

Figure 4-15: Absorption correction factors as a function of the momentum for light antinucleus interacting with the materials at the STAR experiment in 2010.

4.5.3 Beam pipe interaction

Positively charged particles knocked out from beam pipe interaction usually has a small momentum and a large distance of closest approach (*dca*) from the primary vertex, therefore, the contamination of ^{3}He and ^{4}He nucleus from beam pipe can be roughly estimated using the *dca* vs. p_T distribution. The rectangles in Figure 4-16 specify the different p_T and *dca* selection windows, especially "A" in each plot is the cut window used in the ^{4}He/^{3}He ratio measurement. Since, there is no contamination of knock-out for antinucleus, and most of the ^{3}He and ^{4}He nucleus in "A" and "D" are come from collisions and beam pipe interaction, respectively, one can calculate the contribution from knock-out in "A" based on two assumptions, 1) the $^3\overline{\text{He}}/^3$He ratio from real physics collisions is same in "A" and "B", and 2) the ratio of knock-out ^{3}He between "A" and "C" is the same as that between "B" and

"D". Then, the number of ^{3}He from knock-out in A, $\mathrm{N}_{^3\mathrm{He}}^{\mathrm{knock-out}}(\mathrm{A})$, can be calculated via:

$$\mathrm{N}_{^3\mathrm{He}}^{\mathrm{knock-out}}(\mathrm{A}) = \mathrm{N}_{^3\mathrm{He}}(\mathrm{C}) \times \frac{\mathrm{N}_{^3\mathrm{He}}(\mathrm{B}) - \frac{\mathrm{N}_{^3\mathrm{He}}(\mathrm{A})}{\mathrm{N}_{^3\overline{\mathrm{He}}}(\mathrm{A})} \times \mathrm{N}_{^3\overline{\mathrm{He}}}(\mathrm{B})}{\mathrm{N}_{^3\mathrm{He}}(\mathrm{D})} \tag{4-4}$$

It is estimated that the contamination from beam pipe interaction contribute 7.3 out of a total counts of 962 ^{3}He nucleus, corresponding a percentage of 0.76%, in the selected window "A". The knock-out contribution for ^{4}He nucleus can be simply evaluated, by assuming:

$$\frac{\mathrm{N}_{^4\mathrm{He}}^{\mathrm{knock-out}}(\mathrm{A})}{\mathrm{N}_{^4\mathrm{He}}(\mathrm{D})} = \frac{\mathrm{N}_{^3\mathrm{He}}^{\mathrm{knock-out}}(\mathrm{A})}{\mathrm{N}_{^3\mathrm{He}}(\mathrm{D})} \tag{4-5}$$

The knock-out ^{4}He contribute 0.28 in 5, a percentage of 5.6% in the selected cut window.

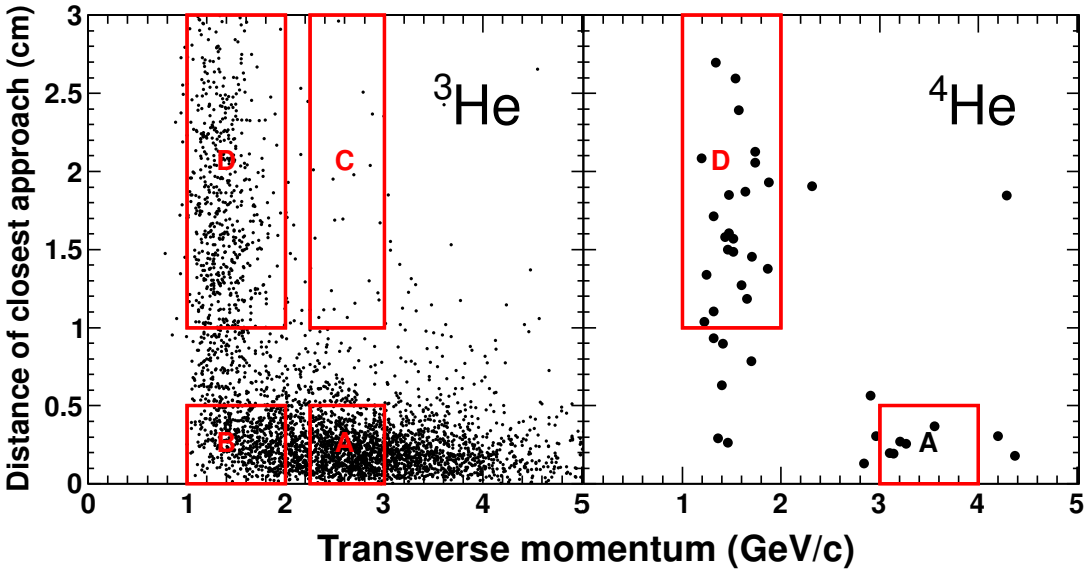

Figure 4-16: Distance of closest approach vs. transverse momentum distribution for ^{3}He nucleus (left), and ^{4}He nucleus (right), respectively. The rectangles outline different p_T and *dca* areas, which are used for estimating the knock out ^{3}He and ^{4}He at selected p_T and *dca* windows.

4.6 Systematic errors

4.6.1 Systematic errors in ^{4}He/^{3}He and $^4\overline{\mathrm{He}}$/$^3\overline{\mathrm{He}}$ measurement

The systematic errors of ^{4}He/^{3}He and $^4\overline{\mathrm{He}}$/$^3\overline{\mathrm{He}}$ measurement at middle pseudo-rapidity and $p_T \in [0.75|\mathrm{B}|, |\mathrm{B}|]$, is determined by the ^{4}He and $^4\overline{\mathrm{He}}$ background estimation, absorp-

tion effect for $^3\overline{\mathrm{He}}$ and $^4\overline{\mathrm{He}}$ in material, the knocked out ^{3}He and ^{4}He nucleus from beam pipe interaction, as well as the feed-down correction from ${}^3_\Lambda\mathrm{H}$ and ${}^3_\Lambda\overline{\mathrm{H}}$[31]. The ^{4}He and $^4\overline{\mathrm{He}}$ background subtraction and ^{3}He and $^3\overline{\mathrm{He}}$ from ${}^3_\Lambda\mathrm{H}$ and ${}^3_\Lambda\overline{\mathrm{H}}$ decay, are applicable for both ^{4}He/^{3}He and $^4\overline{\mathrm{He}}/^3\overline{\mathrm{He}}$ measurement, while absorption and knock-out are only for $^4\overline{\mathrm{He}}/^3\overline{\mathrm{He}}$ and ^{4}He/^{3}He, respectively. The percentage of contributions from the systematic errors talk above are listed as follows:

(a) ^{4}He and $^4\overline{\mathrm{He}}$ background subtraction: -6% for both ^{4}He/^{3}He and $^4\overline{\mathrm{He}}/^3\overline{\mathrm{He}}$;

(b) Absorption loss correction for $^3\overline{\mathrm{He}}$ and $^4\overline{\mathrm{He}}$: +4% for $^4\overline{\mathrm{He}}/^3\overline{\mathrm{He}}$;

(c) Knock out correction for ^{3}He and ^{4}He: -5% for ^{4}He/^{3}He;

(d) Feed-down correction for ^{3}He and $^3\overline{\mathrm{He}}$ from ${}^3_\Lambda\mathrm{H}$ and${}^3_\Lambda\overline{\mathrm{H}}$ decay: +18% for both ^{4}He/^{3}He and $^4\overline{\mathrm{He}}/^3\overline{\mathrm{He}}$;

The systematic uncertainties calculated via (a+b+c+d) is +18-11% for ^{4}He/^{3}He, and +22-6% for $^4\overline{\mathrm{He}}/^3\overline{\mathrm{He}}$ measurements. Considering the systematic errors, the ratios are $^4\mathrm{He}/^3\mathrm{He} = (3.0 \pm 1.3(\mathrm{stat})^{+0.5}_{-0.3}(\mathrm{sys})) \times 10^{-3}$ and $^4\overline{\mathrm{He}}/^3\overline{\mathrm{He}} = (3.2 \pm 2.3(\mathrm{stat})^{+0.7}_{-0.2}(\mathrm{sys})) \times 10^{-3}$, respectively.

4.6.2 Systematic errors in $^4\overline{\mathrm{He}}$ and ^{4}He invariant yields measurement

The ^{4}He and $^4\overline{\mathrm{He}}$ differential invariant yields were calculated by multiplying the ^{4}He/^{3}He and $^4\overline{\mathrm{He}}/^3\overline{\mathrm{He}}$ ratios with the previously measured ^{3}He and $^3\overline{\mathrm{He}}$ yields[61]. The ^{3}He and $^3\overline{\mathrm{He}}$ yields quoted are $(2.85 \pm 0.3(\mathrm{stat})^{+0.29}_{-0.63}(\mathrm{sys})) \times 10^{-6}$ and $(1.02 \pm 0.11(\mathrm{stat})^{+0.10}_{-0.22}(\mathrm{sys})) \times 10^{-6}$, respectively. The systematic errors consist of the TPC tracking

efficiency correction from embedding Monte-Carlo tracks into real events($\pm$10%)[65], and a correction of ^{3}He and $^3\overline{\mathrm{He}}$ yields because of the slight difference between the data point we used (p_T = 2.47 GeV/c) and the expected one (p_T = 2.625 GeV/c) (-12%). The systematic errors of ^{4}He and $^4\overline{\mathrm{He}}$ yields measurements are original from that of ^{4}He/^{3}He and $^4\overline{\mathrm{He}}$/$^3\overline{\mathrm{He}}$ and the previously measured ^{3}He and $^3\overline{\mathrm{He}}$, as shown below:

(a) ^{4}He and $^4\overline{\mathrm{He}}$ background subtraction: -6% for both ^{4}He and $^4\overline{\mathrm{He}}$;

(b) Absorption loss correction for $^3\overline{\mathrm{He}}$ and $^4\overline{\mathrm{He}}$: +4% for $^4\overline{\mathrm{He}}$;

(c) Knock out correction for ^{3}He and ^{4}He: -5% for ^{4}He;

(d) TPC tracking efficiency correction: $\pm$10% for both ^{4}He and $^4\overline{\mathrm{He}}$;

(e) Difference between used ^{3}He and $^3\overline{\mathrm{He}}$ yields (with p_T = 2.47 GeV/c) and the expected one (with p_T = 2.625 GeV/c): -12% for both ^{4}He and $^4\overline{\mathrm{He}}$;

The systematic uncertainty for ^{4}He and $^4\overline{\mathrm{He}}$ invariant yields measurement calculated via (a+b+c+d+e) is +10-33% and +14-28%, respectively.

Chapter 5 Coalescence production of light (anti)nuclei

The recent observation of antihypertriton ($^3_{\Lambda}\overline{\mathrm{H}}$) and antihelium-4 ($^4\overline{\mathrm{He}}$, or $\overline{\alpha}$) nuclei at RHIC have created a lot of excitations in the physics community and beyond. Theoretical calculations indicate that both thermal model[32, 33] and coalescence model based on a multiphase transport approach[66] can effectively describe the relative production abundance of light (anti)nuclei and (anti)hypernuclei in high energy heavy ion collisions. In addition, a vigorous simulation of hypernuclei and di-baryon production, by assuming thermal production from the intermediate phase of the UrQMD-hydro hybrid model and alternatively by the coalescence mechanism from a hadronic cascade model, are performed in a wide range of beam energy[67]. In this chapter, we present our calculation, based on DRoplet and hAdron GeneratOr for Nuclear collisions (DRAGON) model + a simple coalescence[11, 12, 14, 15], for the production of light (anti)nuclei and (anti)hypertriton as well as di-Λ in the most central Au+Au collisions. The invariant yields of ^{3}He($^3\overline{\mathrm{He}}$), $^3_{\Lambda}$H($^3_{\bar{\Lambda}}\overline{\mathrm{H}}$), and ^{4}He($^4\overline{\mathrm{He}}$) obtained with this approach is also found to be consistent with the STAR results. The coalescence parameters B_A (A = 2, 3, 4) are studied as a function of transverse momentum for d($\overline{\mathrm{d}}$), ^{3}He($^3\overline{\mathrm{He}}$), $^3_{\Lambda}$H($^3_{\bar{\Lambda}}\overline{\mathrm{H}}$), and ^{4}He($^4\overline{\mathrm{He}}$), respectively. B_2 for d($\overline{\mathrm{d}}$) and B_3 for ^{3}He($^3\overline{\mathrm{He}}$) are compa-

rable with the STAR measurement within statistical uncertainties. The p_T integrated yield for di-Λ is $dN_{\Lambda\Lambda}/dy \sim 2.23 \times 10^{-5}$, and is not strongly dependent on the parameter employed in the coalescence process. Combining the data points extracted from the PHENIX experiment, coalescence parameters exhibit a strong centrality dependence. An exponential behavior is seen if the differential invariant yields is plotted against the baryon number. The production rate reduces by 1.7×10^3 (1.3×10^3) for each additional antinucleon (nucleon) added to antinuclei (nuclei), roughly consistent with STAR's measurement. The yield of $^6\overline{\mathrm{Li}}$ is predicted to be 10^{-16}. Relative abundance of light anti(nuclei) and (anti)hypertriton are explored with particle ratios, and agree with experimental data as well as thermal model predictions.

5.1 DRAGON model

DRoplet and hAdron GeneratOr for Nuclear collisions (DRAGON) model[14, 15] assumes that, the fireball created in heavy ion collisions decays into fragments of spherical shape with

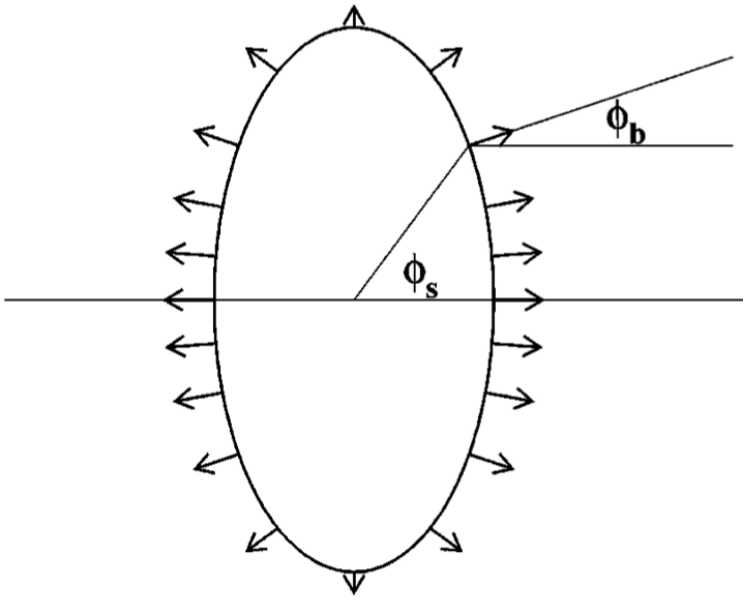

Figure 5-1: The fireball created in heavy ion collisions, with arrows indicating the directions of the four-component velocity.

a characteristic size. Both the bulk and the decayed fragments can produce hadrons and resonances. The fireball reaches the local thermal equilibrium and moves outward at a four-velocity u_μ. The model parameterizes the system with the kinetic freeze-out temperature T_k, the radial flow parameter ρ_0 and elliptic flow parameter ρ_2, the spatial anisotropy parameter a, the average transverse radius R, and the particle emission duration time τ_0. Figure 5-1 shows the interaction zone of heavy ion collisions, where the ϕ_s and ϕ_b are the angles of the space points and the four-velocity respect to the x axis, respectively. The fireball can be described in the frame of relativistic and polar coordinator (r, ϕ_s, η, τ), where the space-time rapidity $\eta = \frac{1}{2}\ln[(t+z)/(t-z)]$, the longitudinal proper time $\tau = \sqrt{t^2 - z^2}$. The four-velocity:

$$u_\mu = (\cosh\eta\cosh\rho, \cos\phi_b\sinh\rho, \sinh\phi_b\sinh\rho, \sinh\eta\cosh\rho), \tag{5-1}$$

where,

$$\rho = \tilde{r}\rho_0\sqrt{2}(1 + \rho_2\cos(2\phi_b)), \tag{5-2}$$

and,

$$\tilde{r} = \sqrt{\frac{(x^1)^2}{R_x^2} + \frac{(x^2)^2}{R_y^2}}, \qquad R_x = aR, \qquad R_y = \frac{R}{a}. \tag{5-3}$$

On the other hand, the fragments decay into hadrons at a probability, which is uniform over the entire volume of the droplet, and exponentially drops in time in their rest frame. The probability is:

$$P_t(\tau_d) = \frac{1}{R_d}\exp(-\frac{\tau_d}{R_d}), \tag{5-4}$$

where R_d is radius of the fragments.

Unlike the Cooper-Frye[27] characterization of the particle production in heavy ion collisions, the phase-space emission points for hadrons in DRAGON model are defined by a

Wigner function[13, 14]:

$$S(x,p)d^4x = \frac{2s+1}{(2\pi)^3} m_t \cosh(y-\eta) \exp(-\frac{p^\mu u_\mu}{T_k}) \Theta(1-\tilde{r}(r,\phi_s)) \\ H(\eta)\delta(\tau-\tau_0) d\tau\tau d\eta r dr d\phi_s, \tag{5-5}$$

where (2s+1) is the hadron spin degeneracy, and y is the rapidity. The azimuthally integrated p_T spectrum is defined as:

$$\frac{dN}{2\pi p_T dp_T} = \int S(x,p) d^4x. \tag{5-6}$$

Assuming chemical equilibrium, the particle abundance density n_i can be expressed in terms of follows the chemical freeze out temperature T_{ch}, chemical potential μ_B and μ_S.

$$n_i(T_{ch}, \mu_B, \mu_S) = g_i \int \frac{d^3p}{(2\pi)^3} [\exp(\frac{\sqrt{p^2+m_i^2} - (\mu_B B_i + \mu_S S_i)}{T_{ch}}) \pm 1]^{-1}. \tag{5-7}$$

where the upper (lower) sign is for bosons (fermions), and g_i is the degeneracy factor. The phase space data of hadrons generated by the DRAGON model is used to calculate the invariant yields, particle ratios, coalescence parameters of light (anti)nuclei, (anti)hypertriton and di-Λ, which will be presented in following sections.

5.2 Invariant yields

We focus on the central Au+Au collisions at RHIC energy in our calculation. The kinetic freeze-out temperature was extracted by the STAR experiment and fixed to be 89 MeV[65]. The radial flow parameter ρ_0 is equal to 0.91, while elliptic flow parameter ρ_2 and spatial anisotropy parameter a are set to be 0 and 1, respectively. The average transverse radius of the fireball R is 10 fm, and the finite longitudinal proper time is 6.2 fm/c[68–70]. Light (anti)nuclei are produced via coalescence during the last stage of the collision process. The quantum wave functions of the constituent nucleons, if close enough in momentum and coordinate space, will overlap to produce the (anti)nucleus. In our approach, we require that $\vec{r_i} - \vec{r_j} < 2R$ and $\vec{p_i} - \vec{p_j} < 100$ MeV, where $(\vec{r_i}, \vec{p_i})$ and $(\vec{r_j}, \vec{p_j})$ are the phase space positions

T_{ch}	T_{kin}	μ_B	μ_S	B_j	τ_0	ρ_0	ρ_2	R	a
159 MeV	89 MeV	22 MeV	3.9 MeV	0.84 GeV/fm^3	6.2 fm/c	0.91	0	10 fm	1.0

Table 5-1: The parameters used in the DRAGON model[65, 68–70] for 200 GeV central Au+Au collisions.

of any two of the constituent nucleons, and R is the nuclear force radius ($1.45 \times A^{1/3}$fm)[71]. Figure 5-2 shows the calculated differential yields of p($\overline{\text{p}}$), $\Lambda(\bar{\Lambda})$, light (anti)nuclei, as well

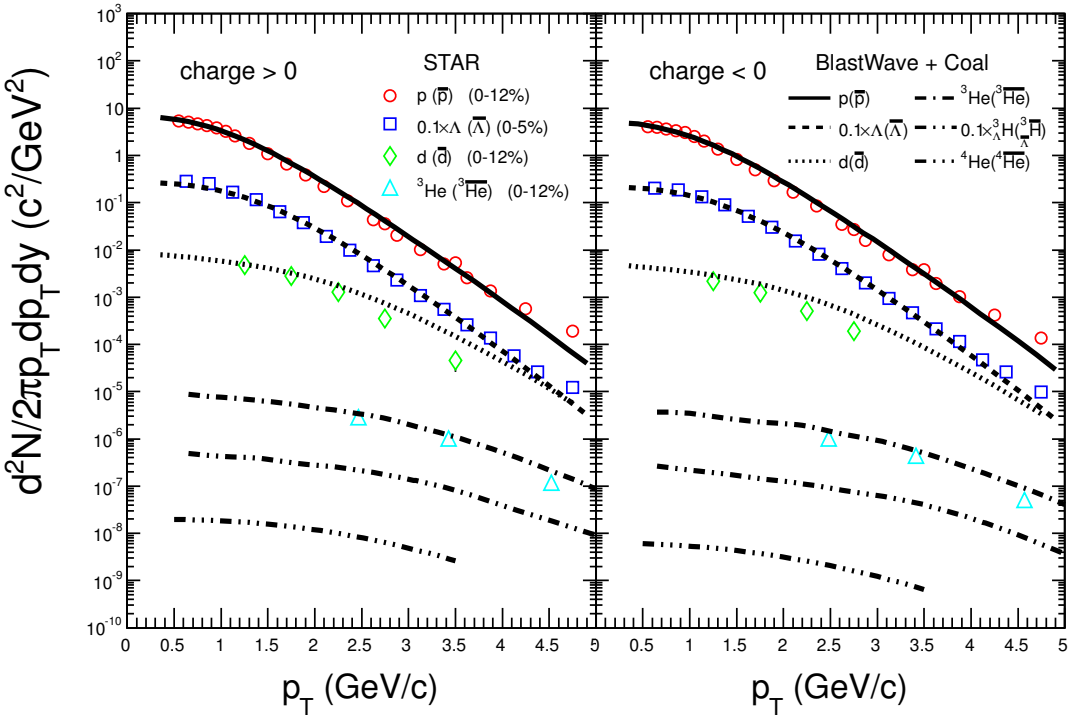

Figure 5-2: Differential invariant yields ($d^2N/2\pi p_T dp_T dy$) vs. p_T for p($\overline{\text{p}}$), $\Lambda(\bar{\Lambda})$ and light (anti)nuclei as well as (anti)hypertriton. The open symbols are experimental data points from the STAR measurement[61, 72, 73], and the black lines represent our calculations from the DRAGON model plus a coalescence model.

as (anti)hypertriton as a function of transverse momentum (p_T). This calculations can reproduce the data points extracted by the STAR experiment[61, 72, 73] very well.

The production rate of light (anti)nuclei as a function of baryon number is explored using their invariant yields at the average transverse momentum region ($p_T = 0.875|B|$ GeV/c). As shown in Figure 5-3, the open triangles represent the measurements made by the STAR experiment[9], while the solid ones are our calculations. A decreasing exponential trend of

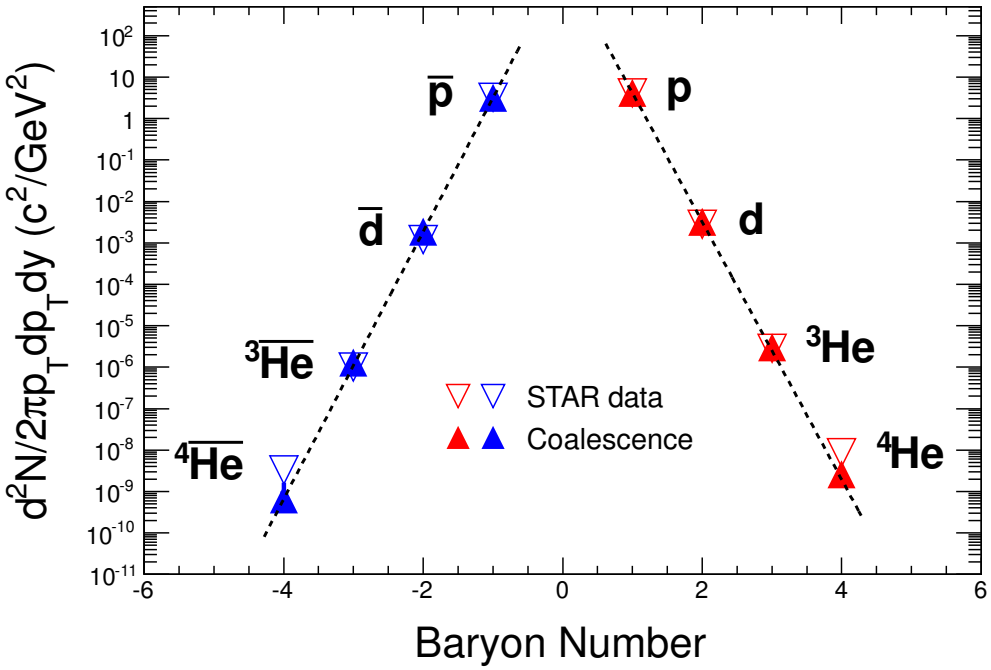

Figure 5-3: Invariant yields $d^2N/(2\pi p_T dp_T dy)$ of light (anti)nuclei at the average transverse momentum region ($p_T = 0.875|B|$ GeV/c) as a function of baryon number (B). The open symbols represent the data points extracted by the STAR experiment at RHIC energy[9], while solid ones are those from our coalescence model calculation. The lines represent the exponential fit for the coalescence results of positive particles (right) and negative particles (left) with the formula $e^{-r|B|}$.

the invariant yields with the increased atomic mass number is observed. The reduction factor obtained by fitting the distribution is 1.7×10^3 (1.3×10^3) for each additional antinucleon (nucleon) added, and is comparable with that measured by the STAR experiment. By extrapolating the distribution to B = -6 region, this study predicts that the yield of next stable antimatter nucleus in line ($^6\overline{\text{Li}}$), is a factor of 10^{-16}. The observation of $^6\overline{\text{Li}}$ in high energy heavy ion collisions seems impossible with current accelerator technology. On the other hand, the excitation of light (anti)nuclei from a highly correlated vacuum is discussed in reference[74]. Any deviation of the experimental data point from the model expectation should be a hint of the new production mechanism. Our results are consistent with the STAR measurement within uncertainties, and do not support the hypothesis of the excitation production from the vacuum.

5.3 Particle ratios

The p_T integrated yields (dN/dy) for light (anti)nuclei, and (anti)hypertriton were calculated at middle rapidity, as presented in table 5-2. Furthermore, the relative particle production abundances of light (anti)nuclei and (anti)hypernuclei are investigated and compared with RHIC data and the thermal model predictions. Figure 5-4 shows the particle

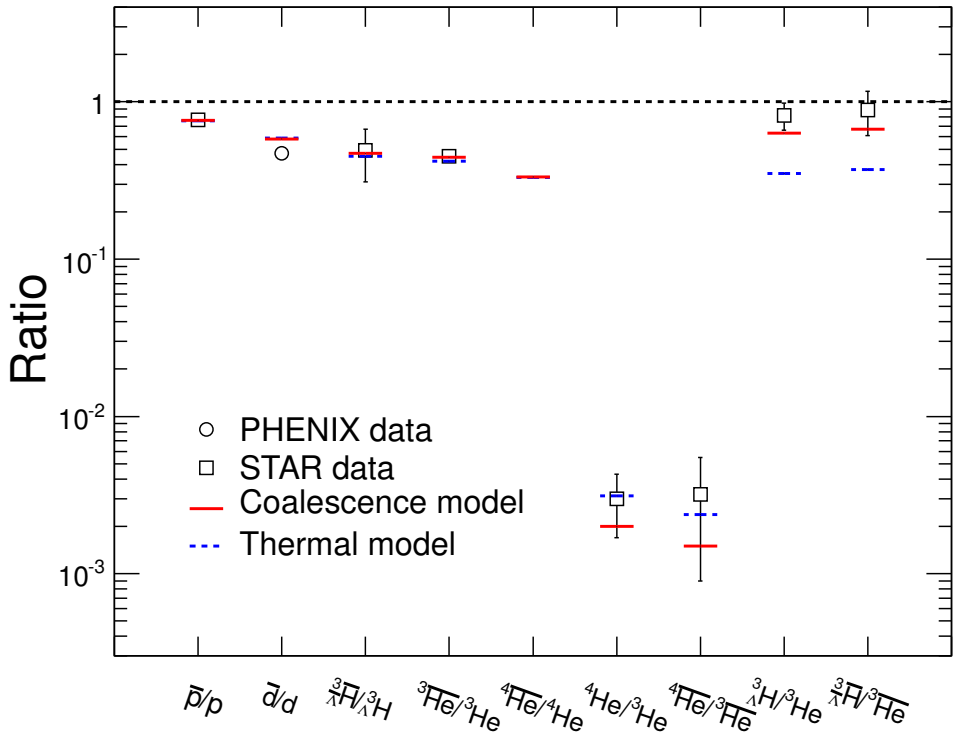

Figure 5-4: The comparison of particle ratios between data and model calculations. The data points are taken from the STAR and PHENIX experiments [9, 31, 56, 75]. The thermal model calculation is quoted from Ref. [33].

ratios for light (anti)nuclei and (anti)hypernuclei. Our results can fit the ratios of antinuclei to nuclei as well as ^{4}He/^{3}He and $^4\overline{\text{He}}/^3\overline{\text{He}}$ at RHIC energy very well [9, 31, 56, 75], and are also consistent with thermal model predictions. However, for $^3_\Lambda$H/^{3}He and $^3_\Lambda\overline{\text{H}}/^3\overline{\text{He}}$, the coalescence production mechanism has a better description than thermal results as declared

in reference[32].

Particle species	p	Λ	d	^{3}He	$^3_\Lambda$H	^{4}He
dN/dy	29.6	16.5	0.081	1.65×10^{-4}	1.05×10^{-4}	3.30×10^{-7}
Particle species	$\overline{\text{p}}$	$\overline{\Lambda}$	$\overline{\text{d}}$	$^3\overline{\text{He}}$	$^3_{\overline{\Lambda}}\overline{\text{H}}$	$^4\overline{\text{He}}$
dN/dy	22.6	13.1	0.047	7.3×10^{-5}	4.9×10^{-5}	1.10×10^{-7}

Table 5-2: p_T integrated yields (dN/dy) for p($\overline{\text{p}}$), $\Lambda(\bar{\Lambda})$, light (anti)nuclei, and (anti)hypertriton in central Au+Au collisions at 200 GeV.

5.4 Coalescence parameter B_A

The coalescence parameters B_A can be evaluated by comparing the invariant yields of the light (anti)nuclei and the primordial (anti)nucleons. B_A is interpreted to be inversely related to the fireball volume in coordinate space, i.e., $B_A \propto 1/V^{A-1}$[16], which was confirmed by the energy dependence of B_A[48]. Figure 5-5 presents $\sqrt[A-1]{B_A}$ as a function of transverse momentum. B_2, $\sqrt{B_3}$, and $\sqrt[3]{B_4}$ calculated based on the invariant yields of d($\overline{\text{d}}$), ^{3}He($^3\overline{\text{He}}$), $^3_\Lambda$H($^3_{\overline{\Lambda}}\overline{\text{H}}$) and ^{4}He($^4\overline{\text{He}}$) are consistent with the STAR B_2 results in central collisions[48]. The PHENIX measurements with d($\overline{\text{d}}$) spectra in other centralities are also included in the figure for reference[56]. Combining RHIC data and our calculation, the coalescence parameters B_A show a strong centrality dependence as shown in Figure 5-5, which means central collision usually create a larger fireball volume than peripheral one[48, 56]. On the other hand, the p_T dependence of $\sqrt[A-1]{B_A}$ is related to the position-momentum correlations in an expanding fireball, and provides information for the nucleon density profile and radial flow[56]. In addition, it is noticed that $\sqrt{B_3}$ of $^3_\Lambda$H is smaller than that of ^{3}He even though the two nuclei have the same mass number. This reflects the strangeness content dependence of the coalescence parameter, i.e, there exists an additional penalty factor due to strangeness. Overall, this calculation with an uniform nucleon density plus an outward velocity can reproduce the PHENIX results, which also consistent with previous model calculations[16,

76].

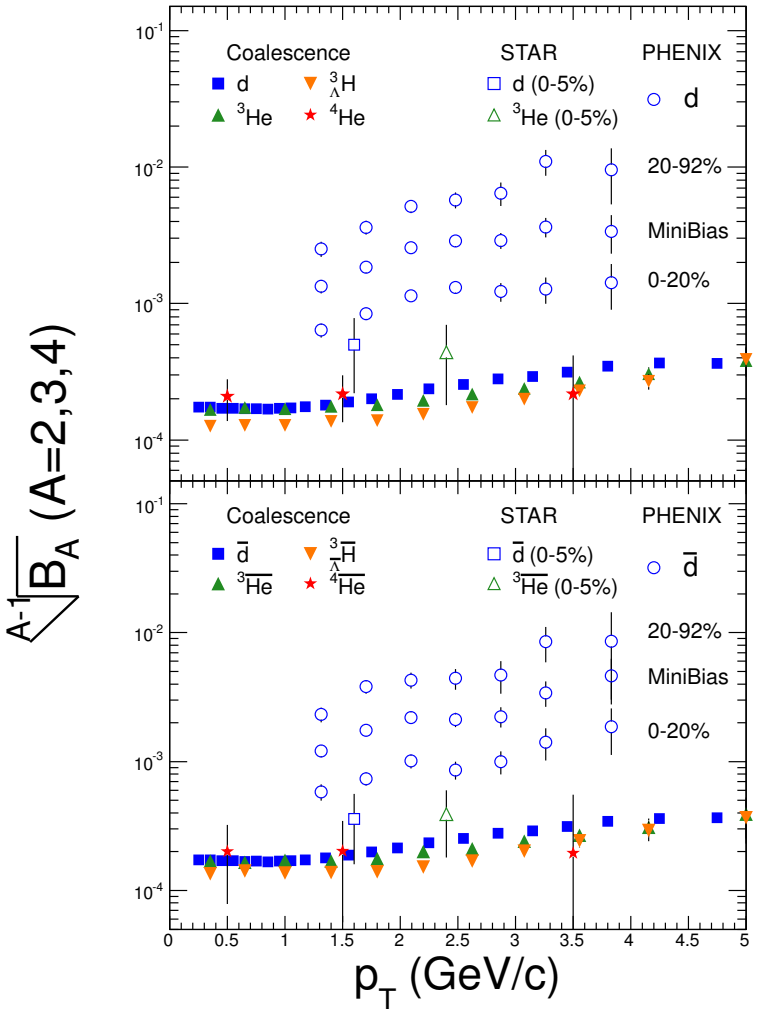

Figure 5-5: Coalescence parameters B_A as a function of p_T for light nuclei (top panel) and antinuclei (bottom panel). The solid symbols are our results for different types of light (anti)nuclei. The open rectangles and triangles are the data points from STAR measurements[61]. The open circles that present a centrality dependence is measured by the PHENIX experiment[56].

5.5 H particle production

The existence of exotic forms of deeply bounded dibaryons have been proposed, and the H particle ($uuddss$), also known as the di-Λ, was predicted to be existed by R. L. Jaffe in 1976[77]. Later, some other bound dibaryons were also proposed, e.g., a bound di-Ω state

predicted within the framework of the chiral SU(3) quark model[78]. However, the H particle

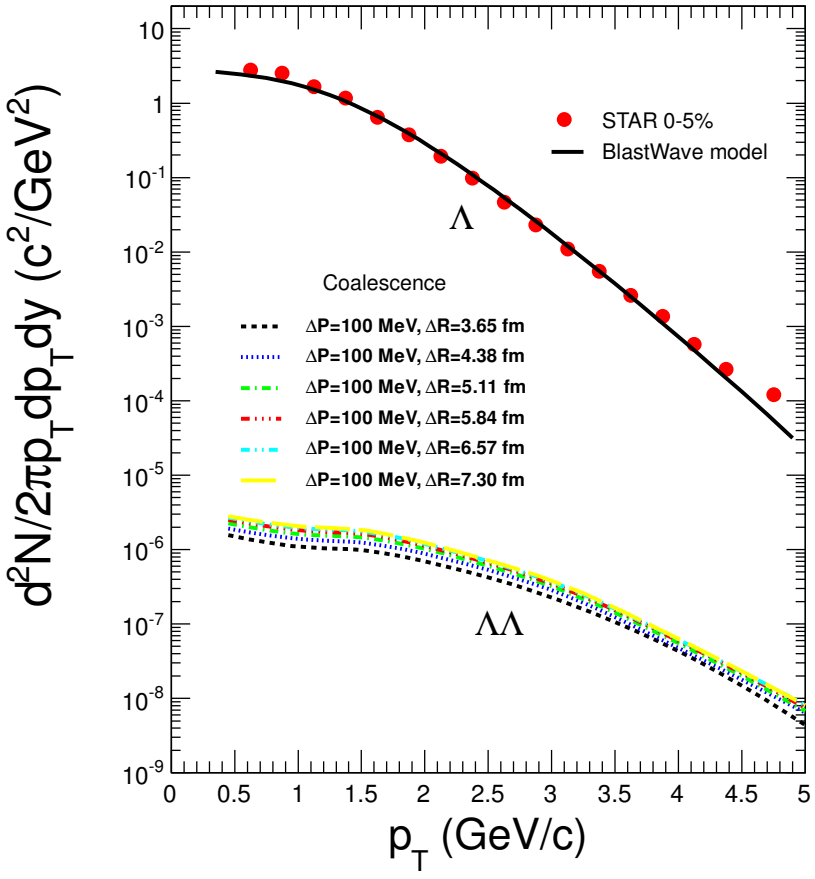

Figure 5-6: Differential invariant yields ($d^2N/2\pi p_T dp_T dy$) versus p_T for Λ and di-Λ. The red solid circles are experimental data points extracted by the STAR experiment[73]. The solid line is our calculation based on the DRAGON model. The dashed lines are the production rate of di-Λ calculated via a simple coalescence model with varied coalescence parameters based on the phase-space data of Λ.

and any other dibaryons are still not experimentally observed yet[79–81]. More recently, some theoretical progresses on di-Λ have been made[82–92], and further theoretical efforts, including quantitative estimation for the invariant yield of di-Λ, are still very useful. The constituent quarks of H particle are $uuddss$, with spin factor $J = 0$, isospin number $I = 0$, and strangeness number $S = -2$. The predicted mass value of H particle, $m_{\rm H}$ is of 2150 MeV. The invariant yield of H particle in heavy ion collision is calculated using the same approach

employed in our light (anti)nuclei study. Figure 5-6 presents the differential invariant yields ($d^2N/2\pi p_T dp_T dy$) as a function of p_T for Λ and di-Λ within this framework. It shows that our calculation can reproduce the Λ spectra extracted by the STAR experiment[73] very well. The production rate of H particle based on the phase space data of Λ and the coalescence model, is not dependent on the parameters used in coalescence. The p_T integrated yield of H particle in our calculation is $dN_{\Lambda\Lambda}/dy \sim 2.234 \times 10^{-5}$.

Chapter 6 Conclusions and Outlook

6.1 Conclusions

In summary, a STAR online high level trigger (HLT) has been developed. Its components and corresponding functionalities are presented. That include online tracking, online trigger algorithm, online monitoring, as well as offline software implementation. Calibration methods for TPC and TOF were set up and applied to the HLT online data-taking successfully. The observation of $^4\overline{\mathrm{He}}$ nucleus, the heaviest antinucleus detected to date, has been made based on the dataset selected by the HLT at the STAR experiment.

The $^4\overline{\mathrm{He}}$ identification relies on the measurements of their energy loss ($\langle dE/dx \rangle$) in TPC and time of flight measured by TOF. In total, 18 $^4\overline{\mathrm{He}}$ counts have been detected. Of those, 2 of them were identified by TPC alone with data recorded in 2007, 15 and 1 were identified by both TPC and TOF from Au+Au collisions at 200 GeV and 62 GeV in 2010, respectively. All candidates have been visually checked with STAR event display. The backgrounds due to the finite TOF timing resolution and the mis-matching between TPC tracks and fired TOF hits were estimated to be 1.4 and 0.05 in Au+Au 200 GeV and 62 GeV, respectively. Considering the background, the misidentification probability of $^4\overline{\mathrm{He}}$ nucleus is lower than

10^{-11}, corresponding to a signal significance larger than 6σ.

The particle ratios of ^{4}He/^{3}He and $^4\overline{\text{He}}/^3\overline{\text{He}}$ are measured for 200 GeV central Au+Au collisions. They are, $^4\text{He}/^3\text{He} = (3.0 \pm 1.3(\text{stat})^{+0.5}_{-0.3}(\text{sys})) \times 10^{-3}$ and $^4\overline{\text{He}}/^3\overline{\text{He}} = (3.2 \pm 2.3(\text{stat})^{+0.7}_{-0.2}(\text{sys})) \times 10^{-3}$, and are consistent with the predictions from the statistical model and the coalescence model. The differential invariant yields for ^{4}He and $^4\overline{\text{He}}$ obtained by multiplying the ratios of ^{4}He/^{3}He and $^4\overline{\text{He}}/^3\overline{\text{He}}$ with previously measured ^{3}He and $^3\overline{\text{He}}$ yields, are $(8.6 \pm 3.8(\text{stat})^{+0.9}_{-2.8}(\text{sys})) \times 10^{-9}$ and $(3.3 \pm 2.4(\text{stat})^{+0.5}_{-0.9}(\text{sys})) \times 10^{-9}$, respectively. The differential invariant yields for light (anti)nuclei as a function of baryon number exhibit an exponential behavior, and the production rate reduces by a factor of $1.6^{+1.0}_{-0.6} \times 10^3$ and $1.1^{+0.3}_{-0.2} \times 10^3$ for each additional antinucleon and nucleon added to the antinuclei and nuclei, respectively. The yield of the stable antimatter nucleus next in line (B = -6) is predicted to be down by a factor of 2.6×10^6, compared to $^4\overline{\text{He}}$, and is beyond the reach of current accelerator technology. Barring the dramatic observation of $^6\overline{\text{Li}}$ and heavier antinucleus in cosmic radiation or a new breakthrough in accelerator technology, it is likely that $^4\overline{\text{He}}$ will remain the heaviest stable antimatter nucleus observed in the foreseeable future.

A rigorous calculation for the production of light (anti)nuclei, (anti)hypertriton, and di-Λ at RHIC energy has been presented based on the DRAGON model and a simple coalescence mechanism. The invariant yields of ^{3}He($^3\overline{\text{He}}$), $^3_\Lambda$H($^3_{\overline{\Lambda}}\overline{\text{H}}$), and ^{4}He($^4\overline{\text{He}}$) obtained within current framework are found to be consistent with the STAR measurements. The coalescence parameters B_A (A = 2, 3, 4) has been studied as a function of transverse momentum for d($\overline{\text{d}}$), ^{3}He($^3\overline{\text{He}}$), $^3_\Lambda$H($^3_{\overline{\Lambda}}\overline{\text{H}}$), and ^{4}He($^4\overline{\text{He}}$), respectively. B_2 for d($\overline{\text{d}}$) and B_3 for ^{3}He($^3\overline{\text{He}}$) are comparable with the STAR measurement within statistical uncertainty. The p_T integrated yields for di-Λ is $dN_{\Lambda\Lambda}/dy \sim 2.23 \times 10^{-5}$, and is not dependent on the parameter employed in the coalescence process. Combining the data points extracted by the PHENIX Collabo-

ration, the coalescence parameters exhibit a strong centrality dependence. An exponential behavior is shown for the differential invariant yields versus the baryon number. The production rate decreases by a factor of 1.7×10^3 (1.3×10^3) for each additional antinucleon (nucleon) added to antinuclei (nuclei), which is consistent with the STAR measurements. The production rate of $^6\overline{\text{Li}}$ is predicted to be 10^{-16}. Relative abundance of light anti(nuclei) and (anti)hypertriton are explored with particle ratios, and agree with experimental data as well as the thermal model predictions.

6.2 Outlook

The search of $^4\overline{\text{He}}$ and heavier antinucleus in the Universe is one of the major motivations of space shuttle based apparatus such as the Alpha Magnetic Spectrometer (AMS). The sensitivity of the space based detectors is below what would be needed to observe a $^4\overline{\text{He}}$ nucleus produced by nuclear interactions in the cosmos, and consequently, any observation of $^4\overline{\text{He}}$ nuckeus or even heavier antinuclei in space would indicate the existence of a large amount of antimatter elsewhere in the Universe[1–3, 93]. Both our measurement

Figure 6-1: The Alpha Magnetic Spectrometer (AMS-02) in the International Space Station (ISS).

made at the STAR experiment and the model calculation provide points of references for possible future observation of $^4\overline{\text{He}}$ nucleus in cosmic radiation. So far, the efforts of searching for heavy antimatter fragments haven't yielded any positive result. The Balloon-borne Experiment with Superconducting Spectrometer (BESS collaboration)[94, 95] has found no $\overline{\text{d}}$ or $^4\overline{\text{He}}$ candidates. They derived an upper limit of 1.9×10^{-4} $(\text{m}^2.\text{s.sr.GeV/nucleon})^{-1}$ for differential flux of cosmic ray $\overline{\text{d}}$ at 95% confidence level, between 0.17 and 1.15 GeV/nucleon at the top of the atmosphere[94]. For $^4\overline{\text{He}}$, a 95% confidence upper limit to the possible abundance of $^4\overline{\text{He}}$ relative to ^{4}He of 6.9×10^{-8} was determined. The AMS-02 was designed to measure the composition of cosmic rays with a accuracy of 10^{-9} up to TeV region. It has been searching for the cosmic ray $^4\overline{\text{He}}$ nucleus, since its launch and installation in international space station (ISS) in 2011. If no $^4\overline{\text{He}}$ or even heavier antinucleus observed by AMS-02, the baryon asymmetry hypothesis will be strongly supported with no existing antimatter to the edge of observable universe[96]. As AMS-02 and other space based experiments are actively taking data, hopefully in the near future a clearer answer can be found.

Bibliography

[1] S. Ahlen et al., Nucl. Instr. and Meth. A **350**, 351 (1994).

[2] M. Casolino et al., Advances in Space Research **42**, 455 (2008).

[3] S. Orito et al., Phys. Rev. Lett. **84**, 1078 (2000).

[4] A. Yamamoto et al., Adv. Space Res. **14**, 75 (1994).

[5] V. Bonicini et al., Nucl. Instr. and Meth. A **461**, 262 (2011).

[6] J. Alcaraz et al., Phys. Lett. B **461**, 387 (1999).

[7] J. Adame et al., Nucl. Phys. A **757**, 102 (2005).

[8] P. B. Munzinger and J. Stachel, Nature **448**, 302 (2007).

[9] H. Agakishiev et al., Nature **473**, 353 (2011).

[10] L. Xue, J. Phys. G: Nucl. Part. Phys **38**, 124072 (2011).

[11] L. Xue, Y. G. Ma, J. H. Chen, and S. Zhang, Phys. Rev. C **85**, 064912 (2012).

[12] Y. G. Ma, J. H. Chen, and L. Xue, Front. Phys **7**, 637 (2012).

[13] F. Retière and M. A. Lisa, Phys. Rev. C **70**, 044907 (2004).

[14] B. Tomasik, Acta Phys. Polon. B **36**, 2087 (2005).

[15] B. Tomasik, Computer Physics Communications **180**, 1642 (2009).

[16] R. Scheibl and U. Heinz, Phys. Rev. C **59**, 1585 (1999).

[17] H. Sato, Phys. Lett. B **98**, 153 (1981).

[18] M. Schmelling, arXiv:hep-ex/9701002 (1996).

[19] F. Karsch, Nucl. Phys. A **698**, 199 (2002).

[20] F. Karsch, E. Laermann, and A. Peikert, Phys. Lett. **B478**, 447 (2000).

[21] J. Adams et al., Phys. Rev. Lett. **91**, 072304 (2003).

[22] C. Blume, arXiv:nucl-ex/0609022v1 (2006).

[23] J. Adams et al., Phys. Rev. Lett. **92**, 052302 (2004).

[24] D. Molnar and S. A. Voloshin., Phys. Rev. Lett **91**, 092301 (2003).

[25] S. T. Butler and C. A. Pearson, Phys. Rev. Lett. **7**, 69 (1961).

[26] B. I. Abelev et al., Phys. Rev. Lett. **99**, 112301 (2007).

[27] F. Cooper and G. Frye, Phys. Rev. D **10**, 186 (1974).

[28] T. A. Armstrong et al., Phys. Rev. C **70**, 024902 (2004).

[29] T. A. Armstrong et al., Phys. Rev. C **61**, 064908 (2000).

[30] V. I. Kolesnikov, J. Phys. Conf. Ser. **110**, 032010 (2008).

[31] B. I. Abelev et al., Science **328**, 58 (2010).

[32] J. Cleymans et al., Phys. Rev. C **84**, 054916 (2011).

[33] A. Andronic et al., Physics Letters B **697**, 203 (2011).

[34] M. Danysz and J. Pniewski, Philos. Mag. **44**, 348 (1953).

[35] J. H. Chen, Nucl. Phys. A **835**, 117 (2010).

[36] J. Rafelski and B. Müller, Phys. Rev. Lett. **48**, 1066 (1982).

[37] F. Bergsma et al., Nucl. Instr. and Meth. A **499**, 633 (2003).

[38] M. Anderson et al., Nucl. Instr. and Meth. A **499**, 659 (2003).

[39] H. Bichsel, Nucl. Instr. and Meth. A **562**, 154 (2006).

[40] S. Eidelman et al., Phys. Lett. **B592**, 1 (2004).

[41] B. Bonner et al., Nucl. Instr. and Meth. A **508**, 181 (2003).

[42] H. F. Chen et al., High Energy Physics And Nuclear Physics **26**, 201 (2002).

[43] M. C. S. Williams et al., Nucl. Instr. and Meth. A **434**, 362 (1999).

[44] M. C. S. Williams, Nucl. Phys. A **698**, 464 (2002).

[45] J. Adams et al., Physics Letters B **616**, 8 (2005).

[46] M. Shao et al., Nucl. Instr. and Meth. A **558**, 419 (2006).

[47] F. S. Bieser et al., Nucl. Instr. and Meth. A **499**, 766 (2003).

[48] J. H. Zhou, Ph.D. thesis, Rice University (2009).

[49] A. Schuster, Nature **58**, 367 (1898).

[50] P. A. M. Dirac, Proc. R. Soc. Lond. A **117**, 610 (1928).

[51] C. D. Anderson, Phys. Rev. **43**, 491 (1933).

[52] C. J. Kevane, Science **133**, 580 (1961).

[53] C. W. O. Chamberlain, E. Segrè and T. Ypsilantis, Phys. Rev. **100**, 947 (1956).

[54] C. Hailey et al., Advances in Space Research **51**, 290 (2013).

[55] S. W. A. Ibarra, Journal of Cosmology and Astroparticle Physics **2013**, 21 (2013).

[56] S. Adler et al., Phys. Rev. Lett. **94**, 122302 (2005).

[57] G. B. Andresen et al., Nature **468**, 673 (2010).

[58] G. B. Andresen et al., Nature Physics **7**, 558 (2011).

[59] X. P. Zhang, Ph.D. thesis, Nanjing University (2010).

[60] H. D. Liu, PhD thesis, USTC (2007).

[61] B. I. Abelev et al., arXiv:nucl-ex 0909.0566 (2009).

[62] C. Adler et al., Phys. Rev. Lett. **87**, 262302 (2001).

[63] C. Struck, Ph.D. thesis, Goethe University Frankfurt am Main (2003).

[64] T. F. Hoang, B. Cork, and H. J. Crawford, Z. Phys. C **29**, 611 (1985).

[65] B. I. Abelev et al., Phys. Rev. C **79**, 034909 (2009).

[66] S. Zhang et al., Physics Letters B **684**, 224 (2010).

[67] J. Steinheimer et al., arXiv:nucl-th 1203.2547 (2012).

[68] K. Geiger, Phys. Rep. C **258**, 237 (1995).

[69] J. W. Harris et al., Ann. Rev. Nucl. Part. Sci **46**, 71 (1996).

[70] B. Müller, Nucl. Phys. A **630**, 461 (1998).

[71] J. L. Nagle et al., Phys. Rev. C **53**, 367 (1996).

[72] B. I. Abelev et al., Phys. Lett. B **655**, 104 (2007).

[73] G. Agakishiev et al., Phys. Rev. Lett **108**, 072301 (2012).

[74] W. Greiner, Int. J. Mod. Phys. E **5** (1996).

[75] J. Adams et al., Phys. Rev. Lett. **92**, 112301 (2004).

[76] A. Polleri et al., Phys. Lett. B **419**, 19 (1998).

[77] R. L. Jaffe, Phys. Rev. Lett. **38**, 195 (1977).

[78] Z. Y. Zhang et al., Phys. Rev. C. **61**, 065204 (2000).

[79] K. Yamamoto et al., Phys. Lett. B **478**, 401 (2000).

[80] A. L. Trattner, Ph.D. thesis, UC Berkeley [UMI-32-54109]. (2006).

[81] C. J. Yoon et al., Phys. Rev. C **75**, 022201 (2007).

[82] T. Sakai et al., Theor. Phys. Suppl. **137**, 121 (2000).

[83] P. J. Mulders et al., J. Phys. G **9**, 1159 (1983).

[84] P. B. Mackenzie et al., Phys. Rev. Lett **55**, 2539 (1985).

[85] Y. Iwasaki et al., Phys. Rev. Lett **60**, 1371 (1988).

[86] A. Pochinsky et al., Nucl. Phys. B, Proc. Suppl. **73**, 255 (1999).

[87] I. Wetzorke et al., Nucl. Phys. B, Proc. Suppl. **83**, 218 (2000).

[88] I. Wetzorke et al., Nucl. Phys. B, Proc. Suppl. **119**, 278 (2003).

[89] Z. H. Luo et al., Mod. Phys. Lett. A **22**, 591 (2007).

[90] S. R. Beane et al., Phys. Rev. D **81**, 054505 (2010).

[91] S. R. Beane et al. (NPLQCD Collaboration), Phys. Rev. Lett. **106**, 162001 (2011).

[92] T. Inoue, arXiv:1109.1620v1 (2011).

[93] K. Abe et al., Phys. Rev. Lett. **108**, 131301 (2012).

[94] H. Fuke et al., Phys. Rev. Lett. **95**, 081101 (2005).

[95] K. Abe et al., Phys. Rev. Lett. **108**, 131301 (2012).

[96] R. Battiston, Nucl. Instr. and Meth. A **588**, 227 (2008).

List of Figures

List of Tables

Publications and Presentations

- Publications

  1. Observation of the antimatter helium-4 nucleus
     H. Agakishiev et al.
     Nature. 473 (2011) 353
  2. Observation of the antimatter helium-4 nucleus at the RHIC
     L. Xue for the STAR Collaboration
     J. Phys. G: Nucl. Part. Phys. 38 (2011) 124072
  3. Production of light (anti)nuclei, (anti)hypertriton, and di-Lambda in central Au+Au collisions at energies available at the BNL Relativistic Heavy Ion Collider
     L. Xue, Y. G. Ma, J. H. Chen, S. Zhang
     Phys. Rev. C 85 (2012) 064912
  4. Phenomenological study of light (anti)nuclei, (anti)hypertriton and di-Lambda production at RHIC
     L. Xue, Y. G. Ma, J. H. Chen, S. Zhang
     Nuclear Structure in China 2012: Proceedings of the 14th National Conference on Nuclear Structure in China (NSC2012) (World Scientific, Singapore)
  5. A brief review of antimatter production
     Y. G. Ma, J. H. Chen, L. Xue
     Front. Phys 7(6): 637-646 (2012)
  6. Hunting antimatter nuclei in ultrarelativistic heavy-ion collisions
     Y.G. Ma, J. H. Chen, L. Xue, A. H. Tang, Z. B. Xu
     Nuclear Physics News, in press (2013) as a Feature Article

- Other publications

  1. System size and energy dependence of near-side dihadron correlations
     H. Agakishiev et al., (STAR Collaboration)
     Phys. Rev. C 85 (2012) 14903

2. Identified Hadron Compositions in p+p and Au+Au Collisions at High Transverse Momenta at $\sqrt{s_{NN}}$= 200 GeV
   H. Agakishiev et al., (STAR Collaboration)
   Phys. Rev. Lett. 108 (2012) 72302
3. Directed and elliptic flow of charged particles in Cu+Cu collisions at $\sqrt{s_{NN}}$=22.4 GeV
   H. Agakishiev et al., (STAR Collaboration)
   Phys. Rev. C 85 (2012) 14901
4. ρ^0 photoproduction in Au+Au collisions at $\sqrt{s_{NN}}$=62.4 GeV measured with the STAR detector
   H. Agakishiev et al., (STAR Collaboration)
   Phys. Rev. C 85 (2012) 14910
5. Strangeness Enhancement in Cu+Cu and Au+Au Collisions at $\sqrt{s_{NN}}$=200 GeV
   H. Agakishiev et al., (STAR Collaboration)
   Phys. Rev. Lett. 108 (2012) 72301
6. Evolution of the differential transverse momentum correlation function with centrality in Au + Au collisions at $\sqrt{s_{NN}}$=200 GeV
   H. Agakishiev et al., (STAR Collaboration)
   Phys. Lett. B 704 (2011) 467
7. Experimental studies of di-jet survival and surface emission bias in Au+Au collisions via angular correlations with respect to back-to-back leading hadrons
   H. Agakishiev et al., (STAR Collaboration)
   Phys. Rev. C 83 (2011) 061901
8. High pT nonphotonic electron production in p+p collisions at $\sqrt{s_{NN}}$=200 GeV
   H. Agakishiev et al., (STAR Collaboration)
   Phys. Rev. D 83 (2011) 052006
9. Strange and multistrange particle production in Au + Au collisions at $\sqrt{s_{NN}}$=62.4 GeV
   M. M. Aggarwal et al., (STAR Collaboration)
   Phys. Rev. C 83 (2011) 024901
10. Measurement of the Parity-Violating Longitudinal Single-Spin Asymmetry for $W^{\pm}$ Boson Production in Polarized Proton-Proton Collisions at $\sqrt{s_{NN}}$=500 GeV
    M. M. Aggarwal et al., (STAR Collaboration)
    Phys. Rev. Lett. 106 (2011) 062002
11. Scaling properties at freeze-out in relativistic heavy-ion collisions
    M. M. Aggarwal et al., (STAR Collaboration)
    Phys. Rev. C 83 (2011) 034910
12. Measurement of the Bottom Quark Contribution to Nonphotonic Electron Production in p+p Collisions at $\sqrt{s_{NN}}$=200 GeV
    M. M. Aggarwal et al., (STAR Collaboration)
    Phys. Rev. Lett. 105 (2010) 202301

13. K^{*0} production in Cu+Cu and Au+Au collisions at $\sqrt{s_{NN}}$=62.4 GeV and $\sqrt{s_{NN}}$=200 GeV
    M. M. Aggarwal et al., (STAR Collaboration)
    Phys. Rev. C 84 (2011) 34909
14. Balance functions from Au+Au, d+Au, and p+p collisions at $\sqrt{s_{NN}}$=200 GeV
    M. M. Aggarwal et al., (STAR Collaboration)
    Phys. Rev. C 82 (2010) 024905
15. Higher Moments of Net Proton Multiplicity Distributions at RHIC
    M. M. Aggarwal et al., (STAR Collaboration)
    Phys. Rev. Lett. 105 (2010) 022302
16. Azimuthal di-hadron correlations in d+ Au and Au + Au collisions at $\sqrt{s_{NN}}$=200 GeV measured at the STAR detector
    M. M. Aggarwal et al., (STAR Collaboration)
    Phys. Rev. C 82 (2010) 024912
17. Pion femtoscopy in p+p collisions at $\sqrt{s_{NN}}$=200 GeV M. M. Aggarwal et al., (STAR Collaboration)
    Phys. Rev. C 83 (2011) 64905
18. Longitudinal scaling property of the charge balance function in Au+Au collisions at $\sqrt{s_{NN}}$=200 GeV
    B.I. Abelev et al., (STAR Collaboration)
    Physics Letters B. Vol 690 (2010) 239
19. Charged and strange hadron elliptic flow in Cu+Cu collisions at $\sqrt{s_{NN}}$= 62.4 and 200 GeV
    B.I. Abelev et al., (STAR Collaboration)
    Phys. Rev. C 81 (2010) 44902
20. Upsilon cross section in p+p collisions at $\sqrt{s_{NN}}$=200 GeV
    B.I. Abelev et al., (STAR Collaboration)
    Phys. Rev. D 82 (2010) 12004
21. Three-Particle Coincidence of the Long Range Pseudorapidity Correlation in High Energy Nucleus-Nucleus Collisions
    B.I. Abelev et al., (STAR Collaboration)
    Phys. Rev. Lett. 105 (2010) 22301
22. Inclusive pi^0, η, and direct photon production at high transverse momentum in p+p and d+Au collisions at $\sqrt{s_{NN}}$=200 GeV
    B.I. Abelev et al., (STAR Collaboration)
    Phys. Rev. C 81 (2010) 64904
23. Observation of $\pi^+\pi^-\pi^+\pi^-$ photoproduction in ultraperipheral heavy-ion collisions at $\sqrt{s_{NN}}$=200 GeV at the STAR detector
    B.I. Abelev et al., (STAR Collaboration)
    Phys. Rev. C 81 (2010) 44901

24. Spectra of identified high-p_T $\pi^{\pm}$ and p($\overline{\text{p}}$) in Cu + Cu collisions at $\sqrt{s_{NN}}$=200 GeV
B.I. Abelev et al., (STAR Collaboration)
Phys. Rev. C 81 (2010) 54907

25. Longitudinal double-spin asymmetry and cross section for inclusive neutral pion production at midrapidity in polarized proton collisions at $\sqrt{s_{NN}}$=200 GeV
B.I. Abelev et al., (STAR Collaboration)
Phys. Rev. D 80 (2009) 111108

26. Observation of an Antimatter Hypernucleus
B.I. Abelev et al., (STAR Collaboration)
Science 328, 58-62 (2010)

27. Longitudinal spin transfer to Lambda and Lambda hyperons in polarized p+p collisions at $\sqrt{s_{NN}}$=200 GeV
B.I. Abelev et al., (STAR Collaboration)
Phys. Rev. D 80 (2009) 111102

28. Identified particle production, azimuthal anisotropy, and interferometry measurements in Au+Au collisions at $\sqrt{s_{NN}}$=9.2 GeV
B.I. Abelev et al., (STAR Collaboration)
Phys. Rev. C 81 (2010) 24911

- Presentations

1. Production of light (anti)nuclei, (anti)hypernuclei and di-Lambda in central Au+Au collisions at RHIC
The14th National Conference on Nuclear Structure in China (NSC2012), April 12-16, 2012, Huzhou, China.

2. Observation of the antimatter helium-4 (anti-α) nucleus
The 9th Workshop on QCD Phase Transitions and Relativistic Heavy Ion Collisions, July 18-20, 2011, Hangzhou, China.

3. Observation of the antimatter helium-4 (anti-α) nucleus
The 22nd International Conference on Ultra-Relativistic Nucleus-Nucleus Collisions: Quark Matter 2011, May 23-28, 2011. Annecy, France, Europe.

4. Observation of the antimatter helium-4 (anti-α) nucleus
STAR Annual Collaboration Meeting, May 15-20, 2011. Prague, Czech Republic, Europe.

5. Observation of the antimatter helium-4 nucleus
STAR Annual Analysis Meeting, March 14-18, 2011. Brookhaven National Laboratory (BNL), Upton, USA.

6. Search For Anti-^{4}He In Run10 AuAu Collision
STAR Annual Collaboration Meeting, Nov 12-17, 2010. Brookhaven National Laboratory (BNL), Upton, USA.

7. STAR High Level Trigger in Run10 and offline dE/dx calibration
   STAR Annual Analysis Meeting, June 15-18, 2010. University of California, Los Angeles (UCLA), USA.
8. STAR High Level Trigger online QA, Time Projection Chamber calibration and anti–α search
   Post at 2010 RHIC-AGS Annual User's Meeting, June 10-14, 2010, Brookhaven National Laboratory (BNL), Upton, USA.

- Nature paper proofs

Ernest Orlando Lawrence Berkeley National Laboratory

May 5th, 2011

To Whom It May Concern:

Mr. Liang Xue was the leading author for the recent STAR publication of "Observation of the antimatter helium-4 nucleus", published in ***Nature*** on March 24th, 2011 (doi:10.1038/nature10079). In the past two years, I have been impressed by his contributions to the STAR experiment.

In case you have any question, please feel free to contact me.

Sincerely yours,

Nu Xu

Spokesperson for the STAR Collaboration (http://www.star.bnl.gov/)

Senior Scientist
Nuclear Science Division
Lawrence Berkeley National Laboratory

Nuclear Sciences Division One Cyclotron Road MS 70-319 Berkeley, CA 94720
Office Phone: 510-495-2851 Cell Phone: 510-289-8119 Fax: 510-486-4818

Appendix A: $^{4}\overline{\mathrm{He}}$ event display

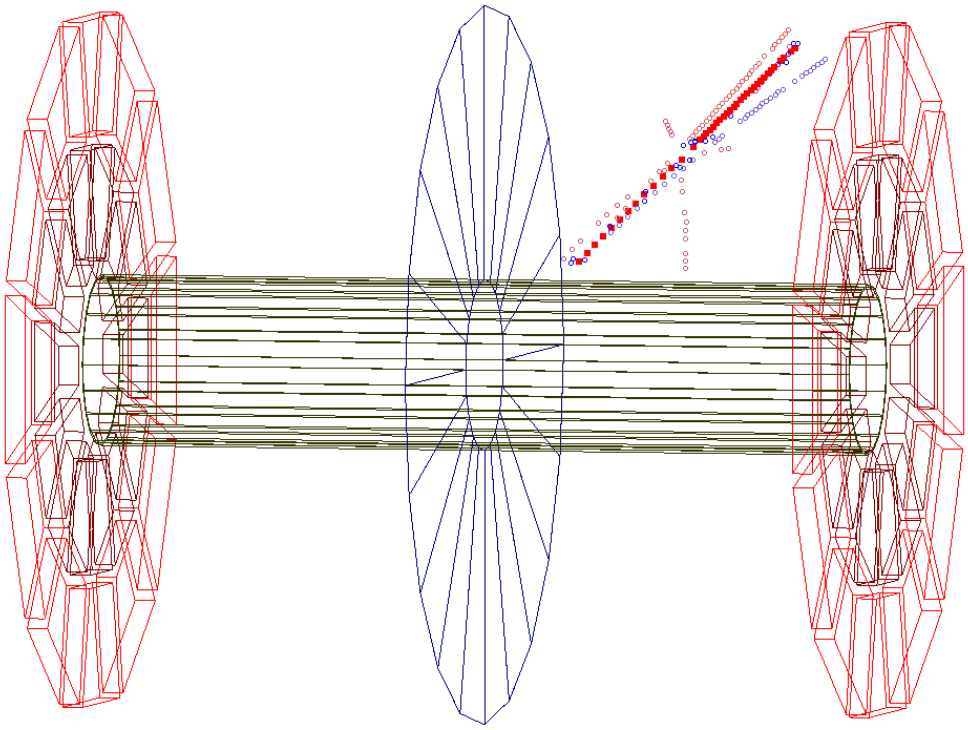

Figure 1: TPC event display for $^{4}\overline{\mathrm{He}}$ with run number 11073003. The red solid rectangles highlight the $^{4}\overline{\mathrm{He}}$ candidate. Tracks in other colors have at least one hit within 5 cm of the $^{4}\overline{\mathrm{He}}$ candidate.

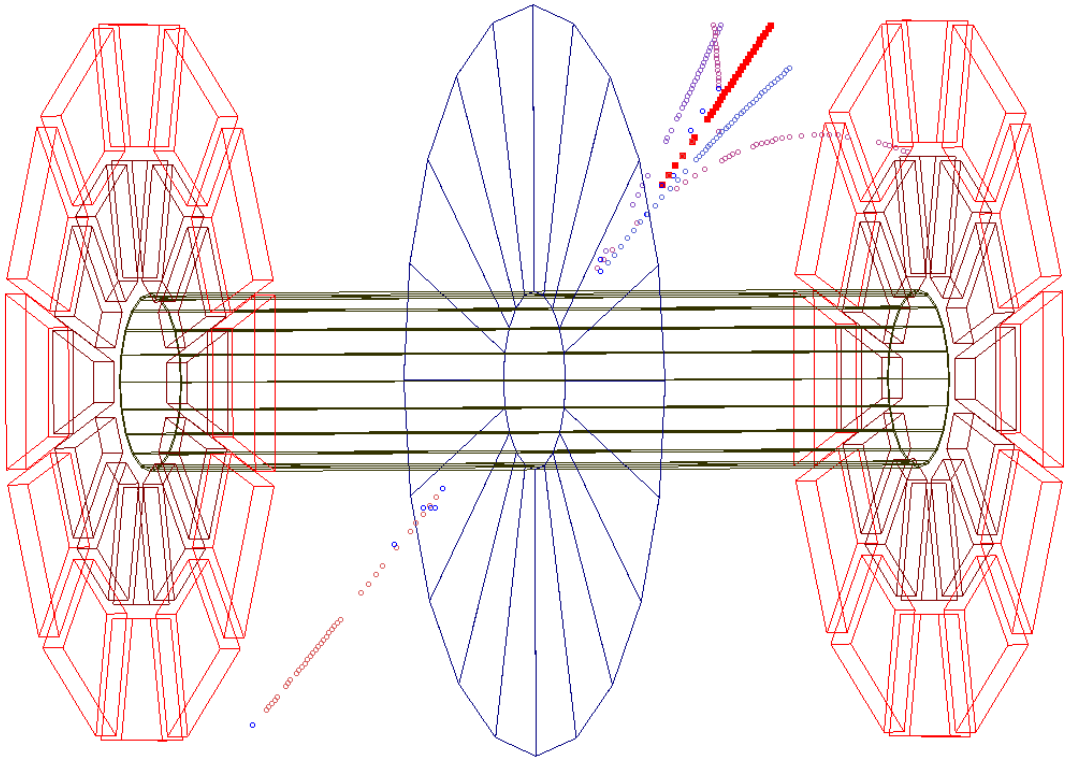

Figure 2: TPC event display for $^4\overline{\text{He}}$ with run number 11039055. The red solid rectangles highlight the $^4\overline{\text{He}}$ candidate. Tracks in other colors have at least one hit within 5 cm of the $^4\overline{\text{He}}$ candidate.

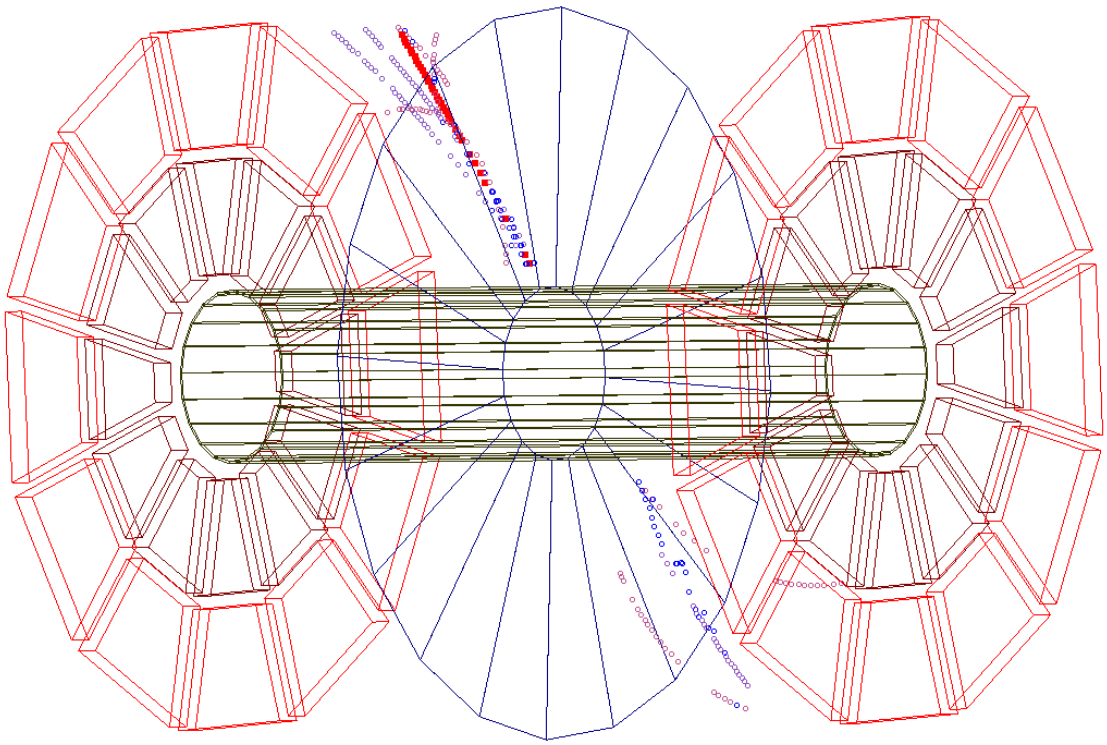

Figure 3: TPC event display for $^4\overline{\text{He}}$ with run number 11068026. The red solid rectangles highlight the $^4\overline{\text{He}}$ candidate. Tracks in other colors have at least one hit within 5 cm of the $^4\overline{\text{He}}$ candidate.

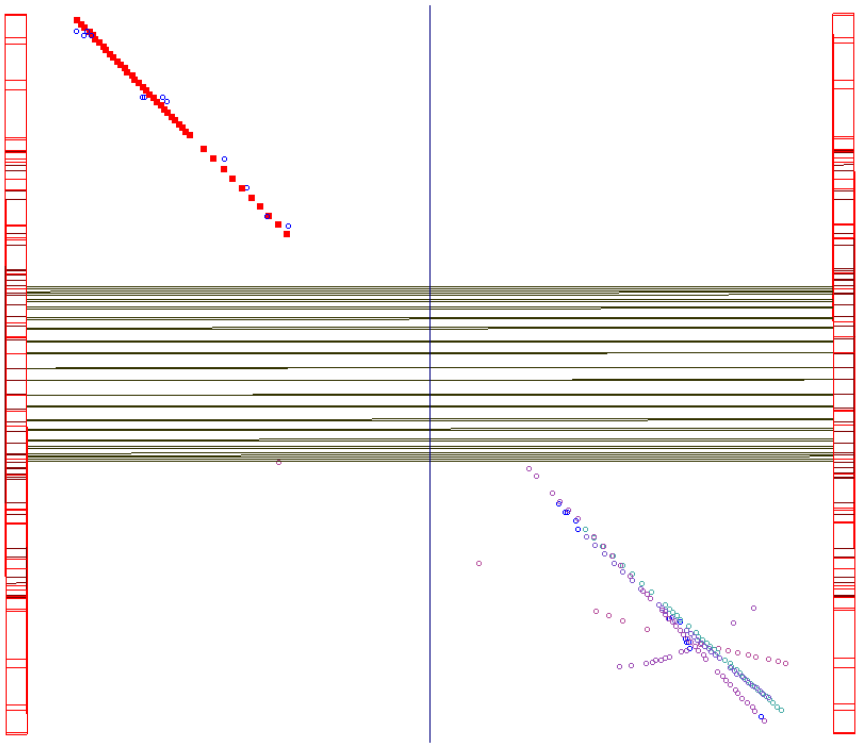

Figure 4: TPC event display for $^{4}\overline{\mathrm{He}}$ with run number 11058065. The red solid rectangles highlight the $^{4}\overline{\mathrm{He}}$ candidate. Tracks in other colors have at least one hit within 5 cm of the $^{4}\overline{\mathrm{He}}$ candidate.

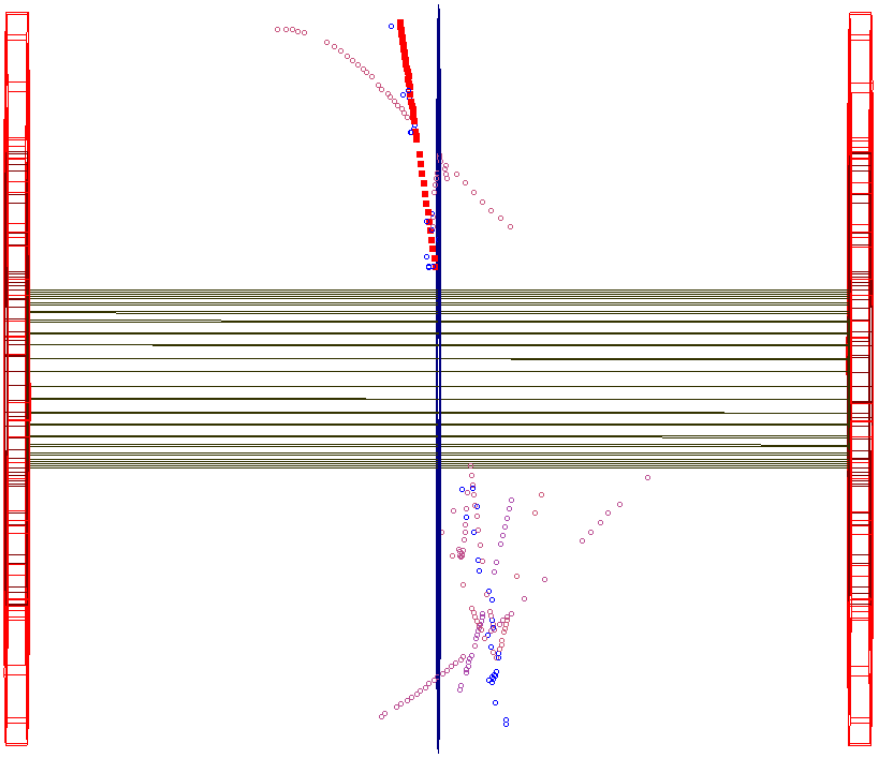

Figure 5: TPC event display for $^{4}\overline{\mathrm{He}}$ with run number 11067003. The red solid rectangles highlight the $^{4}\overline{\mathrm{He}}$ candidate. Tracks in other colors have at least one hit within 5 cm of the $^{4}\overline{\mathrm{He}}$ candidate.

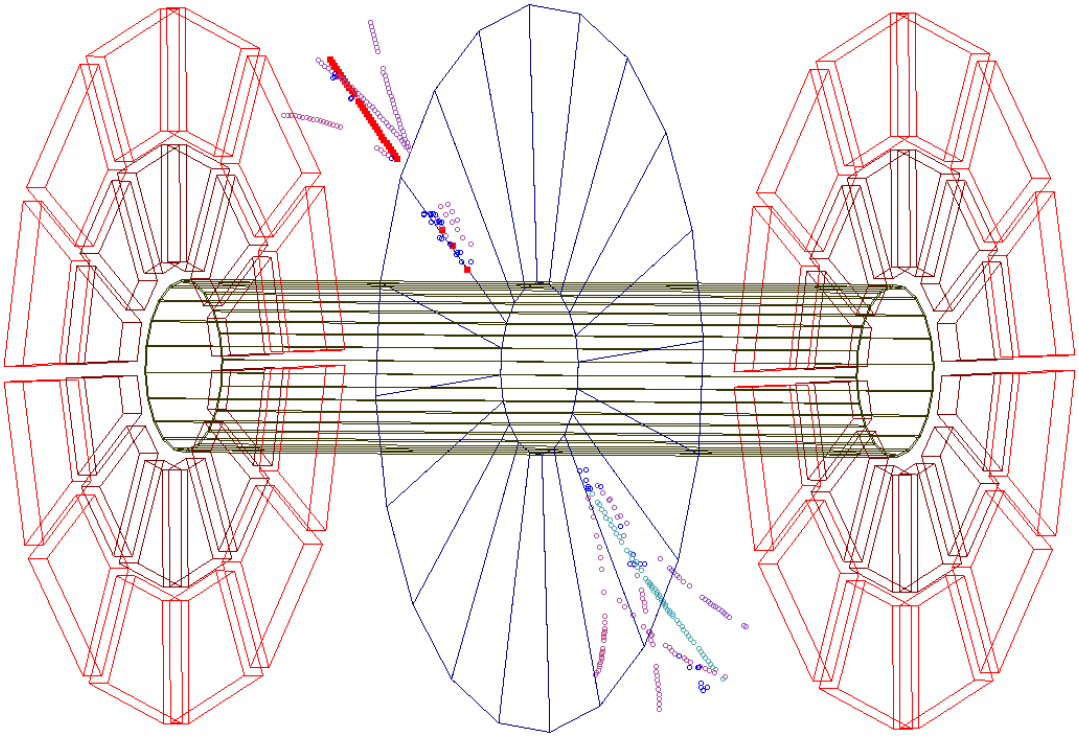

Figure 6: TPC event display for $^4\overline{\text{He}}$ with run number 11058057. The red solid rectangles highlight the $^4\overline{\text{He}}$ candidate. Tracks in other colors have at least one hit within 5 cm of the $^4\overline{\text{He}}$ candidate.

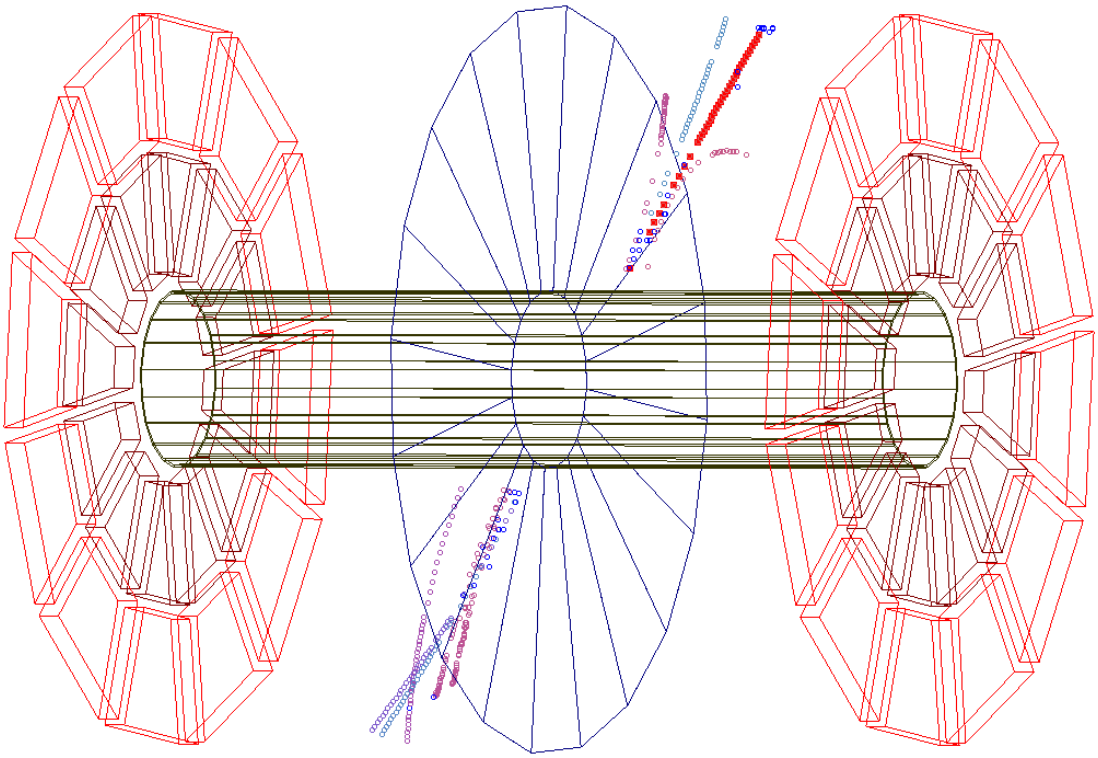

Figure 7: TPC event display for $^4\overline{\text{He}}$ with run number 11071001. The red solid rectangles highlight the $^4\overline{\text{He}}$ candidate. Tracks in other colors have at least one hit within 5 cm of the $^4\overline{\text{He}}$ candidate.

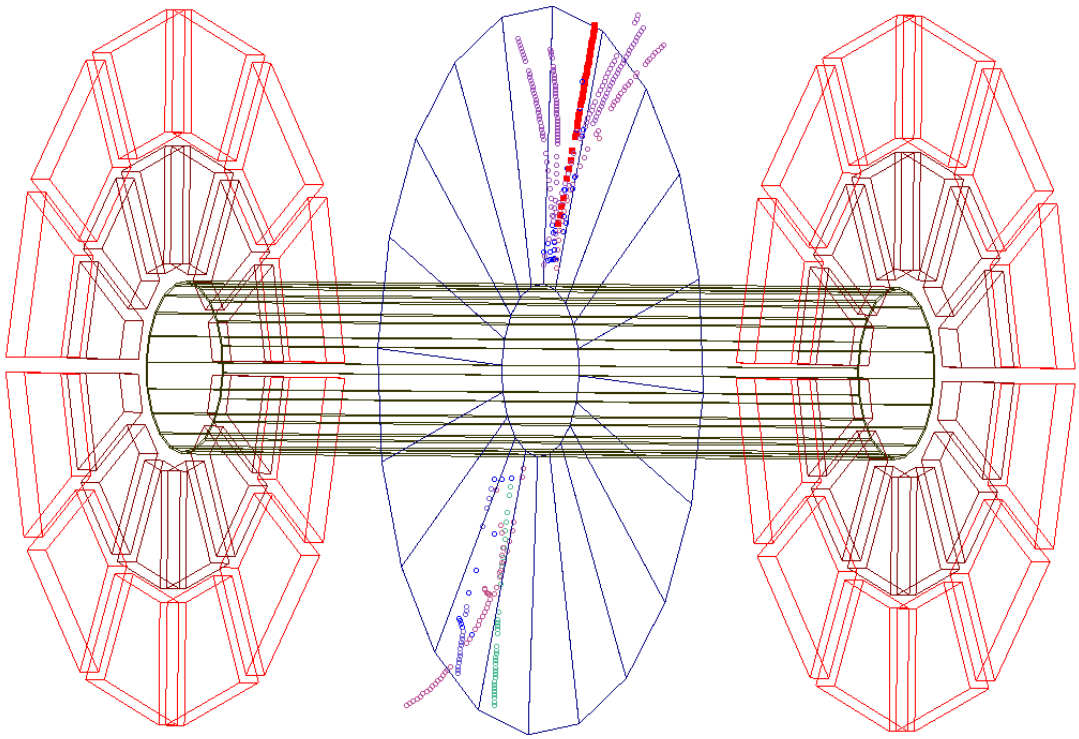

Figure 8: TPC event display for $^{4}\overline{\mathrm{He}}$ with run number 11038029. The red solid rectangles highlight the $^{4}\overline{\mathrm{He}}$ candidate. Tracks in other colors have at least one hit within 5 cm of the $^{4}\overline{\mathrm{He}}$ candidate.

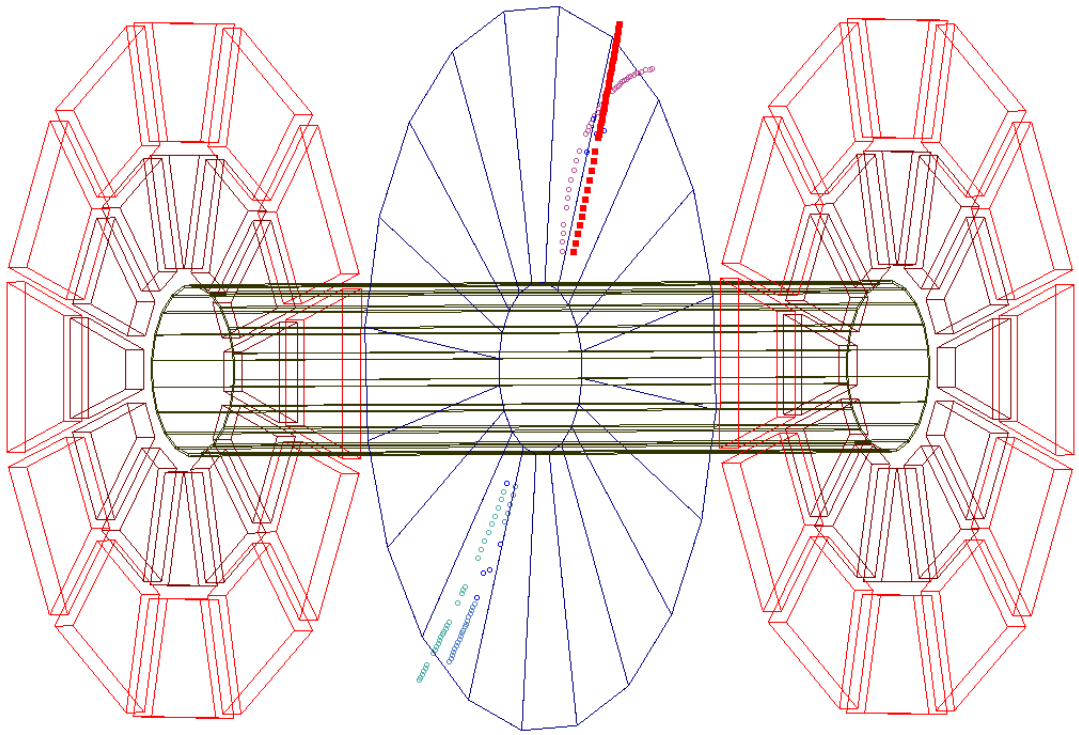

Figure 9: TPC event display for $^{4}\overline{\mathrm{He}}$ with run number 11042004. The red solid rectangles highlight the $^{4}\overline{\mathrm{He}}$ candidate. Tracks in other colors have at least one hit within 5 cm of the $^{4}\overline{\mathrm{He}}$ candidate.

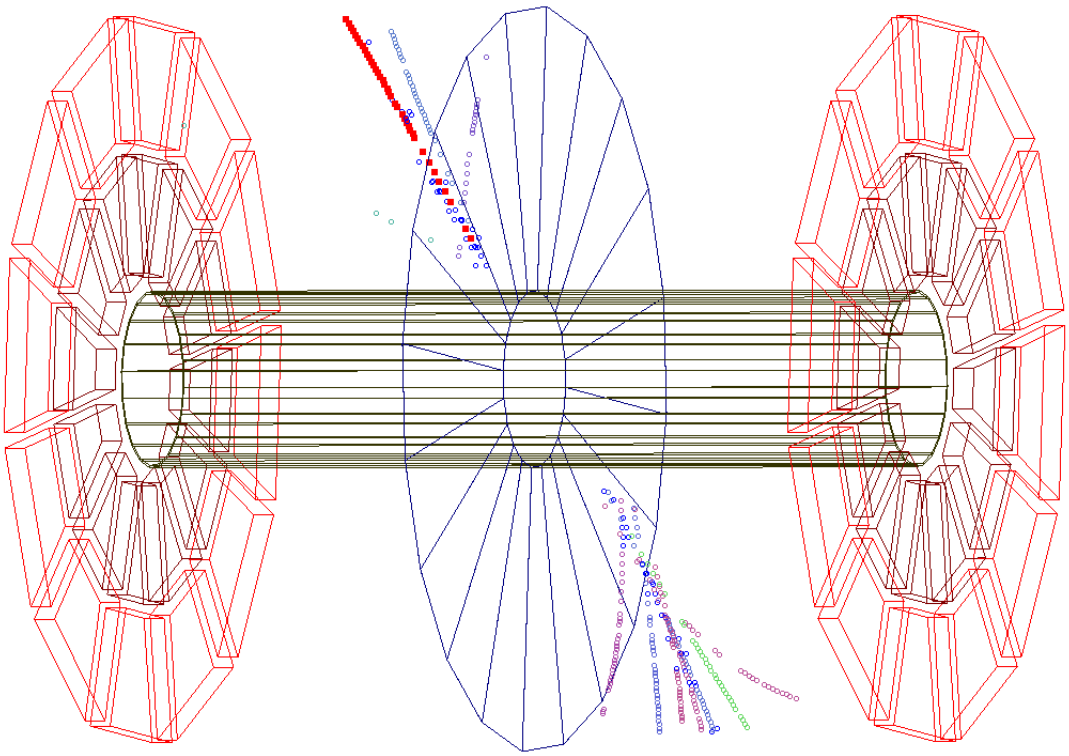

Figure 10: TPC event display for $^4\overline{\text{He}}$ with run number 11049030. The red solid rectangles highlight the $^4\overline{\text{He}}$ candidate. Tracks in other colors have at least one hit within 5 cm of the $^4\overline{\text{He}}$ candidate.

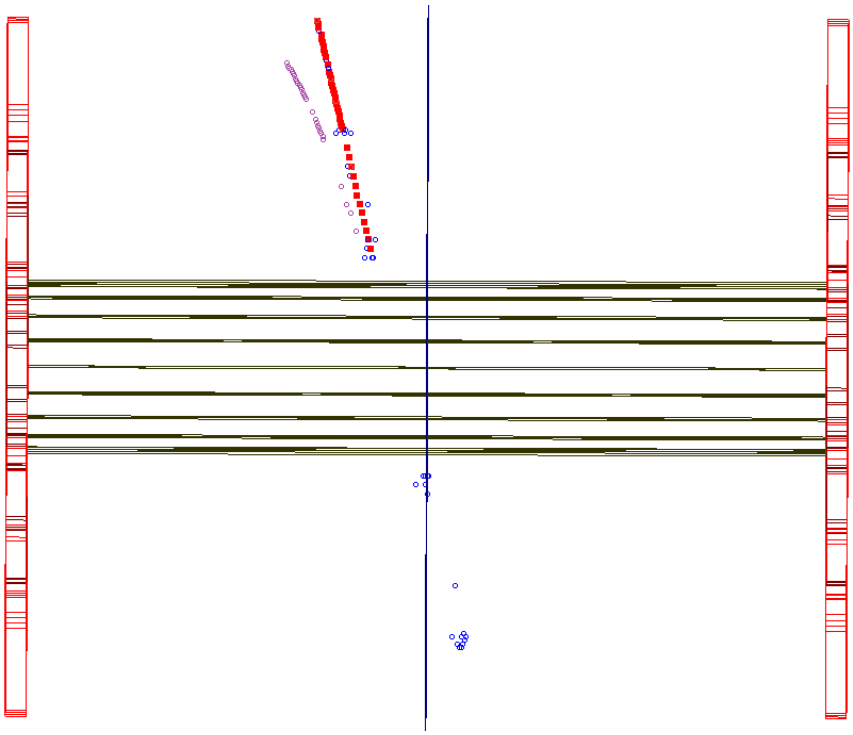

Figure 11: TPC event display for $^4\overline{\text{He}}$ with run number 11061082. The red solid rectangles highlight the $^4\overline{\text{He}}$ candidate. Tracks in other colors have at least one hit within 5 cm of the $^4\overline{\text{He}}$ candidate.

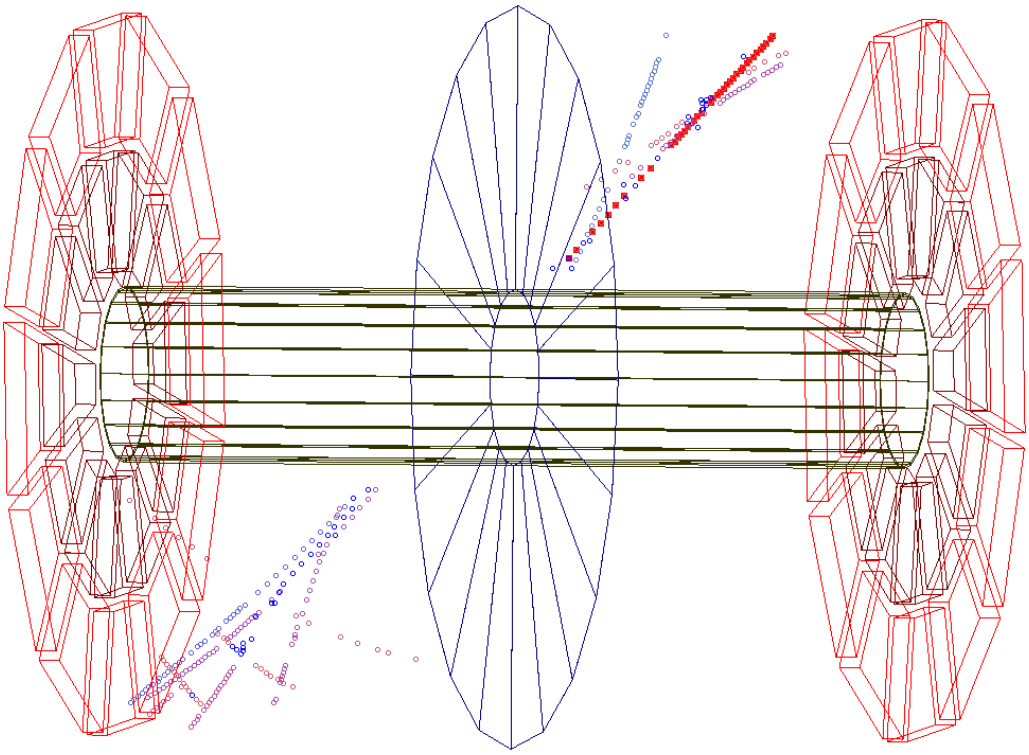

Figure 12: TPC event display for $^{4}\overline{\text{He}}$ with run number 11036057. The red solid rectangles highlight the $^{4}\overline{\text{He}}$ candidate. Tracks in other colors have at least one hit within 5 cm of the $^{4}\overline{\text{He}}$ candidate.

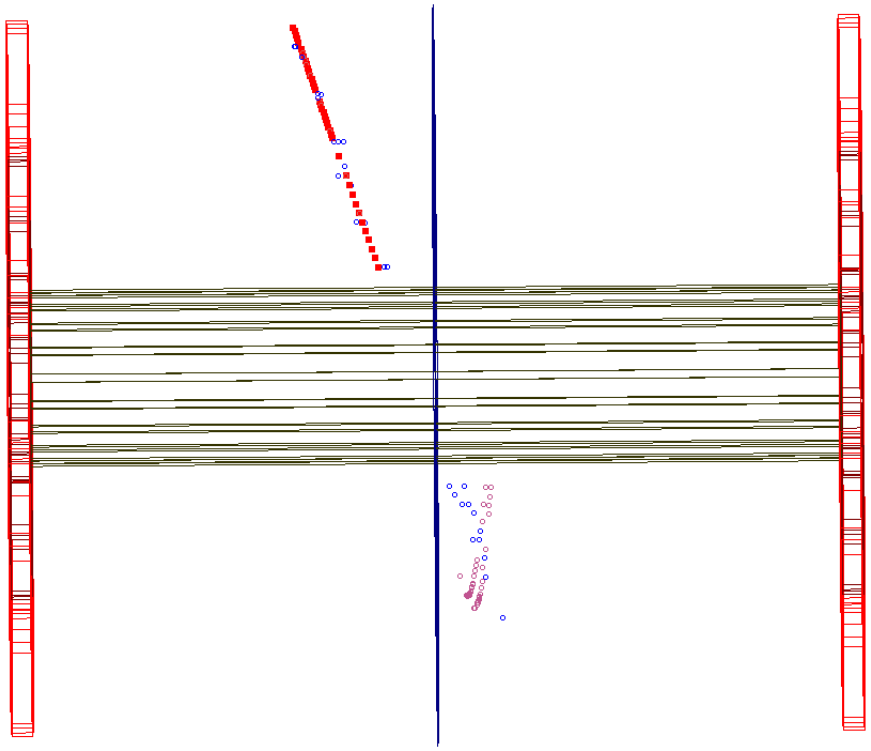

Figure 13: TPC event display for $^{4}\overline{\text{He}}$ with run number 11073073. The red solid rectangles highlight the $^{4}\overline{\text{He}}$ candidate. Tracks in other colors have at least one hit within 5 cm of the $^{4}\overline{\text{He}}$ candidate.

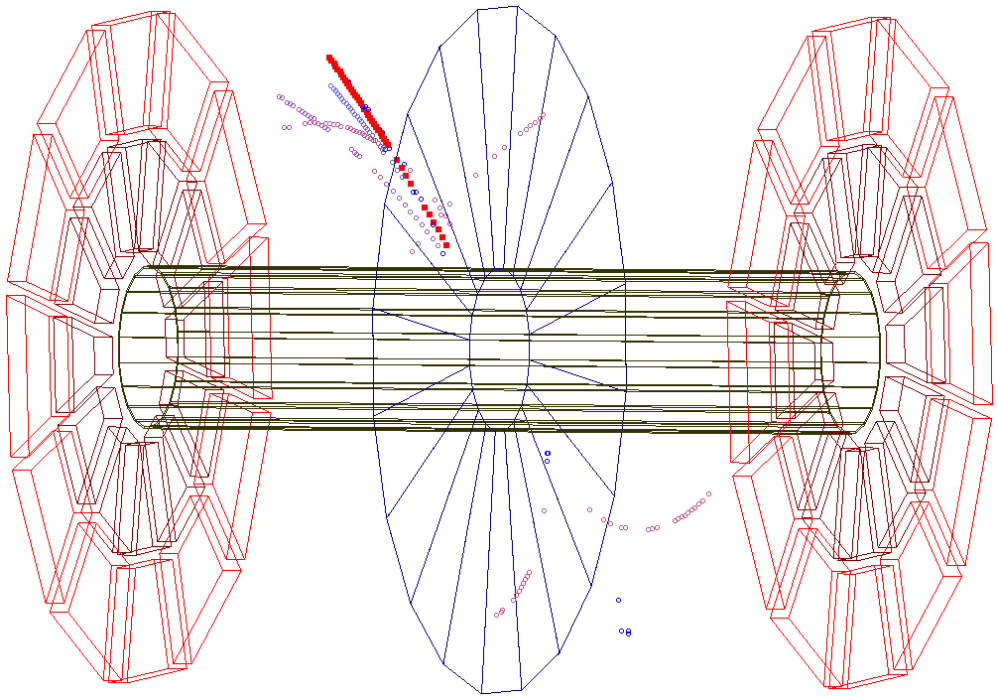

Figure 14: TPC event display for $^4\overline{\text{He}}$ with run number 11040022. The red solid rectangles highlight the $^4\overline{\text{He}}$ candidate. Tracks in other colors have at least one hit within 5 cm of the $^4\overline{\text{He}}$ candidate.

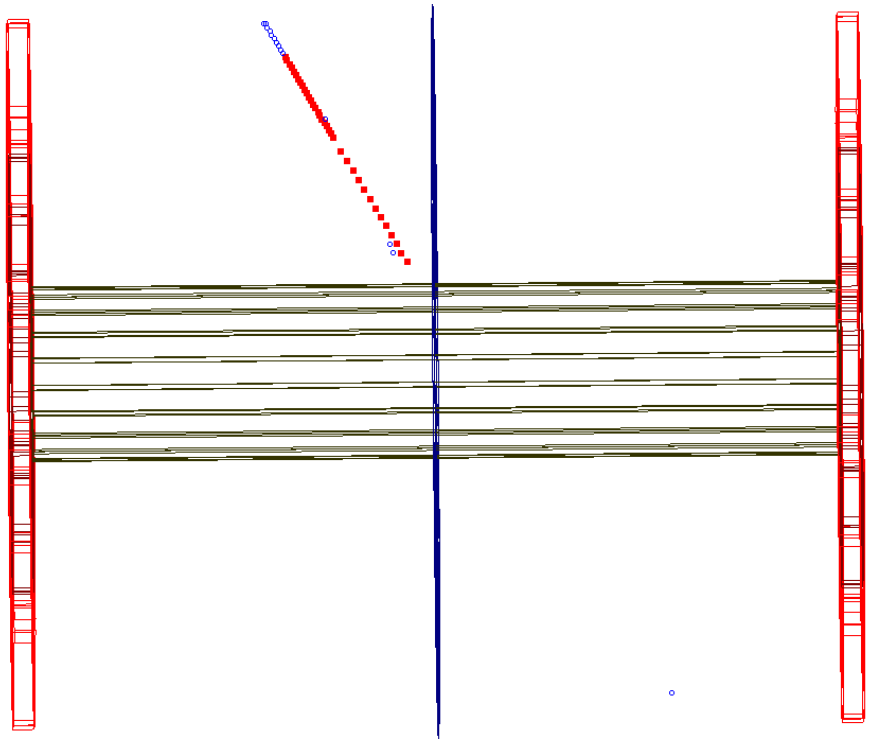

Figure 15: TPC event display for $^4\overline{\text{He}}$ with run number 11051001. The red solid rectangles highlight the $^4\overline{\text{He}}$ candidate. Tracks in other colors have at least one hit within 5 cm of the $^4\overline{\text{He}}$ candidate.

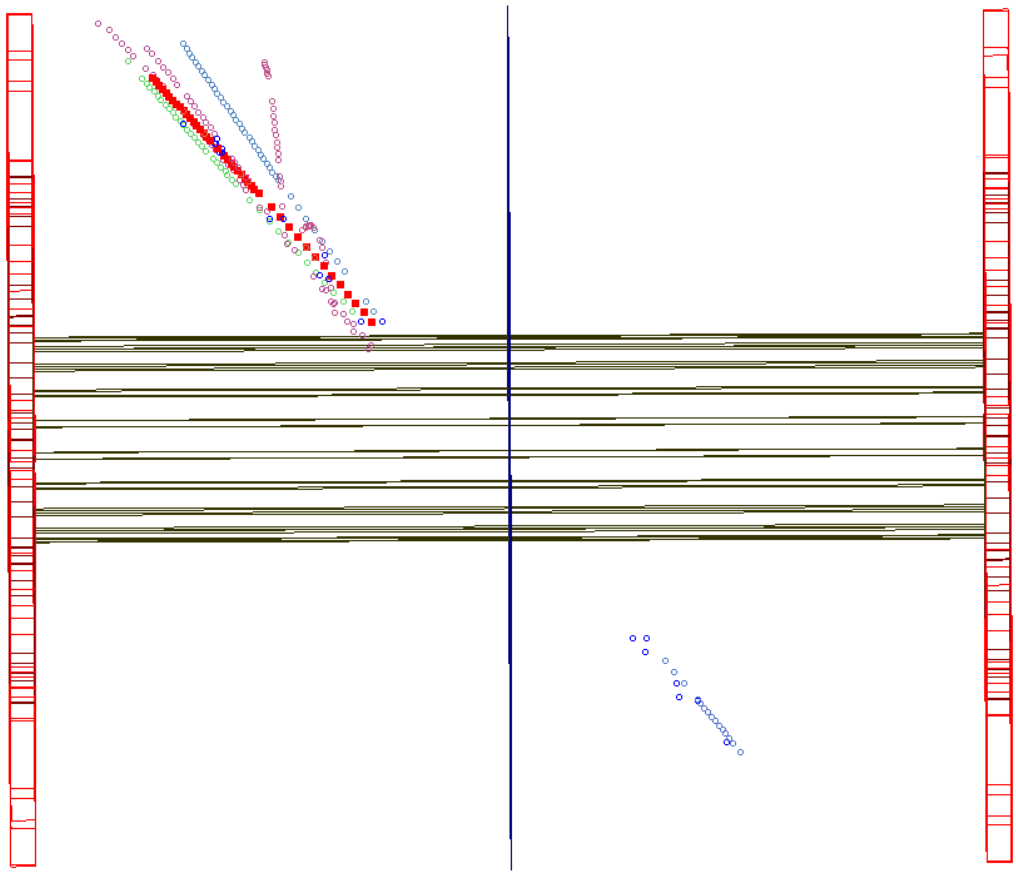

Figure 16: TPC event display for $^{4}\overline{\mathrm{He}}$ with run number 11086015. The red solid rectangles highlight the $^{4}\overline{\mathrm{He}}$ candidate. Tracks in other colors have at least one hit within 5 cm of the $^{4}\overline{\mathrm{He}}$ candidate.

Appendix B: $^4\overline{\mathrm{He}}$ properties

RunID	EvtID	Vz	nHit	ndEdx	$p/\|Z\|$	η	ϕ	dca	length	χ^2	n$\sigma_{^4He}$	E	tofZ	tofY	tot	tof	β	m
11073003	164108	-4.21	41	20	2.32	0.79	2.84	0.79	250.80	1.62	2.10	-	-0.92	-1.49	25.92	12.14	0.78	3.73
11039055	210350	-6.60	32	20	2.93	0.62	0.26	0.65	230.60	1.72	1.71	7.60	1.50	-0.21	19.40	10.21	0.84	3.82
11068026	39668	21.47	35	17	2.72	0.60	5.32	0.12	220.40	0.82	1.04	4.35	-1.06	1.15	24.36	10.20	0.83	3.60
11058065	578838	2.80	42	23	2.19	0.87	6.01	0.23	268.43	1.00	0.67	-	0.49	-1.41	25.05	13.27	0.75	3.90
11067003	459202	-7.38	41	22	1.77	0.15	5.26	0.41	192.10	1.87	0.58	3.83	0.62	-0.44	30.80	10.14	0.71	3.53
11058057	14412	-7.89	34	20	2.55	-0.38	0.89	0.15	206.80	0.33	0.47	6.63	-2.29	-0.66	30.50	9.45	0.81	3.76
11071001	22782	13.80	39	22	1.90	0.52	0.08	0.33	209.70	0.65	0.26	7.33	-0.21	1.42	26.20	11.40	0.71	3.72
11038029	198533	8.32	38	20	2.30	-0.28	4.90	0.35	198.80	0.56	-0.71	5.39	-1.85	-1.23	30.00	9.62	0.77	3.78
11042004	32163	-3.15	44	22	1.89	-0.16	2.33	0.35	193.83	0.69	-1.03	6.63	0.39	-0.15	20.30	9.95	0.72	3.66
11049030	163422	-6.25	38	20	1.80	0.52	3.03	0.53	220.60	1.35	-0.92	1.92	-1.51	0.25	29.06	11.30	0.72	3.54
11061082	75580	15.94	40	24	1.84	0.23	4.69	0.13	196.23	1.07	-1.11	9.00	2.67	1.14	34.53	10.50	0.71	3.69
11036057	231733	27.77	38	16	2.40	-0.75	0.77	0.11	247.27	0.97	-1.27	2.43	-2.61	-1.50	14.93	11.30	0.81	3.49
11073073	184644	10.11	40	20	1.61	0.34	1.72	0.16	199.68	0.62	-1.72	2.93	-2.40	0.60	24.78	11.65	0.65	3.81
11040022	369055	-2.03	40	23	1.12	0.38	0.79	0.11	203.90	1.29	0.72	3.19	0.43	-0.18	31.79	14.90	0.52	3.72
11051001	331536	-19.09	36	22	1.10	0.55	1.14	0.10	197.30	0.81	0.23	1.90	-2.82	1.22	30.06	16.16	0.51	3.73
11086015	43011	17.56	43	25	1.81	0.70	0.96	0.11	241.00	0.39	-0.03	5.77	1.49	-0.46	32.5	12.70	0.71	3.63

Table 1: Properties for the 16 $^4\overline{\mathrm{He}}$ candidates recored by STAR in 2010.